Study on the pathogenesis of oocyte pick-up dysfunction of oviduct in autoimmune disease-prone model mouse

（自己免疫疾患モデルマウスにおける卵管ピックアップ障害の病態発生に関する研究）

SAITO (HOSOTANI) Marina

Contents

Abbreviations

3D: three-dimensional

Actb: actin, beta

Acvr1: activin A receptor, type 1

Acvr2a: activin receptor IIA

Acvr2b: activin receptor IIB

αSMA: alpha smooth muscle actin

B6: C57BL/6N

CBF: ciliary beat frequency

chr: chromosome

CL: corpus luteum

COC: cumulus oocyte complex

D-MEM: Dulbecco's modified Eagle's medium (high glucose) with L-glutamine and phenol red

dsDNA: double-stranded DNA

Esr1: estrogen receptor 1

Esr2: estrogen receptor 2

Fas: Fas cell surface death receptor

FOB: foramen of ovarian bursa

Fshb: follicle stimulating hormone beta

Fshr: follicle stimulating hormone receptor

Gnrh1: gonadotropin releasing hormone 1

h: hour

hCG: human chorionic gonadotropin

h.p.o.: hour postovulation

HE: hematoxylin-eosin

Inha: inhibin alpha

Inhba: inhibin beta-A

Inhbb: inhibin beta-B

IVF: *in vitro* fertilization

Lhb: luteinizing hormone beta

Lhcgr: luteinizing hormone/choriogonadotropin receptor

LOB: ligament of foramen of ovarian bursa

lpr: lymphoproliferation

min: minute

Mmp2: matrix metallopeptidase 2

Mmp9: matrix metallopeptidase 9

MRL/+: MRL/MpJ

MRL/lpr: MRL/MpJ-*Fas*$^{lpr/lpr}$

MT: Masson's trichrome staining

OO: ovulated oocyte

PB: phosphate buffer

PBS: phosphate-buffered saline

PCD: primary ciliary dyskinesia

PFA: paraformaldehyde

Pgr: progesterone receptor

PMSG: pregnant mare serum gonadotropin

PUR: oocyte pick-up rate

qPCR: quantitative polymerase chain reaction

ROI: region of interest

RT: reverse transcription

S/B: spleen weight to body weight ratio

SE: standard error

SEM: scanning electron microscopy

SNV: single nucleotide variant

TEM: transmission electron microscopy

Timp1: tissue inhibitor of metalloproteinase 1

UTR: untranslated region

Preface

Infertility represents a worldwide problem in both the human and veterinary medicine. Human infertility underlies the public concern of declining birth rates in the developed country including Japan [50]. The reproductive disorder in farm animals leads to serious economic loss in the livestock industry [28] and that in endangered animals leads to the failure of species preservation [44]. Mammalian infertility is caused by complex factors in individuals of both sexes. The causes of male infertility are primarily in the semen ejection and sperm problems in numbers, morphology, and motility [68]. On the other hand, female infertility and reproductive disorder has more complex and various causes compared to the male one, including anatomical abnormalities of ovaries, oviducts and uterus, and abnormality of endocrine system and immune system [107,115]. Therefore, approximately 20 to 30% of infertility cases in women are caused by medically unexplained factors [98]. In veterinary medicine, female livestock animals such as cows and horses are the target of treatment for reproductive disorders that aims to improve their reproductive performance and achieve high productivity. However, 14 % of dairy cows are diagnosed with repeat breeders in Japan [151], which are defined as cows that fail to pregnant after three or more breeding attempts without any detectable abnormalities [41].

There are many unexplained mechanisms underlying the physiological regulation and pathology of female reproductive functions such as ovulation, oocyte pick-up and transport by oviducts, implantation, and embryo development. Therefore, it is difficult to diagnose and treat all female infertility and reproductive disorders in medical and veterinary clinical environment. At present, sex hormonal tests, pelvic ultrasound imaging tests, and hysterosalpingography are generally performed to diagnose ovulation disorder, anatomical abnormality of the female reproductive organs, and the blockage of oviducts in women [9,97]. In the infertile livestock animals, ultrasonography, body condition assessment, and behavioral checks are general diagnosing methods of female reproductive tracts [126]. Based on the pointed causes, there are some treatment options such as hormonal medications, surgery, or assisted reproductive technology [133]. On the other hand, there are no effective methods to detect the dysfunction of oocyte pick-up and transport by oviducts. Especially, the evaluation of oviducts in living animals is difficult to perform in the veterinary clinical field [57]. However, the percentage of oviductal abnormalities in cows has been reported to range from approximately 2 to 60%, although which varied widely depending on the country where the examination was conducted [83]. In the Spanish reports which

experimentally examined oviductal patency in repeat breeders, the 44% of repeat breeder Holstein cows had oviductal obstruction, which did not correlate with postpartum reproductive or metabolic diseases [35]. It is suspected that the oocyte pick-up dysfunction may be involved in the pathogenesis of female infertility and reproductive disorder when various tests can not clinically determine the any abnormalities in the reproductive function [2,52]. Although abnormality of ciliary beating of the oviductal epithelium in experimental rodents is necessary for oocyte pick-up [63,149], the pathogenesis of oocyte pick-up dysfunction and its relationship with the epithelial pathology has not been understood in the infertile cases of human and animals. To overcome the unexplained female infertility, the details of the oviductal pathology should be clarified by the basic research.

Importantly, the disrupted immune system, as well as age and endocrine abnormality, is one of the risk factors of female infertility and reproductive disorder [130]. In cows, bacterial and viral agents are causes of reproductive disorders, and Chlamydial and fungal infections directly impair the function of reproductive tracts [148]. Furthermore, it is suggested that inflammation, rather than infection, reduces the fertility in the dairy cows [15]. While pelvic inflammatory disease such as Chlamydial infection causes the local effect and structural disruption in reproductive tracts including the oviductal blockage and adhesions of oviducts to surrounding tissues [125], systemic disruption of immune system, i.e. autoimmune disease, causes the functional abnormality of women reproductive organs [61]. Autoimmune disease has been reported to be involved in premature ovarian failure, endometriosis, polycystic ovary syndrome, and unexplained women infertility [43]. Premature ovarian failure, defined by premature depletion of ovarian follicle before the age of 40 years [7], has been suggested to be associated with autoimmune reactions of lymphocytes and autoantibodies to ovarian steroid cells [13]. The autoantibodies in women patients with autoimmune thyroid disease has been thought to increase risk of infertility [128]. Thus, although it is clear that autoimmune disease affects the female reproductive function, the relationship between immune abnormality and oviductal function has not been elucidated.

Herein, the thesis, which consists of four Chapters, explores the pathology and pathogenesis of oocyte pick-up dysfunction as the oviductal factors involved in immune abnormality-related female infertility by using autoimmune disease model mice. The first Chapter developed the histological method to evaluate the murine oocyte pick-up function and examined the relationship between oocyte pick-up dysfunction and autoimmune disease. The second Chapter examined the anatomical characters of the murine female reproductive tracts involving in facilitating oocyte

pick-up in the autoimmune disease model. The third Chapter clarified the unique phenotypes regulating ovarian functions in autoimmune disease model mice. The last Chapter investigated the ciliary morphofunction in the autoimmune disease model mice and its relationship with the pathogenesis of oocyte pick-up dysfunction. This study reveals the important relationship between immune abnormality and oviductal morphofunction, and proposes the novel pathological theory on female infertility and reproductive disorders in the field of human and veterinary medicine.

Notes

Contents of the thesis were published in the following articles

1. Hosotani M, Ichii O, Nakamura T, Otsuka-Kanazawa S, Elewa YHA, Kon Y. 2018. Autoimmune abnormality affects ovulation and oocyte-pick-up in MRL/MpJ-Fas$^{lpr/lpr}$ mice. *Lupus* 27: 82-94.
2. Hosotani M, Ichii O, Nakamura T, Masum MA, Otani Y, Otsuka-Kanazawa S, Elewa YHA, Kon Y. 2019. MRL/MpJ mice produce more oocytes and exhibit impaired fertilisation and accelerated luteinisation after superovulation treatment. *Reproduction, fertility, and development* 31: 760-773.
3. Hosotani M, Ichii O, Nakamura T, Masum MA, Otani Y, Elewa YHA, Kon Y. 2020. Altered ciliary morphofunction in the oviductal infundibulum of systemic autoimmune disease-prone MRL/MpJ-Fas$^{lpr/lpr}$ mice. *Cell and Tissue Research* 380: 627-641.
4. Hosotani M, Ichii O, Nakamura T, Namba T, Islam MR, Elewa YHA, Watanabe T, Ueda H, Kon Y. 2021. Anatomy and histology of the foramen of ovarian bursa opening to the peritoneal cavity and its changes in autoimmune disease-prone mice. *Journal of Anatomy* 238: 73-85.

Chapter 1

Autoimmune abnormality affects oocyte pick-up in autoimmune disease-prone mice

Introduction

Mammalian female infertility is caused by morphofunctional changes in reproductive tract including ovary, oviduct, and uterus. These disorders in female reproductive tracts are triggered by abnormalities in genomic background, endocrine profile, metabolic condition, or immune system [107,115]. Especially, a close relationship between female infertility and autoimmune diseases has been reported. For example, human patients with autoimmune diseases that are local, such as autoimmune hepatitis or autoimmune thyroid disease, or systemic, like multiple sclerosis and celiac disease, have increased risks of infertility [13]. However, the pathological mechanism underlying autoimmune disease impairs the female reproductive process is not completely elucidated. In veterinary medical fields, it is unknown whether autoimmune disease or systemic immune abnormality relates to the pathogenesis of female reproductive disorders.

Ovulation and oocyte pick-up is essential for the progression of fertilization, and any abnormality in these processes can cause female infertility [37,121]. Mammalian oocytes are ovulated into the peritoneal or bursal cavity and picked-up by the infundibulum of the oviduct, defined as “oocyte pick-up”. In human, ovulatory disorders and tubal abnormalities make up about 25% and 20% of female infertility, respectively [86,115,133], while approximately 20 to 30% of female infertility cases are caused by medically unexplained factors [98]. In veterinary medical fields, ovulation disorder due to ovarian cysts is frequently diagnosed in cows [91], and obstruction of oviducts is occasionally found in cows and mares [51]. Ovulation and oocyte pick-up is intricately regulated by multiple factors including sex hormonal dynamics and physical and temporal effects, so that the actual physiological mechanism of the process is not fully understood. Therefore, there is no reports on the relationship between autoimmune disease and the disorder of ovulation and oocyte pick-up.

The previous report revealed the pathological relationship between autoimmune disease and ovarian function by using MRL/MpJ (MRL/+) strain mice, a representative murine model for autoimmune disease [92]. The MRL/MpJ-*Fas*$^{lpr/lpr}$ (MRL/lpr) strain bears the lymphoproliferation mutation (*lpr*) in the Fas cell surface death receptor (*Fas*) gene [105], causing severe phenotypes associated with spontaneous systemic autoimmune disease compared to MRL/+ mice, including splenomegaly, arthritis, vasculitis, and autoimmune glomerulonephritis [1], which are similar to human systemic lupus erythematosus exhibits more severe phenotypes compared to MRL/+ mice that are similar to human systemic lupus erythematosus [105]. MRL/lpr mice manifested ovarian abnormalities characterized by a decreased number of ovarian follicles and corpora lutea, increased infiltrating lymphocytes within the

ovarian interstitium [92]. Thus, the author hypothesized that these autoimmune disease-related female reproductive phenotypes affect oocyte pick-up and evaluated the relationship between oocyte pick-up and systemic autoimmune disease by histological examination of ovary and oviduct of MRL/+ strain model mice as well as C57BL/6N (B6) mice as healthy control. To investigate the decreased efficiency of oocyte pick-up by oviducts in MRL/lpr mice during the progression of autoimmune disease, the author developed a novel method to evaluate oocyte pick-up.

Materials and Methods

Animals

Animal experimentation was approved by the Institutional Animal Care and Use Committee of the Graduate School of Veterinary Medicine, Hokkaido University (Approval No. 15-0079). Experimental animals were handled in accordance with the Guide for the Care and Use of Laboratory Animals, Graduate School of Veterinary Medicine, Hokkaido University (approved by the Association for Assessment and Accreditation of Laboratory Animal Care International). Female B6, MRL/+, and MRL/lpr mice at 3 and 6 months of age were obtained from Japan SLC, Inc. (Shizuoka, Japan). Mice were confirmed to have normal estrus cycles by monitoring vaginal smears. It has been reported that MRL/+ mice exhibit regular estrous cyclicity, with each cycle lasting 4 to 7 days until 11 months of age. On the other hand, MRL/lpr mice were found to start to develop spontaneous autoimmune abnormality at 3 months [1)] and lose estrous cyclicity after 6 months, as characterized by a prolonged diestrus period and a shortened estrus period [92)]. The mice were housed in plastic cages in groups at 18°C to 26°C under a 12 h light/dark cycle and had free access to commercial diet and water. All mice were euthanized by cutting of the carotid artery or cervical dislocation under deep anesthesia using a mixture of medetomidine (0.3 mg/kg), midazolam (4 mg/kg), and butorphanol (5 mg/kg).

Evaluation of autoimmune disease condition

Spleen were collected from euthanized mice in order to measure the spleen weight to body weight ratio (S/B), which serves as a marker of an autoimmune disease. In addition, anti-double-strand DNA (dsDNA) antibody levels in mice serum were measured to evaluate systemic autoimmune condition using Mouse Anti-dsDNA Ig's (Total A+G+M) ELISA kit (Alpha Diagnostic International, San Antonio, TX, USA) according to the manufacturer's instructions.

Evaluation of ovulation and oocyte pick-up by the oviduct

Superovulation treatment

To evaluate ovulation and oocyte pick-up ability, superovulation treatment was performed because obtaining oocytes without superovulation is difficult, since the timing of ovulation is unsteady by the mouse. Pregnant mare serum gonadotropin (PMSG, ASKA Animal Health Co., Ltd., Tokyo, Japan) was injected intraperitoneally to mice (200 μL of 37.5 IU/mL gonadotropin per mouse). After 48 h of PMSG injection, these mice were injected intraperitoneally with the same dose of human chorionic

gonadotropin (hCG, ASKA Animal Health Co., Ltd.). After 24 h of hCG injection, the ovaries and oviducts were collected and immediately placed in 0.01 M phosphate buffered saline (PBS) until the next step.

Measurement of oocyte pick-up rate by the oviduct.

(a) Number of cumulus oocyte complexes (COCs): "COCs" were defined as oocytes picked-up by the infundibulum and found in the ampulla of oviducts. Under a stereoscopic microscope, oviducts were carefully stretched and cut off at uterine ostium from the uterus. On the glass dish, 300 μL of 0.01 M PBS were perfused from the ostium of the infundibulum to the opening beside uterine ostium by using a 31G needle, COCs in ampulla were pushed out on the dish, and their numbers were counted.

(b) Number of ovulated oocytes (OOs): The same mice used in the measurement of COCs were examined. "OOs" were defined as oocytes before being picked-up. After counting COCs, ovaries were fixed with 4% paraformaldehyde (PFA) at 4°C overnight, embedded in paraffin, and cut into 10 μm-thick serial sections. Using serial hematoxylin-eosin (HE)-stained sections, the total number of ruptured follicles and hemorrhagic bodies, which had no oocytes inside of follicular antrum, were counted as alternative values reflecting OOs. Further, in MRL/+ and MRL/lpr mice, the total number of corpus luteum (CL) was added to the total number of ruptured follicles and hemorrhagic bodies to calculate the number of OOs.

(c) Calculation of oocyte pick-up rate (PUR): From (a) and (b) values, the PUR was calculated as follows: PUR (%) = 100 × number of COCs (a) / number of OOs (b).

Immunohistochemistry

Ovaries were collected at three and six months of age and fixed with 4% PFA at 4°C overnight, embedded in paraffin, and cut into the 3 μm-thick sections. Sections were incubated in 20 mM Tris-HCl (pH 9.0) for 20 min at 105°C. Sections were then soaked in methanol containing 0.3% H_2O_2. Sections blocked in 10% normal goat serum for 30 min at room temperature were incubated with rabbit anti-CD3 (1:200, Nichirei, Tokyo, Japan) at 4°C overnight. After three washes in PBS, sections were incubated with biotin-conjugated goat anti-rat IgG antibody for 30 min, and washed and incubated with a streptavidin-biotin complex (SABPRO Kit, Nichirei, Tokyo, Japan) for 30 min at room temperature. Sections were then incubated with 3, 3' –diaminobenzidine tetrahydrochloride-H_2O_2 solution, and

lightly stained with hematoxylin. To quantify the degree of T-cell infiltration in the infundibulum, the number of CD3-positive T-cells per 1 μm^2 was counted using the BZ-X Analyzer of the BZ-X710 Fluorescence Microscope (Keyence, Osaka, Japan).

Ultrastructural analysis

For scanning electron microscopy (SEM), a perfusion fixation was performed on B6 and MRL/lpr mice at 3 and 6 months of age. The caudal vena cava was cut and released under deep anesthesia and 20 mL of PBS and half-Karnovsky's fixing solution (2.5% glutaraldehyde, 2% PFA, 0.1 M phosphate buffer (PB), pH 7.4) perfused from the left ventricle to the whole body. To observe the infundibulum, ovaries and oviducts were collected and carefully detached from each other. Glutaraldehyde-fixed oviducts were post-fixed with 1% osmium tetroxide in 0.1 M PB for 1 h at 4°C, kept in 1% tannic acid for 1h, and post-fixed with 1% osmium tetroxide for 1 h. Specimens were dehydrated through graded alcohol, transferred into 3-methylbutyl acetate and dried using an HCP-2 critical point dryer (Hitachi, Tokyo, Japan), and observed on an S-4100 SEM (Hitachi) after ion-spatter coating.

Statistical analysis

Results are expressed as mean ± standard error (SE) and statistically analyzed in a non-parametric manner. Data between two groups were compared using the Mann-Whitney *U*-test ($P < 0.05$). The Kruskal-Wallis test was used to compare data among three or more groups. Multiple comparisons were performed using Scheffé's method when significant differences were observed overall ($P < 0.05$). Correlations between two parameters were analyzed using Spearman's correlation test ($P < 0.05$). The statistical analysis was conducted in JMP 14.2.0 (SAS Institute Inc., Cary, North Carolina, USA).

Results

Indices of autoimmune disease

For autoimmune disease indices, the S/B in MRL/lpr mice was highest among strains at both 3 and 6 months of age, and increased significantly at 6 months compared with 3 months (Figure 1-1A). Serum levels of anti-dsDNA antibody were also significantly higher in MRL/lpr mice at both 3 and 6 months than the other strains (Figure 1-1B). As described previously [92], numerous CD3-positive T-cells were observed in the ovarian interstitium of MRL/lpr mice at 3 months, that were more prominent at 6 months (Figure 1-1C). However, they were scarce in B6 and MRL/+ mice at both ages. The number of CD3-positive T-cells in ovaries was measured by histoplanimetry. MRL/lpr mice showed the highest values at both ages, while increased significantly at 6 months compared with 3 months (Figure 1-D). Thus, autoimmune disease phenotypes were obvious in MRL/lpr mice and worsened at 6 months.

The similar results were previously obtained in our earlier study [92]. However, because this MRL/lpr strain shows individual differences in autoimmune disease phenotypes, it is quite important to evaluate the autoimmune abnormalities and the inflammatory conditions in the female genital systems by using several indices, including the S/B and the T-cell numbers in the ovary, in each experiment. Furthermore, in the present study, by using these autoimmune phenotype indices, the correlation between the systemic or local autoimmune condition and the ovulation or oocyte pick-up function were analyzed in each mouse.

Ovulation and oocyte pick-up

At 3 months, the numbers of both OOs and COCs in MRL/+ and MRL/lpr mice were significantly higher than that in B6 mice (Figure 1-2A and B). At 6 months, the numbers of both OOs and COCs in MRL/lpr mice were significantly reduced compared to 3 months. However, the numbers of both OOs and COCs in B6 and MRL/+ mice showed no significant age-associated difference. The PUR calculated based on the measured numbers from Figure 1-2A and B (Figure 1-2C). The PUR did not change with the age of B6 (96 ± 2.9 % at 3 months, 86.0 ± 5.0 % at 6 months) and MRL/+ mice (157.2 ± 9.7 % at 3 months, 131.0 ± 15.7 % at 6 months). However, the PUR in MRL/lpr mice declined significantly at 6 months (94.0 ± 3.6 % at 3 months, 63.0 ± 9.6 % at 6 months).

Given that the PUR of MRL/+ mice was over 100%, the author considered the possibility that MRL/+-background mice displayed premature CL formation. The author therefore counted the CLs in addition to the numbers of ruptured follicles and hemorrhagic bodies, in MRL/+ and MRL/lpr mice

(Figure 1-2D). Furthermore, the PUR was calculated, including the number of CLs (Figure 1-2E). This value in MRL/+ mice approached 100% (98.8 ± 8.2% at three months, 81.0 ± 9.7% at six months) compared to the results in Figure 1-2C. However, the PUR including CL was significantly lower in MRL/lpr mice (72.6 ± 3.5% at three months, 45.6 ± 7.2% at six months) than in B6 and MRL/+ mice at both ages. Furthermore, this value in MRL/lpr mice significantly declined with age.

Correlations between the indices of ovulation or oocyte pick-up and autoimmune disease

To confirm whether autoimmune disease can affect ovulation and the oocyte pick-up of the oviduct, the author performed correlation analyses (Table 1-1). The number of OOs positively and negatively correlated with S/B in B6 and MRL/lpr mice, respectively. Furthermore, the number of T-cells in the ovary and the levels of serum anti-dsDNA antibodies positively correlated with those in B6 and in all mice used in the study, respectively. The number of OOs including those of CLs and of COCs had the same correlation pattern with autoimmune disease parameters. However, the PUR of all mice and of MRL/lpr mice were significantly negatively correlated with S/B and with the number of T-cells in the ovary, respectively; this rate, however, also showed a positive correlation with the levels of serum anti-dsDNA antibodies in MRL/lpr mice. Furthermore, the PUR including CL negatively correlated with all three autoimmune disease parameters in all mice. In MRL/lpr mice, this rate negatively correlated with S/B only.

Ultrastructure of the infundibulum

Next, the author examined the ultrastructure of the infundibulum epithelium in B6 and MRL/lpr mice. The infundibulum in all mice resembled an elliptical dome with folds, and the fissure-like abdominal opening of oviducts was observed at the center of infundibulum (Figure 1-3A-H). At 6 months, the infundibulum of MRL/lpr mice at both stages of the cycle swelled up widely in the ovarian bursa compared with that of B6 mice at each stage. When studying the surface of the infundibulum (Figure 1-3A'-H'), the author observed that it was covered by numerous ciliated epithelial cells and some secretory cells. At both estrus and anestrus, the orientation of the cilia in MRL/lpr mice showed randomized patterns. These differences were more noticeable at 6 months, and led to a rougher epithelial surface in MRL/lpr mice compared to that in B6 mice. Further, at anestrus, the numbers of ciliated epithelial cells and secretory cells covering the surface were lower and higher, respectively, in MRL/lpr mice at 6 months compared to those in MRL/lpr mice at 3 months and B6 mice at 6 months.

Discussion

First, consistent with previous reports [147], the number of both OOs and COCs was significantly higher in MRL/+-background mice compared to that in B6 mice after superovulation treatment. The process from follicular development to ovulation is ingeniously controlled by several hormones, including inhibin and activin that are produced in the ovary, or by anterior pituitary hormones [102]. In mammals, genetic traits carrying on these hormonal regulation affects the ovulation process. Therefore, high ovulation number in MRL/+-background mice thought to be derived from several genetic factors related to the ovulation process. On the other hand, a significant age-related decrease was observed in MRL/lpr mice, which manifested a severe autoimmune disease phenotype. These results indicate that the MRL/+ genomic background results in high ovulation; however, a significant age-related decrease of these features in MRL/lpr mice might be caused by autoimmune disease because of the lpr mutation in *Fas*.

With regard to ovulation, the number of OOs showed a positive correlation with the S/B and the number of T-cells in the normal control, B6 mice. Increasing evidence suggests that the success of female reproduction depends on the fine balance between inflammatory and anti-inflammatory processes and on various immune cells including T-cells [152]. Accordingly, T-cells might play a positive physiological role in murine ovulation. Further, the serum level of anti-dsDNA antibodies positively correlated with the numbers of both OOs and COCs in all mice used in the present study. The serum level of anti-dsDNA antibodies is one of the hallmarks indicating autoimmune disease progression, and this level increased significantly in 6-month mice in our study. However, these antibodies do not completely correlate with the progression of autoimmune disease [79]. Anti-dsDNA antibodies are produced by immune cells through the recognition of dsDNA derived from dead cells [27]. Therefore, the changes in systemic or local ovarian conditions through folliculogenesis and ovulation might cause the physiological increase in serum anti-dsDNA antibody levels in mice. However, the number of OOs in MRL/lpr mice negatively correlated with S/B. Moreover, Fas-mediated cell death is involved in the maintenance of follicular development in mice [104]. Taken together, an excessive immune response and/or abnormal apoptosis due to the lpr mutation might alter the ovulation function in MRL/lpr mice.

In this study, the PUR was used as the index for measuring the pick-up function of the oviduct. Our result showing that the normal control strain, B6 mice, had approximately 100% of the PUR, indicates the accuracy of this novel method for oocyte pick-up evaluation in mice. Interestingly, the PUR was over 100% in MRL/+ mice. This result leads to the speculation that several ruptured follicles could not

be found on histological sections because ovulated follicles develop into CLs more quickly in MRL/+-background mice than in B6 mice. Several studies indicate that MRL/+ mice show unique repair abilities in various tissues [38,110], suggesting the possibility that MRL/+ mice present an earlier repair process of ruptured follicles. Therefore, the author also counted the number of CLs in MRL/+-background mice, resulting in nearly 100% of the PUR in MRL/+ mice. Therefore, in MRL/+-background mice, the values of the PUR calculated including the number of CLs would be more accurate than the values calculated only with ruptured follicles. This result indicates that MRL/+-background mice have a unique ability to repair the ovulated regions in their ovary, which is investigated in detail in Chapter 3.

Remarkably, at 6 months, the PUR of only MRL/lpr mice was significantly decreased compared to that of 3-month-old mice, and showed negative correlations with indices of autoimmune disease even after the inclusion of the CL number in this calculation. This result indicates that the pick-up function was reduced with the progression of autoimmune disease. Although MRL/+ mice also showed an exacerbation of the autoimmune disease phenotype with aging, only MRL/lpr mice showed a reduction in the PUR. Therefore, only severe immune defects, such as the significant local infiltration of inflammatory cells, or abnormal apoptosis due to the lpr mutation in *Fas* might affect the pick-up function in MRL/lpr mice.

There are considerable species-specific differences in the morphology of the oviduct. For example, the infundibulum of mice is much smaller than the ovary, while that of rabbits is large enough to cover much of the ovary [29]. The infundibular smooth muscle contraction does not appear to be necessary for oocyte pick-up in rabbits [42], while this is unknown in mice. Owing to the small size of the infundibulum, it is more likely that the smooth muscle moves the infundibulum along the ovary surface in the ovarian sac in mice. Ultrastructurally, the infundibulum of MRL/lpr mice at 6 months extended widely in an abnormal manner within the ovary bursa, and this macroscopic morphological abnormality may interfere with the movement of the entire infundibulum for the finding and pick-up of oocytes. In addition to muscular contraction of infundibulum, both ciliary beating and adhesion between the oviductal epithelium and the COCs involves in oocyte pick-up [89]. In MRL/lpr mice at 6 months, the ciliated epithelial cells of the infundibulum were fewer in number than in same aged B6 mice and the arrangement of cilia was randomized. The regular swinging movement of cilia toward the ostium plays a key role in transferring oocytes into the ampulla [26,108,121], suggesting that an altered ciliary morphology in MRL/lpr mice may induce the oocyte pick-up dysfunction. Therefore, in Chapter 4, the author investigates the relationship between ciliary morphofunction and the oocyte pick-up dysfunction in

MRL/lpr mice in detail.

The decreased PUR in MRL/lpr mice suggests a failure of oocyte pick-up into the abdominal ostium of the oviduct; however, in mice, the oocytes are prevented from escaping into the peritoneal cavity because both the ovary and the oviduct are surrounded by the mesovarium, and connected by the ovarian bursa [29]. Therefore, in Chapter 2, the author investigates the anatomical features of the murine mesovarium and suggests the fate of the oocytes that fail to enter the ostium. Furthermore, the number of pups in MRL/lpr mice was similar to that in B6 and MRL/+ mice (data not shown), the accurate fertility rate was evaluated based on the oocyte pick-up rate. The author has to consider the possibility that superovulation may affect or enhance the progression of autoimmune disease or the oocyte pick-up in mice. Further studies are needed to clarify the oocyte pick-up rate in relationship to the nature of ovulation in MRL/lpr mice.

In conclusion, the author demonstrated the correlation between the progression of autoimmune disease and the function of ovulation or oocyte pick-up. Some reproductive disorders caused by unexplained causes in livestock animals would involve the oviductal dysfunction due to the altered systemic immune system. Our findings provide a new viewpoint in understanding unexplained female infertility and reproductive disorders.

Summary

Ovulation and oocyte pick-up are essential processes in fertilization. Herein, the author investigated the relationship aforementioned processes and systemic autoimmune disease. At 3 and 6 months, along with the evaluation of autoimmune disease indices, the ovary and oviduct were histologically examined in B6, MRL/+, and MRL/lpr mice as healthy control, mild and severe models of autoimmune disease, respectively. MRL/lpr mice showed early and late autoimmune disease stages at 3 and 6 months of age, respectively. In superovulated mice, the number of COCs found in the ampulla was macroscopically counted, and that of OOs were histologically evaluated, as indicated by ruptured follicles or hemorrhagic bodies in ovaries. Finally, the PUR was calculated. In MRL/lpr mice, the PUR decreased with the deterioration of diseases, unlike in other mouse strains. Further, more ovulated oocytes were found in MRL/+ mice than in B6 mice, and this number significantly decreased with aging in MRL/lpr mice. The infundibulum in aged MRL/lpr mice showed swelling and decreased ciliated epithelial cells compared to that of B6 mice. In conclusion, the author developed the novel method to evaluate murine oocyte pick-up function. In addition, these results in Chapter 1 revealed that the progression of severe autoimmune disease disturbed the ovulation and oocyte pick-up process with pathological changes of the infundibulum.

Tables and Figures

Table 1-1. Spearman's correlation coefficient (ρ) between the number of ovulated oocytes or cumulus oocyte complexes, or oocyte pick-up rate and the autoimmune disease parameters

	Strains	Parameters		
		S/B	T-cells in ovary	Anti-dsDNA antibody
OOs	All mice (+CL)	-0.100 (-0.074)	0.084 (0.071)	0.505^{**} (0.608^{**})
	B6	0.627^{**}	0.676^{**}	0.344
	MRL/+ (+CL)	0.414 (0.568)	-0.031 (-0.139)	-0.261 (-0.271)
	MRL/lpr (+CL)	-0.428^{*} (-0.512^{*})	-0.062 (-0.214)	0.366 (0.387)
COCs	All mice	0.051	-0.061	0.525^{**}
	B6	0.294^{*}	0.559^{*}	0.055
	MRL/+	0.013	-0.188	-0.271
	MRL/lpr	-0.559^{**}	-0.322	0.395
PUR	All mice (+CL)	-0.640^{**} (-0.670^{**})	-0.548^{**} (-0.608^{**})	-0.003 (-0.403^{**})
	B6	-0.047	-0.208	-0.278
	MRL/+ (+CL)	-0.089 (0.051)	-0.134 (-0.212)	-0.025 (-0.074)
	MRL/lpr (+CL)	-0.640^{**} (-0.465^{*})	-0.471^{*} (-0.291)	0.466^{*} (0.425)

*: $P < 0.05$, **: $P < 0.01$. B6: C57BL/6; MRL/+: MRL/MpJ; MRL/lpr: MRL/MpJ-Fas$^{lpr/lpr}$; OO: ovulated oocyte; COC: cumulus oocyte complex; PUR: oocyte pick-up rate; +CL: values when the number of corpus luteum is accounted; S/B: spleen weight to body weight ratio; dsDNA: double-stranded DNA.

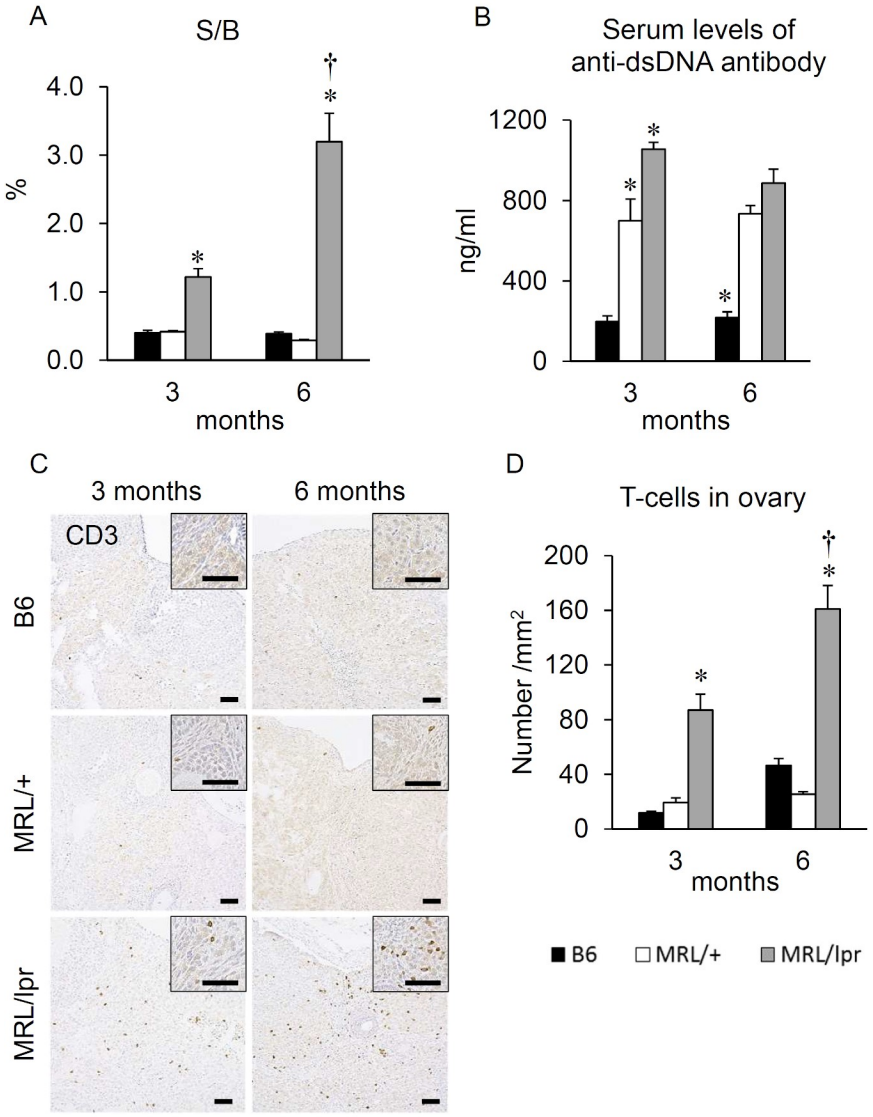

Figure 1-1. Autoimmune disease indices of mice at 3 and 6 months.
(A) Spleen weight to body weight ratio (S/B).
(B) Serum levels of anti-double-stranded DNA (dsDNA) antibody.
(C) Localization of CD3-positive T-cells in mouse ovaries. Immunohistochemistry. Insets show magnified ovarian interstitium. Numerous positive cells are observed in the MRL/lpr mouse ovary, especially at 6 months of age. Bars = 50 μm.
(D) Number of CD3-positive T-cells in mouse ovaries.
Data are the mean ± SE (n ≥4). *: comparison with the other strains at the same age (Kruskal–Wallis test followed by Scheffé's method, $P < 0.05$). †: significant age-related difference in the same strain (Mann-Whitney *U*-test, $P < 0.05$). B6: C57BL/6N, MRL/+: MRL/MpJ, MRL/lpr: MRL/MpJ-Fas$^{lpr/lpr}$.

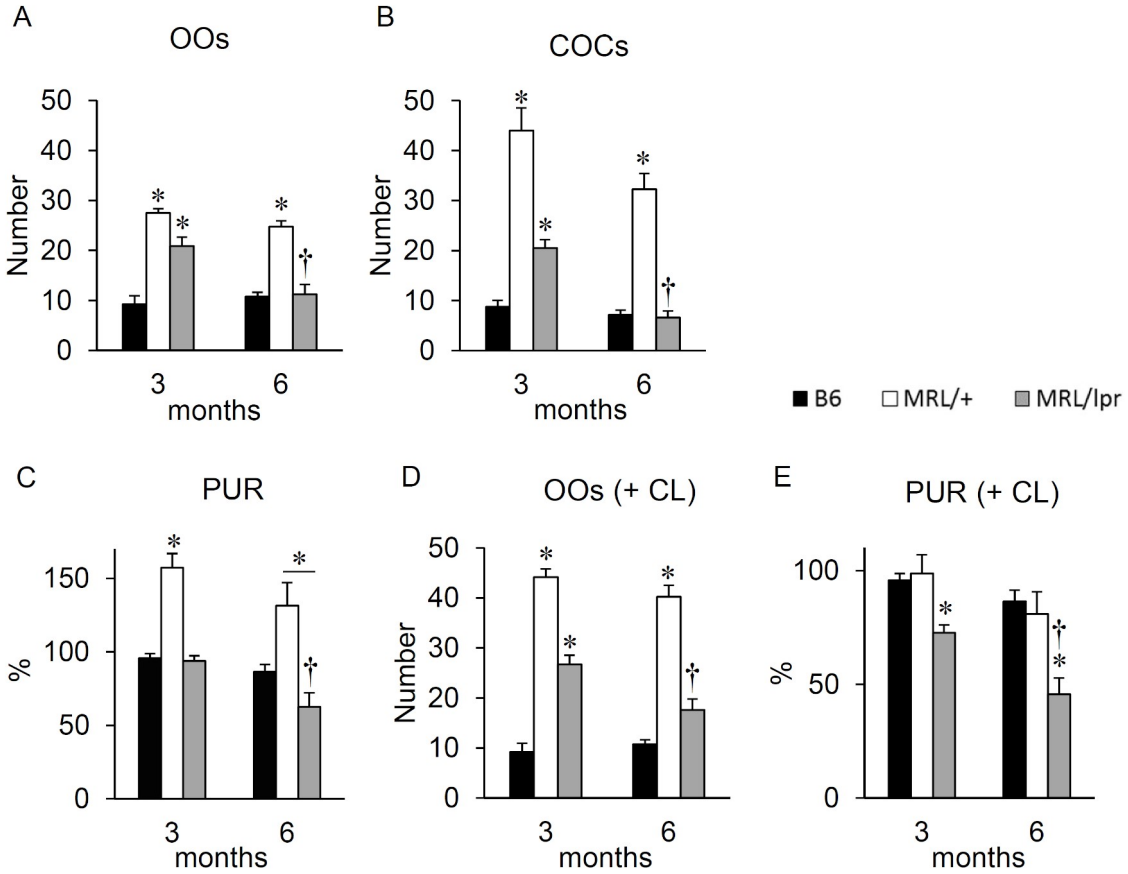

Figure 1-2. Ovulation and oocyte pick-up indices of mice at 3 and 6 months.
(A) Number of ovulated oocytes (OOs).
(B) Number of cumulus oocyte complexes (COCs).
(C) Oocyte pick-up rate (PUR).
(D) Number of OOs in MRL/+ and MRL/lpr mice included the number of corpus luteum (CL).
(E) PUR calculated from **(D)**.
Data are the mean ± SE (n ≥4). *: comparison with the other strains at the same age (Kruskal–Wallis test followed by Scheffé's method, $P < 0.05$). †: significant age-related difference in the same strain (Mann-Whitney *U*-test, $P < 0.05$). Line in graph **(C)** indicates significant. B6: C57BL/6N, MRL/+: MRL/MpJ, MRL/lpr: MRL/MpJ-Fas$^{lpr/lpr}$.

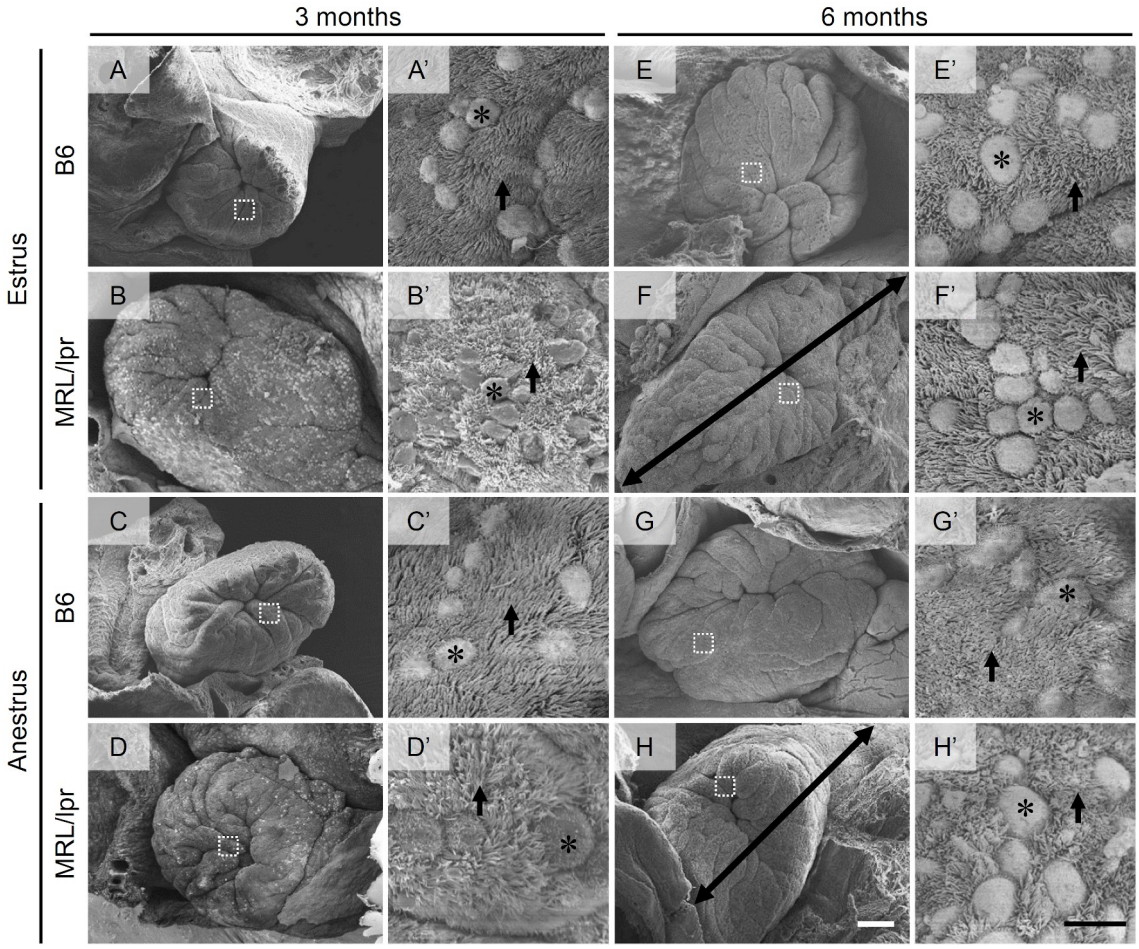

Figure 1-3. Ultrastructural differences in the infundibulum in mouse oviducts among different estrus stages, strains, and ages.

(A-H) Morphological features of the infundibulum at estrus and anestrus stages in B6 and MRL/lpr mice are shown by scanning electron microscopy. As shown using bidirectional arrows in **(F and H)**, in MRL/lpr mice at 6 months of age, the infundibulum expands in the ovarian bursa. The white squares in **(A-H)** are magnified in **(A'-H')**, respectively.

(A'-H') The epithelium is covered with abundant cilia (arrows), and some secretory cells are observed (asterisks).

White bar = 100 μm. Black bar = 10 μm. B6: C57BL/6N, MRL/+: MRL/MpJ, MRL/lpr: MRL/MpJ-Fas$^{lpr/lpr}$.

Chapter 2

Anatomy and histology of the foramen of ovarian bursa opening to the peritoneal cavity and its changes in autoimmune disease-prone mice

Introduction

In Chapter 1, the author revealed that MRL/lpr mice suffer a reduction in oocyte pick-up by the oviductal infundibulum, resulting due to the progression of their systemic autoimmune conditions. Furthermore, it was also revealed that the ruptured follicles and hemorrhagic bodies counts in whole-serial-sectioned ovaries, accounting for OOs, exceeded the count of COCs in the oviductal ampulla picked-up by the oviductal infundibulum of MRL/lpr mice at 6 months of age with severe autoimmune abnormalities. These results indicate the possibility that the oocytes which progress into the ovarian bursa of mice are expelled into the peritoneal cavity through the small peritoneal opening in the ovarian bursa. However, only a few anatomical and histological studies of the murine ovarian bursa are available to confirm this hypothesis. Hence, in this Chapter, the author visualized and analyzed the structure of the ovarian bursa of three murine models: B6, MRL/+, and MRL/lpr mice at 3 and 6 months of age.

The ovaries originate from the gonadal primordium, located in the lumbar region on the medial surface of mammalian mesonephros [66]. Moreover, the oviducts and uterus develop from the Müllerian ducts [142] and play crucial roles in female reproduction. The ovaries and oviducts are suspended within the mesovarium and mesosalpinx, respectively. These are the cranial parts of the broad ligament, ligamentum latum uteri, which is the common double-folded suspension of the mammalian female genital tract to the abdominal wall [66]. The ovarian ligaments and the proper ligament of the ovary, *ligamentum ovarii proprium*, connect each ovary to the lateral side of the uterus [23]. The mesovarium, mesosalpinx, and the proper ligament of the ovary enclose a small peritoneal cavity, termed the ovarian bursa, *bursa ovarica*, which surrounds the ovary and oviductal infundibulum [66].

The anatomical characteristics of the ovarian bursa, as well as ovulation rates, vary depending on the animal species. In cows, ovulation produces one oocyte at a time [95], and the mesosalpinx surrounds the ovary like a mantle and forms a voluminous ovarian bursa with a wide cranio-ventromedial opening [10]. In mares, ovulation produces one oocyte at a time [36], and the ovary is too large to be located within the ovarian bursa [66]. In female dogs, multiple ovulations produce about 5 to 7 oocytes at a time [82], and the ovarian bursa completely encompasses the ovary within the foramen of ovarian bursa (FOB, *foramen bursae ovaricae*), which is a narrow slit-like opening to the peritoneal cavity [66]. Female human have no bursal structure around the ovaries [8,87]. Finally, in mice, the ovulation rate is about eight at once, although the ovulation rate

varies depending on the mouse strain [95], the ovaries are completely surrounded by the ovarian bursa, which has a small peritoneal opening [137].

The ovarian bursa is thought to play a role in preventing ovulated oocytes from escaping into the peritoneal cavity, thus facilitating the transport of ovulated oocytes into the oviduct and assisting effective fertilization [153]. Furthermore, surgical removal of the ovarian bursa surrounding the ovary of rodents leads to a reduction in the number of oocytes picked-up by the oviductal infundibulum within the oviduct [59,132]. Based on the aforementioned anatomy and function of the murine ovarian bursa, it has been suggested that the oocytes produced in the ovaries rarely escape into the peritoneal cavity in mice.

In this Chapter, based on the anatomical and histological examinations of the mesovarium and mesosalpinx, all strains were confirmed to have the FOB within the mesosalpinx connecting oviduct and uterus. The author also found the histological characteristics of the mesosalpinx surrounding the FOB, which is named the ligament of FOB (LOB). Moreover, the LOB differs from other parts of the mesosalpinx, as the LOB is partially lined with cuboidal mesothelial cells and consists of a thick smooth muscle layer in all strains. In 6-month-old MRL/lpr mice with severe autoimmune disease, although the LOB prevented the infiltration of immune cells, it showed fibrosis; moreover, the FOB size in some of these mice was markedly larger than that of other strains and 3-month-old MRL/lpr mice. These results provide insight on the fate of the oocytes that fail to enter the ostium in MRL/lpr mice.

Materials and Methods

Animals

Animal experimentation was approved by the Institutional Animal Care and Use Committee of the Graduate School of Veterinary Medicine, Hokkaido University (Approval No.15-0079), and the School of Veterinary Medicine, Rakuno Gakuen University (Approval No. VH19A6). Animals were handled in accordance with the Guide for the Care and Use of Laboratory Animals, Graduate School of Veterinary Medicine, Hokkaido University, Japan (approved by the Association for Assessment and Accreditation of Laboratory Animal Care International), and with the Guide for the Care and Use of Laboratory Animals, Rakuno Gakuen University, Japan. Female B6, MRL/+, and MRL/lpr mice at 3 and 6 months of age were obtained from Japan SLC, Inc. The estrous cycle of each mouse was confirmed by monitoring vaginal smears. The housing and euthanization of mice were performed as done in Chapter 1.

Stereomicroscopical and histological observation of mice female reproductive tract

The experiment was performed in Rakuno Gakuen University. The female reproductive tract, including ovaries, oviducts, and a cranial part of the uterus were collected from mice. The morphology of these organs kept in 0.01M PBS and were observed under a stereo microscope. After observation, the organs were fixed with 4% PFA at 4°C overnight, embedded in paraffin, and cut into 3 μm-thick sections for immunohistochemistry and Masson's trichrome staining (MT).

India ink injection into the ovarian bursa

The experiment was performed in Rakuno Gakuen University. The female reproductive tract, including ovaries, oviducts, and a cranial part of the uterus, were collected from mice. A total of 10 to 20 μL India ink was injected into the ovarian bursa by inserting a glass capillary or 35G needles, and the leakage of India ink through the FOB was observed.

Ultrastructural analysis of mice female reproductive tract

The experiment was performed in Rakuno Gakuen University. For SEM, the female reproductive tract, including ovaries, oviducts, and a cranial part of the uterus were removed from mice during the estrus cycle and fixed using half-strength Karnovsky's fixing solution. After six

washes in 0.1 M PB, these organs were post-fixed with 1% osmium tetroxide in 0.1 M PB for 2 h at room temperature. After six washes in distilled water, the specimens were subjected to conductive treatment by 5% BEL-1 (Nisshin EM Co. Ltd., Tokyo, Japan) in 70% ethanol for 2 h at room temperature. Specimens were dried completely and examined using a S-2460N scanning electron microscope (Hitachi, Tokyo, Japan). Samples were sputter coated with gold using the ion-sputter E102 (Hitachi).

Area measurement of the opening of ovarian bursa using three-dimensional reconstruction

The experiment was performed in Rakuno Gakuen University. The ovaries, oviducts and the cranial part of the uterus were collected from mice during estrus. These organs were fixed with 4% PFA and kept at 4°C overnight. They were then embedded in paraffin and cut into 12 μm-thick whole serial sections. The serial hematoxylin and eosin-stained sections were used for both the histological observation and the three-dimensional (3D) reconstruction of the female reproductive organs. The 3D reconstruction was processed using Fiji software, which is an image processing package of ImageJ (National Institutes of Health, Bethesda, Maryland, USA), and Image Pro software (Media Cybernetics Inc., Rockville, Maryland, USA). The alignment of each pictured section in whole serial sections was adjusted by the Register Virtual Stack Slices plugin provided in Fiji (National Institutes of Health). Based on these aligned 2D pictures of the female reproductive tract, 3D geometrical models of female reproductive tracts were created using the Image Pro software (Media Cybernetics Inc.). The peritoneal side of the FOB observed in these 3D models was measured using Image Pro software (Media Cybernetics Inc.).

Immunohistochemistry

The experiment was performed in Hokkaido University. Immunohistochemistry was performed as done in Chapter 1. The 3 μm-thick sections of female reproductive organs of mice during estrus were used. For antigen retrieval, 20 mM tris-HCl (pH 9.0) (for B220, B cell marker; CD3, T cell marker; Foxp3, regulatory T cell marker), or 10 mM citrate buffer (pH 6.0) (for Iba1, macrophage marker; Lyve1, lymphatic vessel marker; alpha smooth muscle actin (αSMA), smooth muscle cell marker) were used. After washing and blocking, sections were incubated with rat anti-B220 (1:1600, Cedarlane, Ontario, Canada), rabbit anti-CD3 (ready to use, Nichirei Bioscience Inc., Tokyo, Japan), rabbit anti-Iba1 (1:1,200, FUJIFILM Wako Pure Chemical Co.,

Ltd., Osaka, Japan), rat anti-Foxp3 (1:100, Thermo Fisher Scientific K.K., Tokyo, Japan), rabbit anti-Lyve1 (1:500, AdipoGen Inc., San Diego, California, USA) or rabbit anti-αSMA (1:3,000, Abcam Co. Ltd., Cambridge, UK). After washing, sections were incubated with biotin-conjugated goat anti-rabbit IgG (SABPRO Kit, Nichirei Co., Ltd., Tokyo, Japan), or goat anti-rat IgG antibody (1:150, BioLegend Inc., San Diego, California, USA). After washing, sections were incubated using a streptavidin-biotin complex. Sections were then incubated with 3, 3′ – diaminobenzidine tetrahydrochloride-H_2O_2 solution, and lightly stained with hematoxylin.

Statistical analysis

Results are expressed as the mean ± SE. Statistical analysis was performed as done in Chapter 1.

Results

The morphology of the peritoneal opening of the ovarian bursa of mice

Under the stereomicroscope, it was found that there was common positional anatomy of the female reproductive tract among the three strains at both ages, and both the left and right ovaries were located on the cranial side of the oviducts, folded like a coil connecting to the uterus (Figure 2-1). Most parts of the ovaries in all mice were covered by continuous mesovarium and mesosalpinx. Notably, MRL/+ mice at 6 months of age developed ovarian cysts (Figure 2-1) [65]. In the magnified stereomicroscopical observations, the oviducts folded like a coil by the mesosalpinx were clearly observed in the female reproductive tract of all strains. The coiled oviducts were connected to the cranial part of the uterus by the mesosalpinx, which surrounded the slit-shaped peritoneal openings in the ovarian bursa. Both the left and right ovaries had peritoneal openings generally less than 1 mm in length, which were commonly observed at the same position of the female reproductive tract of all strains at both ages. The slit-shaped peritoneal opening in the ovarian bursa of the mouse is named the FOB, based on the anatomical vocabulary of the narrow slit-like opening observed in the ovarian bursa of female dogs [66]. The mesosalpinx surrounding the murine FOB is named the LOB (ligament of ovarian bursa). Some, but not all, of the ovarian bursa of the 6-month-old MRL/lpr mice exhibited a larger FOB than that of other individuals. Furthermore, the oviductal infundibulum enclosed the ovarian bursa and was observed from the peritoneal side, as shown in the FOB of the right side ovaries of MRL/lpr mice at 6 months of age in Figure 2-1. The India ink injected into the ovarian bursa leaked through the FOB in the three strains at both ages (Figure 2-2 and Movie 2-1).

The ultrastructure of FOB was also observed in all strains (Figure 2-3). As shown through stereomicroscopical observations, the FOB in mice was surrounded by the LOB, which was slit-shaped or had a slightly expanded ellipsoid shape. Furthermore, mesothelial cells lining the LOB in B6 and MRL/+ mice exhibited spherical dome-like morphology (Figure 2-3, arrowheads in insets). In MRL/lpr mice, the mesothelium of the LOB had a deeply tangled surface. The ultrastructural differences of the FOB between the left and right sides were not observed.

The female reproductive tract reconstructed in 3D by superimposing the images of their whole serial sections reproduced the morphology of the FOB in the mesothelium (Figure 2-4A). Furthermore, the author measured the peritoneal side area of the FOB (Figure 2-4B). Although the area was approximately 0.04 to 0.12 cm^2 and had no significant differences among strains at

both 3 and 6 months of age, MRL/lpr mice at 6 months of age tended to have a larger FOB size than other strains at the same age.

The histology of the LOB of mice

The presence of the FOB in all strains was confirmed in the histological sections shown in Figure 2-5. The whole serial sections of the female reproductive tract of mice revealed that the ovarian bursa did not have apertures that were continuous with the peritoneal cavity, other than the FOB (data not shown). This histological observation also showed that the FOB was surrounded by the LOB connecting the isthmus or ampulla of the oviducts and the cranial part of the uterus. The epithelium of the LOB facing the FOB was lined with mesothelial cells, which were, in part, cuboidal epithelial cells (Figure 2-5). Significant histological differences in the LOB were not observed among the strains at both 3 and 6 months of age and the left and right sides.

The distribution of smooth muscle cells and collagen fibers in the LOB of mice

Immunohistochemical analysis identified smooth muscle cells as the cell types that compose the connective tissue under the epithelium of the LOB (Figure 2-6). To examine the distribution of the collagen fibers in the LOB, MT staining was performed (Figure 2-6, MT). In the LOB of B6 mice at both 3 and 6 months of age, the thick collagen fibers were distributed underneath the mesothelium and between smooth muscle layers (Figure 2-6). In the LOB of MRL/+ mice at 3 and 6 months of age, as well as in MRL/lpr mice at 3 months of age, the distribution of thick collagen fibers was not significant. However, it was observed that the thick and dense aniline blue^{+} collagen fibers were distributed underneath the mesothelium and partially between the smooth muscle layers in the LOB of MRL/lpr mice, at 6 months of age (Figure 2-6).

The distribution of immune cells in the LOB of mice

To examine the effect of the inflammation in the LOB of the mice, the author performed immunohistochemistry to detect B cells, T cells, macrophages, and regulatory T cells. In the mesosalpinx folding the isthmus, there was marked infiltration of immune cells, including B220-positive B cells, CD3-positive T cells, and Iba1-positive macrophages (Figure 2-7). In MRL/lpr mice at both 3 and 6 months, compared to the other strains, a larger distribution of Foxp3-positive regulatory T cells was observed (Figure 2-7). The infiltration of the immune cells was more

profound in MRL/lpr mice at 6 months of age than at 3 months of age. However, no marked distribution of B220-positive B cells, CD3-positive T cells, Iba1^{+} macrophages, or Foxp3-positive regulatory T cells in the LOB was observed in any of the mice used in this study (Figure 2-8). The lymphatic vessels, visualized by the Lyve1-positive reaction, were distributed directly underneath the LOB, as well as in the connective tissue of the LOB, in all strains at 3 and 6 months of age. The number of these immune cells and lymphatic vessels in the LOB exhibited no differences among the strains at 3 and 6 months of age

Discussion

Over 70 years ago, Wimsatt and his colleagues reported for the first time that a peritoneal opening generally appears in the ovarian bursa of B6 and Swiss strain of mice [137]. However, the rather small morphology of the FOB, which is rarely observed in the histological section of female reproductive tracts, led to misinterpretations in several reports which stated that mice have a ovarian bursa with no peritoneal opening, with completely enveloped ovaries [8,21,22,30,59]. This study confirmed and revealed that both B6 and MRL-background strains of mice have peritoneal openings in the ovarian bursa, indicating that the FOB surrounded by the LOB, which connects the oviduct and the cranial part of the uterus, is the general female reproductive structure in mice (Figure 2-9). As for other rodents, rats also have a small opening in the ovarian bursa to the peritoneal cavity [60]. However, in golden hamsters, each ovary has been reported to be enclosed within a complete bursa that is connected with the oviduct [22,77,109]. Interestingly, the monotocous species possess neither a bursa (as in the case of the female human) nor an ovarian bursa that is strongly connected with the peritoneal cavity (as in the cases of the mare and cow), but polytocous species possess an almost complete ovarian bursa (as in the cases of the rodents) [59]. The anatomical characteristics of the mammalian ovarian bursa can provide key information to explain the biological and evolutional differences in their reproduction.

The almost closed appearance of the murine ovarian bursa has been used for the intrabursal injection technique, which is a method of topical drug delivery to ovaries by the injection of a solution into the bursal cavity of an anesthetized animal [77,131]. It is also used as the method for selective introduction of genetic information to alter the ovarian surface epithelium [17,59]. However, it has been suggested that the ovarian bursa may play an active role in regulating local fluid homeostasis during the ovulation [153]. The intrabursal fluid interchange is thought to be bidirectional between the peritoneal cavity and the reproductive tract through the FOB. This rationale is based on the observation that particles of India ink, which was injected into the peritoneal cavity of mice, were found to be abundantly present in the ovarian bursa and oviduct during the ovulation period [137]. Although the author examined the FOB and LOB of the mice at estrus in this study, further studies using mice at various stages in the estrous cycle can help to reveal additional morphological differences between the FOB and LOB. Furthermore, the author found that the LOB possesses a thick, smooth muscle layer, which indicates that the FOB alters its area depending on the physiological, hormonal, and pathological conditions of the female

reproductive tract by contracting the LOB. Therefore, in order to get accurate results, the selection of an optimal injection time, while taking into consideration the stage of the estrous cycle and/or light-dark cycle, as well as the consistency of the injection timing through a series of experiments is important for researchers who perform intrabursal injections.

The ovarian bursa is a key player in maintaining an adaptive ovarian microenvironment for ovulation [72]. Lymphatic stomata are small openings in lymphatic capillaries on the free surface of the mesothelium [135]. The ovarian bursa of the golden hamster has lymphatic stomata that connects the bursal cavity with the lymphatic lumen [109]. It is suggested that the opening area of lymphatic stomata varies under different fluid pressure and mechanical forces [72]. In addition to these theories, the muscular structure of the LOB surrounding the FOB provides us with a novel hypothesis that the contraction of the FOB also plays a role in maintaining the bursal liquid and/or hormonal homeostasis, by discarding the bursal liquid into the peritoneal cavity.

The peritoneum is composed of an extensive squamous or cuboidal monolayer of mesothelial cells that rests on the fibrous connective tissue underneath [53,150]. The cuboidal mesothelial cells appear in the septal folds of the mediastinal pleura, liver, and spleen, and are in a metabolically active state [84]. The peritoneum facilitates immune induction, modulation, and inhibition, as the mesothelial cells are capable of recognizing pathogens and tissue damage, and initiating inflammatory responses through antigen presentation, cytokine production, and interaction with immune cells, such as macrophages [53]. In swine, mesothelial cells covering the ovarian bursa are cuboidal and biosynthetically activated, which suggests that these mesothelial cells may produce large amounts of surfactants and regulate immunomodulation, fluid balance, lubrication, and protection [146]. The author reports that the epithelium of the LOB in mice is partially lined with such cuboidal mesothelial cells. Hence, the LOB might have the unique function to regulate intrabursal immune balance and thereby promote healthy reproductive processes in the ovary. Previous studies and the results in Chapter 1 reported that autoimmune disease in female MRL/lpr mice is severely exacerbated at 6 months of age, and the severe inflammation due to the infiltration of immune cells affects the ovaries. In this Chapter, the lymphoma-like infiltration of inflammatory cells, including B cells, T cells, and macrophages was observed in the mesosalpinx folding the isthmus in MRL/lpr mice at 6 months of age. However, this was not observed in the LOB, thereby suggesting a higher ability of the LOB to regulate immune conditions compared to typical mesosalpinx. Further investigations will be needed to confirm these hypotheses.

Notably, as shown in Chapter 1, the MRL/lpr at 6 months of age with severe autoimmune conditions lose their ovulated oocytes into the coeloma, which is neither the ovarian bursa nor the oviductal lumen. The diameter of mouse oocytes is approximately 80 μm [141]. Based on our findings that the area of FOB in mice was approximately 0.04 to 0.12 cm^2, and given smooth muscle contraction in the LOB might change the area of the FOB, it is hypothesized that the oocytes released from the ovaries into the ovarian bursa can escape into the peritoneal cavity through the FOB in mice with autoimmune issues. In MRL/lpr mice in the severe disease stage, some of which possessed larger than average FOB relative to other strains and individuals, the altered morphology and function of the FOB might be one of the causes for the dysfunction of oocyte pick-up, in addition to the abnormal morphology in the oviductal infundibulum. In the animals possessing the ovarian bursa strongly connecting with the peritoneal cavity, the oocytes produced from ovaries are thought to easily escape into the peritoneal cavity when the morphofunction of the oviductal infundibulum is impaired.

The chronic inflammatory reactions triggered by persistent infections, autoimmune reactions, allergic responses, and tissue injury result in fibrosis [140]. In addition organs such as lungs, heart, liver, kidney, intestine, and skin [140], the peritoneum is also pathologically affected by chronic inflammation and fibrosis [134]. Even in MRL/lpr mice at 6 months of age which have severe inflammation in the mesosalpinx, there were only a small number of immune cells infiltrating the LOB. Nonetheless, the inflammation enhances fibrosis in the LOB in MRL/lpr mice at 6 months of age, compared to 3 months of age, and MRL/+ at both ages. Once initiated, fibrogenesis in the intestine is no longer dependent on the presence of inflammation, suggesting that the fibrosis is self-propagating [55]. Although inflammation is prerequisite for the initiation of fibrosis, the severity of inflammation during fibrogenesis does not correlate with the degree of collagen deposition [47]. Therefore, the author considers that the severe and chronic systemic immune abnormalities, which deteriorate in the later life of MRL/lpr mice, alter the hormonal environment post-ovulation and immunological microenvironment, including cytokines in female reproductive organs. This leads to the deposition of thick collagen fibers in MRL/lpr mice at 6 months of age. The ultrastructure of the surface of the LOB revealed highly complicated LOB in MRL/lpr mice, which corresponds with the histological observation of thick collagen deposition underneath the mesothelium. Although it is unclear whether fibrosis affects the function of the LOB and morphology of the FOB, considering that B6 mice also possess the fibrotic LOB at both 3 and 6

months of age, the deposition of collagen fibers in MRL/lpr mice in the severe disease stage might make the LOB stiffer than at younger ages. This can occur as organs increase their extracellular matrix (ECM), which contains fibrillar collagens [136], thus resulting in a stiffer LOB. Repeated ovulation induces an acute pro-inflammatory environment on the ovarian surface and oviductal fimbria, increasing ovarian cancer risk [124]. Although the ovulation rate of B6 and MRL strain mice is similar (about 10 oocytes per estrus), the impaired clearance of intrabursal fluid containing inflammatory substances derived from ovarian follicles would cause pathology not only of the ovaries but also of the oviducts. The stiffer LOB perhaps affects the ovarian pathology due to impaired bursal fluid regulation in mice. On the other hand, in cows which have ovarian bursa widely opening to the pelvic cavity, the inflammatory environment abdominal or pelvic cavity can directly impact on the ovary and oviduct, as suggested by the fact that peritonitis relates to the ovaro-bursal adhesions in cows [81].

In conclusion, the ovarian bursa of mouse is connected to the peritoneal cavity, which is a characteristic similar to those of other mammals, such as ruminants and horses. The author also reports the physiological function of the LOB with a thick, smooth muscle layer in the maintenance of the fluid microenvironment and immune condition around the ovary. Furthermore, in MRL/lpr mice with severe autoimmune disease, the alternation of the physiological function of the LOB and the size of the FOB is suggested to influence on the healthy ovulation and oocyte pick-up by the oviductal infundibulum.

Summary

The results in Chapter 1 indicate the possibility of an escape of ovulated oocytes into the peritoneal cavity, despite the presence of an almost complete ovarian bursa in the mouse. The ovarian bursa is a small peritoneal cavity enclosed by the mesovarium and mesosalpinx, which surrounds the ovaries and oviductal infundibulum in mammals. The ovarian bursa is considered as the structure facilitating the pick-up and transport of ovulated oocytes into the oviduct. To verify this possibility, in Chapter 2, the author investigated the anatomical and histological characteristics of the ovarian bursa of B6, MRL/+, and MRL/lpr mice at 3 and 6 months of age. As a result, all strains had the FOB, with a size of approximately 0.04 to 0.12 cm^2, surrounded by the LOB, which is part of the mesosalpinx. The LOB was partially lined with the cuboidal mesothelial cells and consisted of a thick smooth muscle layer in all strains. In 6-month-old MRL/lpr mice, in which the systemic autoimmune abnormality deteriorated and oocyte pick-up function was impaired, the size of the FOB tended to be larger than that of other strains. Additionally, in MR/lpr mice at 6 months of age, there was infiltration by numerous immune cells in the mesosalpinx suspending the isthmus; however, the LOB prevented severe inflammation and showed deposition of collagen fibers. These results not only indicate that the FOB is a common structure within mice, but also imply the physiological function of the LOB and its role in maintaining the microenvironment around the ovary, as well as regulating healthy reproduction. In MRL/lpr mice with severe autoimmune disease, the structural changes of the FOB and the functional changes of the LOB are thought to influence on the pick-up process of ovulated oocytes.

Figures

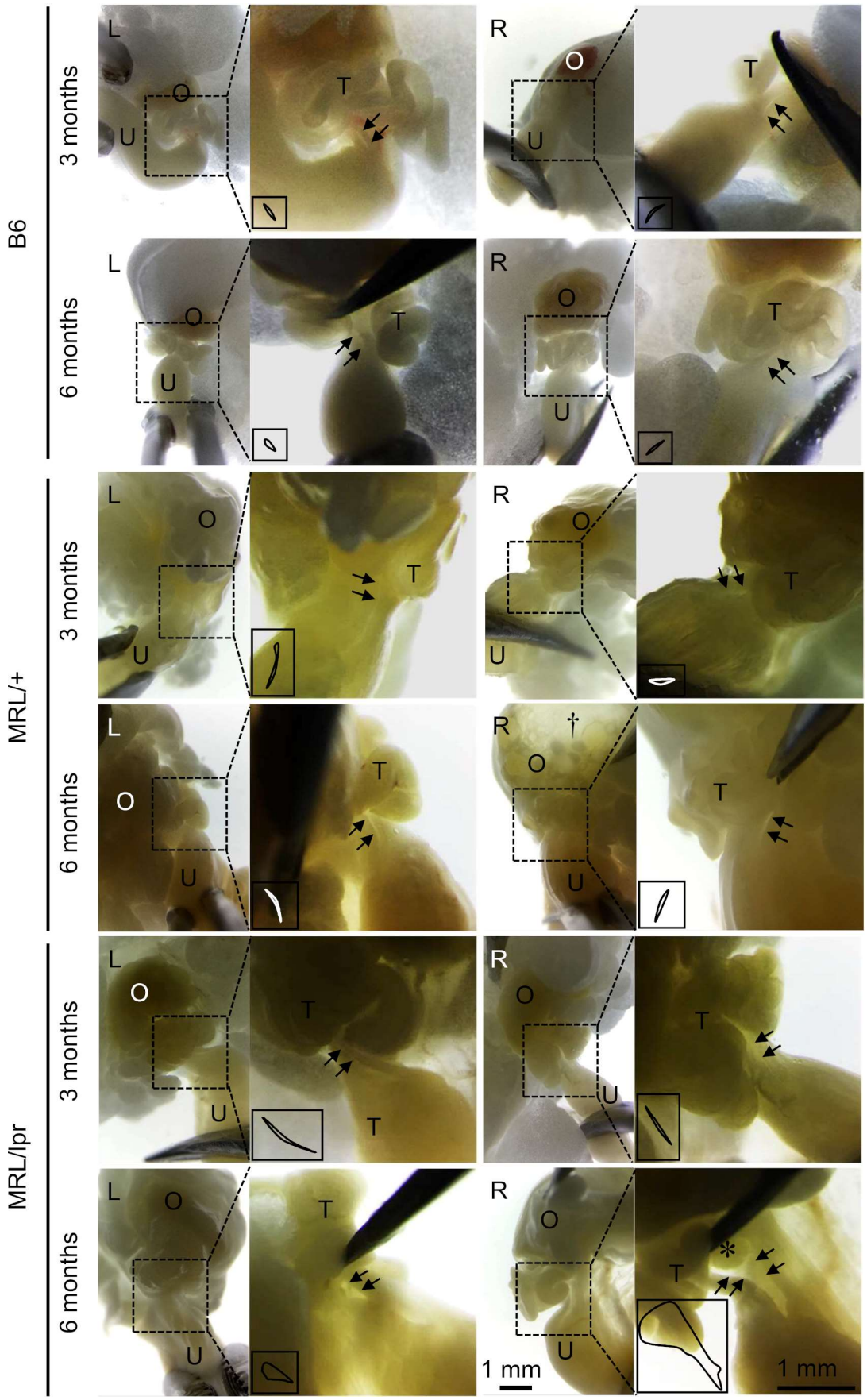
B6
MRL/+
MRL/lpr
3 months
6 months
L
R
O
U
T
†
*
1 mm
1 mm

Figure 2-1. The stereomicroscopical morphology of the foramen of the ovarian bursa in mice. Arrows show the positions of the foramen of the ovarian bursa. The squares surrounded by dashed lines are magnified in images on the right side. The line drawings in the insets imitate the shape of the foramen of the ovarian bursa. Asterisk shows the infundibulum enveloped in the ovarian bursa of MRL/lpr mice at 6 months of age.
L: left, R: right, O: ovary, T: oviduct, U: uterus, †: ovarian cyst. B6: C57BL/6N, MRL/+: MRL/MpJ, MRL/lpr: MRL/MpJ-Fas$^{lpr/lpr}$.

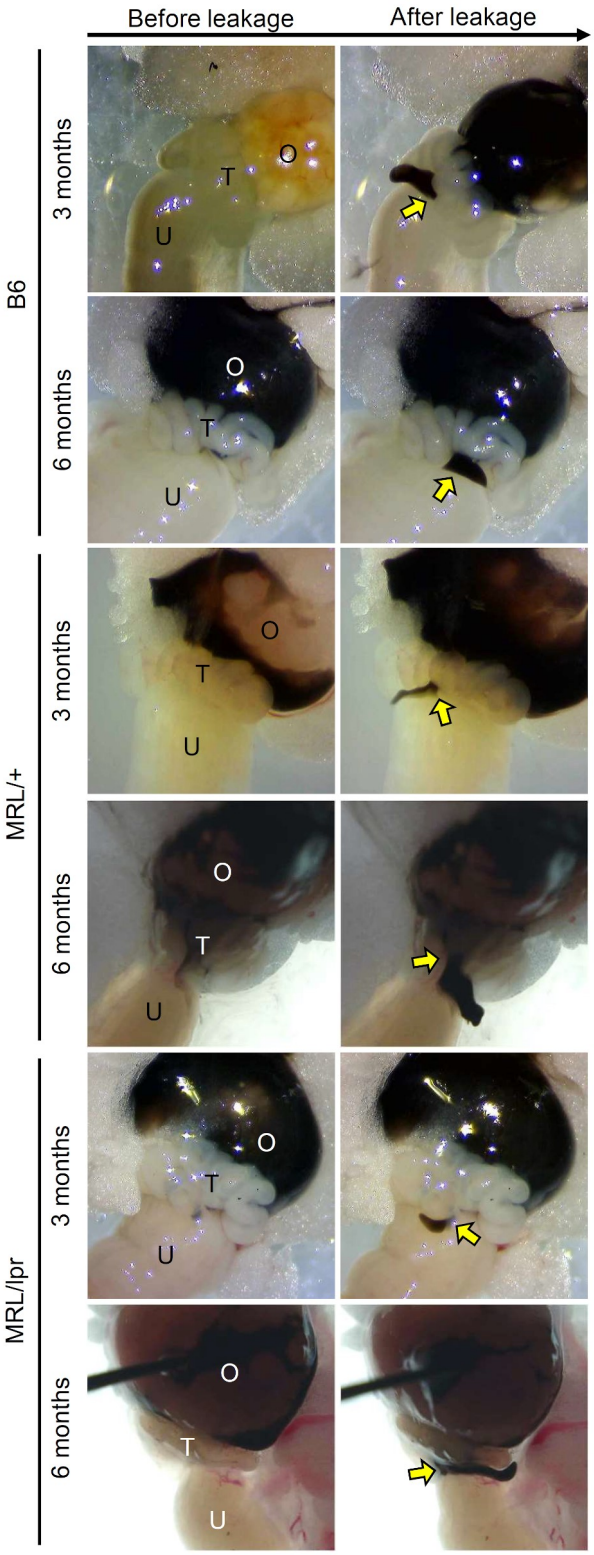

Figure 2-2. Leakage of India ink from the ovarian bursa to extrabursa through the foramen of the ovarian bursa in mice.
Arrows indicate the points where the India ink leaked (i.e., foramen of the ovarian bursa).
O: ovary, T: oviduct, U: uterus. B6: C57BL/6N, MRL/+: MRL/MpJ, MRL/lpr: MRL/MpJ-Fas$^{lpr/lpr}$.

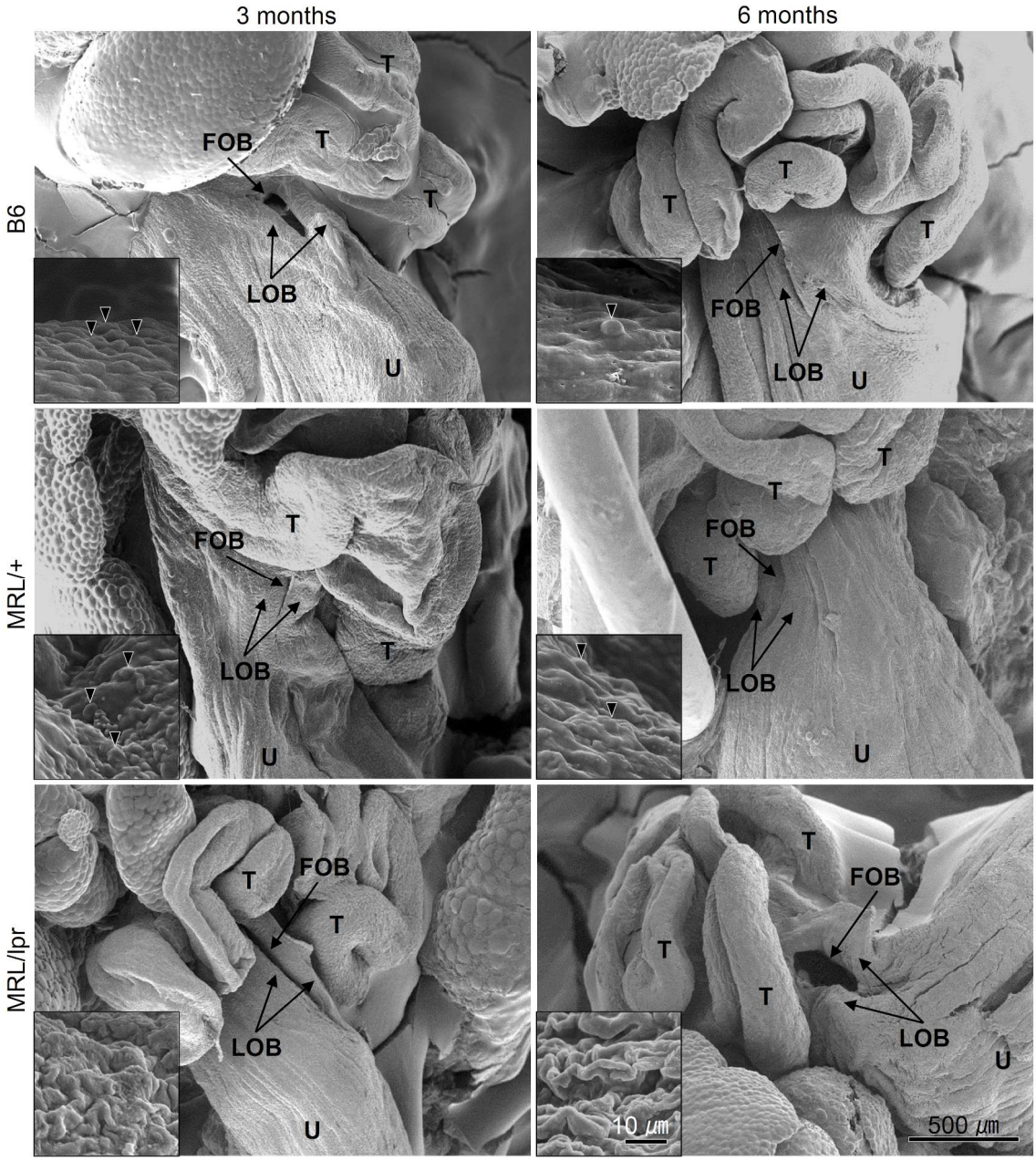

Figure 2-3. The ultrastructure of the foramen of ovarian bursa in mice.
Arrowheads indicate the spherical dome like mesothelial cells lining the LOB.
T: oviduct, U: uterus, FOB: foramen of ovarian bursa, LOB: ligament of ovarian bursa. B6: C57BL/6N, MRL/+: MRL/MpJ, MRL/lpr: MRL/MpJ-Fas$^{lpr/lpr}$.

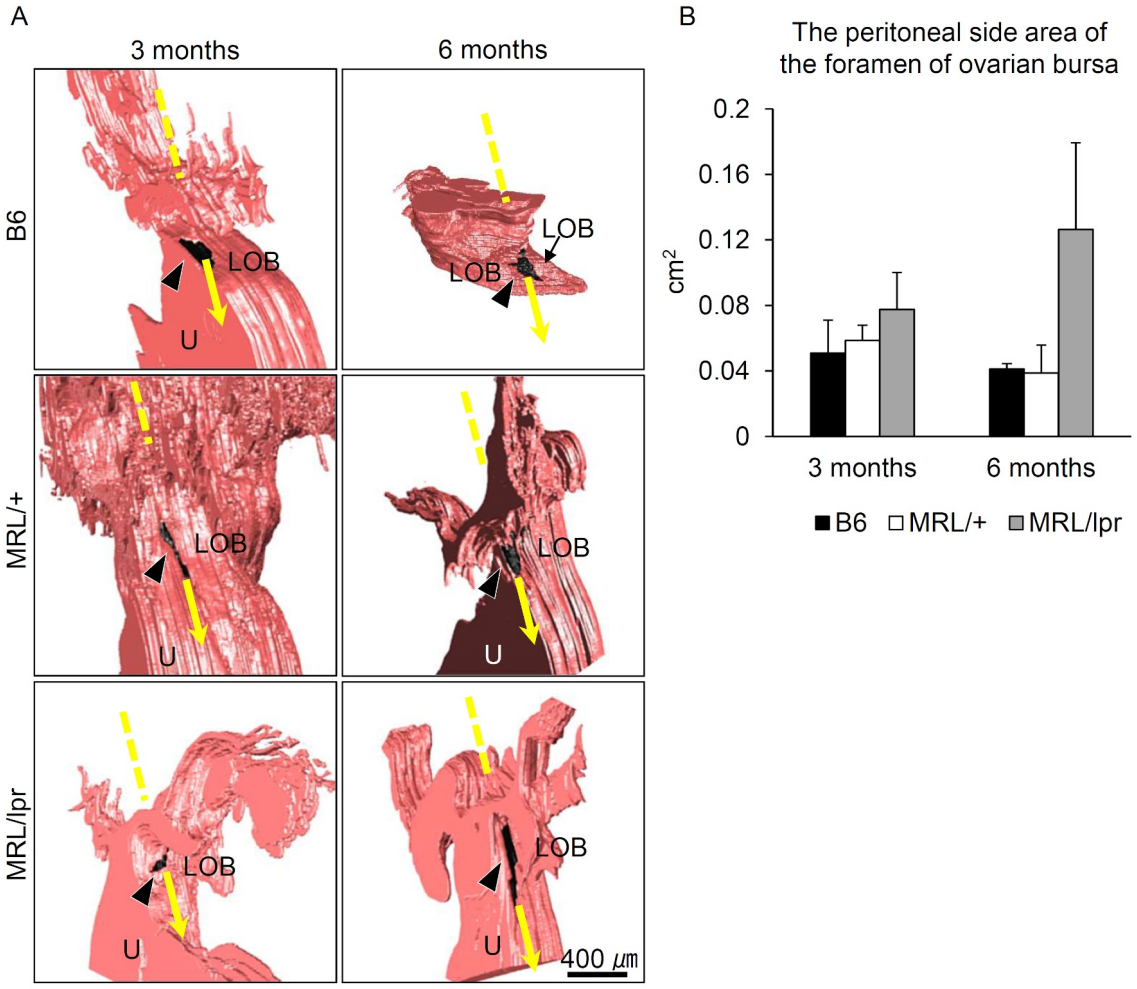

Figure 2-4. 3D reconstruction of the female reproductive tract and the size measurement of the foramen of ovarian bursa in mice.

(A) The mesothelium composing the female reproductive tract is colored in red. The foramen of ovarian bursa is colored in black and indicated by black arrowheads. The dashed yellow lines indicate the inside of the ovarian bursa, while the yellow arrows indicate the outside of the ovarian bursa. LOB: ligament of ovarian bursa, U: uterus.

(B) The peritoneal side area of the foramen of the ovarian bursa is measured. There is no significant strain-related difference in the same age examined by the Kruskal-Wallis test followed by Scheffé's method and no significant differences between 3 and 6 months of age in the same strain examined by the Mann-Whitney *U*-test. Data are the mean ± SE (n = 4 per group).

B6: C57BL/6N, MRL/+: MRL/MpJ, MRL/lpr: MRL/MpJ-Fas$^{lpr/lpr}$.

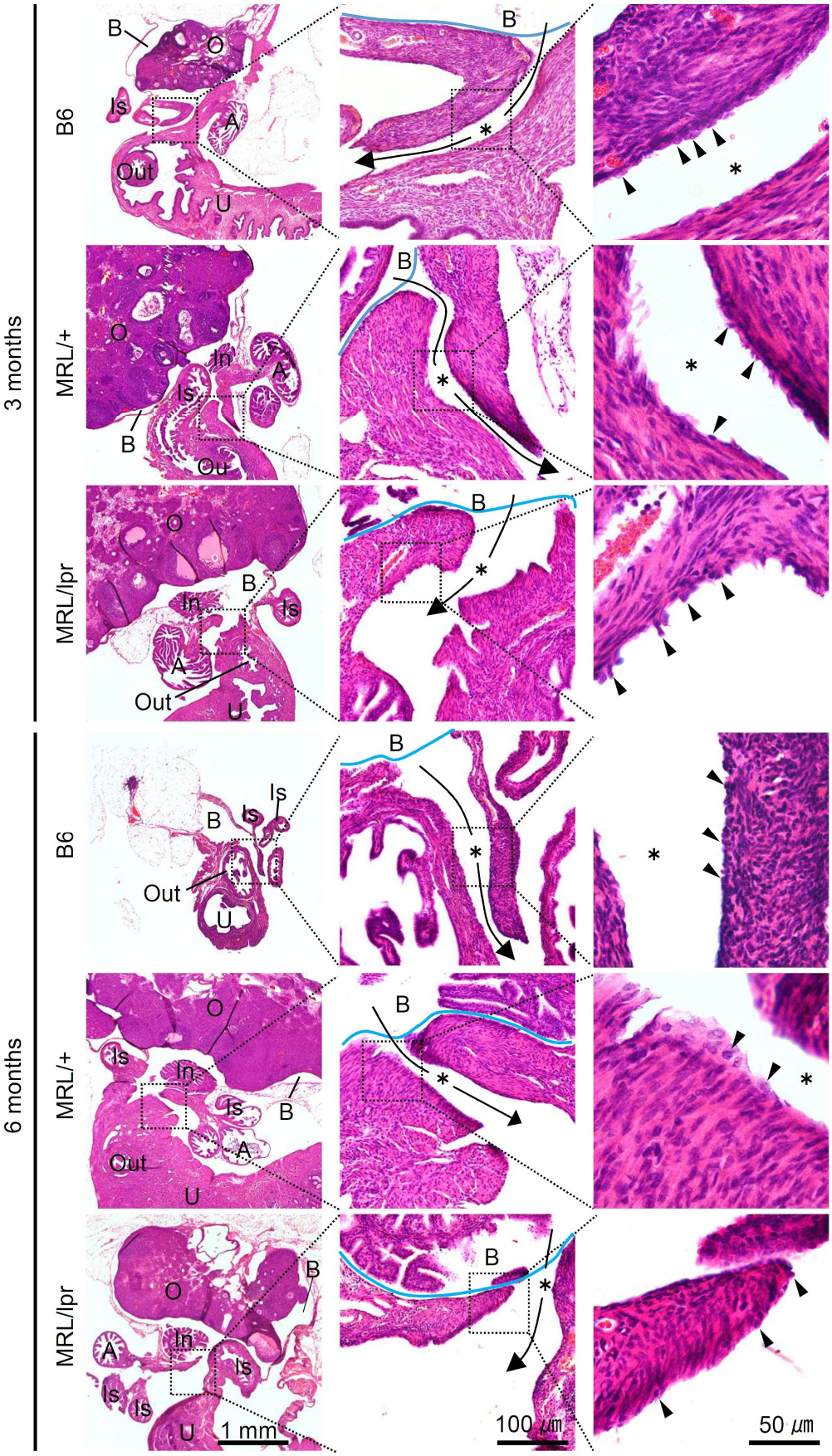
3 months
6 months
B6
MRL/+
MRL/lpr
B
O
Is
A
Out
U
In
Ou
1 mm
100 μm
50 μm

Figure 2-5. The histology of the foramen and ligament of ovarian bursa in mice.
The hematoxylin and eosin staining. The squares surrounded by black dashed lines are magnified in the images on the right side. The blue lines indicate the boundary of the ovarian bursa. Arrows connecting the intrabursal and peritoneal sides are passing through the foramen of the ovarian bursa, and the centers are indicated by asterisks. Arrowheads indicate the cuboidal mesothelial cells lining the epithelium of the foramen of ovarian bursa.
A: ampulla, B: ovarian bursa, In: infundibulum, Is: isthmus, O: ovary, Out: ostium uterinum tubae, U: uterus. B6: C57BL/6N, MRL/+: MRL/MpJ, MRL/lpr: MRL/MpJ-Fas$^{lpr/lpr}$.

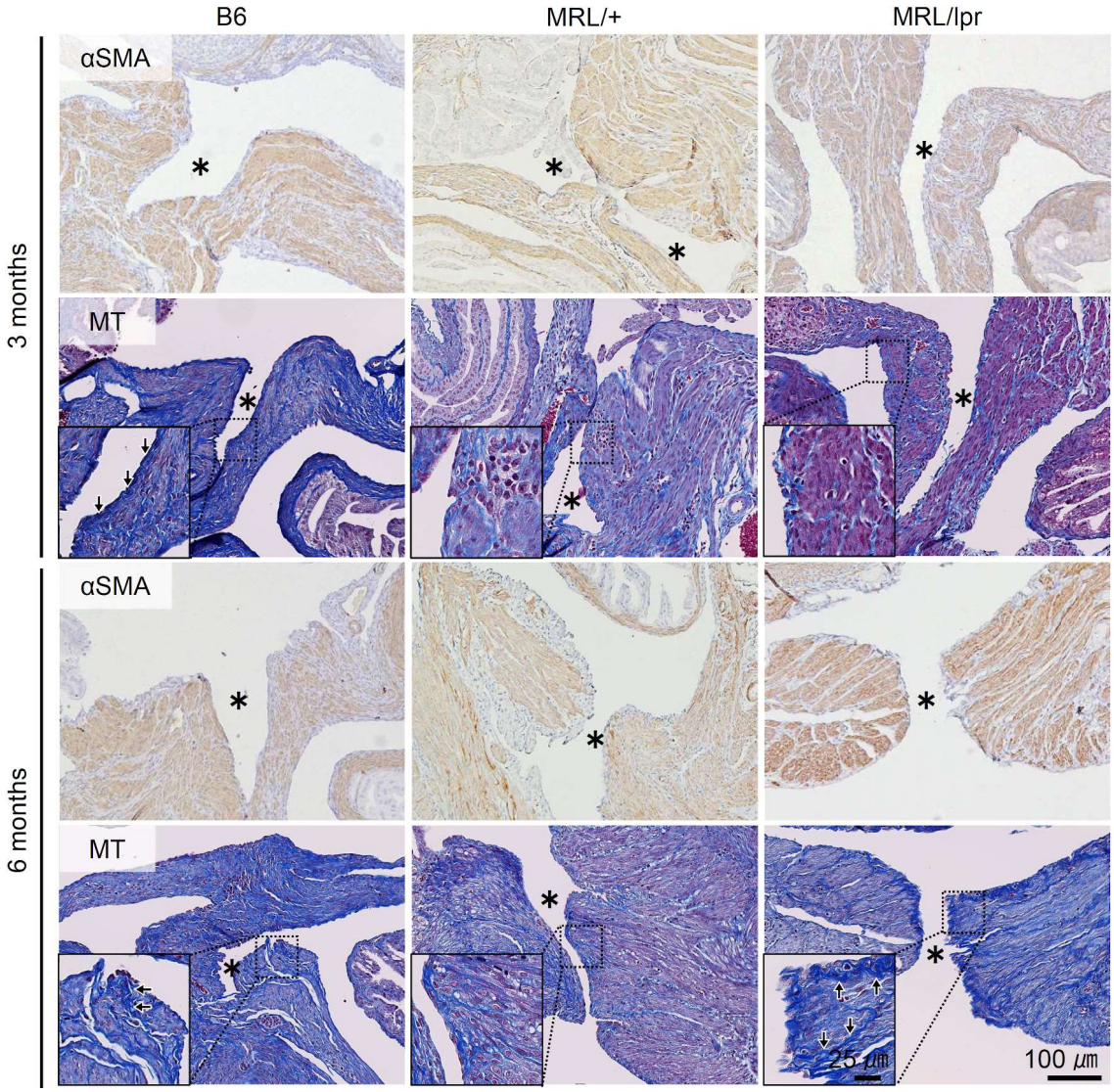

Figure 2-6. The distribution of smooth muscle cells and collagen fibers in the ligament of ovarian bursa in mice.

The squares surrounded by black dashed lines are magnified in the insets.

Asterisks: the foramen of ovarian bursa, Arrows: thick collagen fibers in the ligament of ovarian bursa, αSMA: alpha smooth muscle actin, immunohistochemistry, MT: masson's trichrome staining. B6: C57BL/6N, MRL/+: MRL/MpJ, MRL/lpr: MRL/MpJ-Fas$^{lpr/lpr}$.

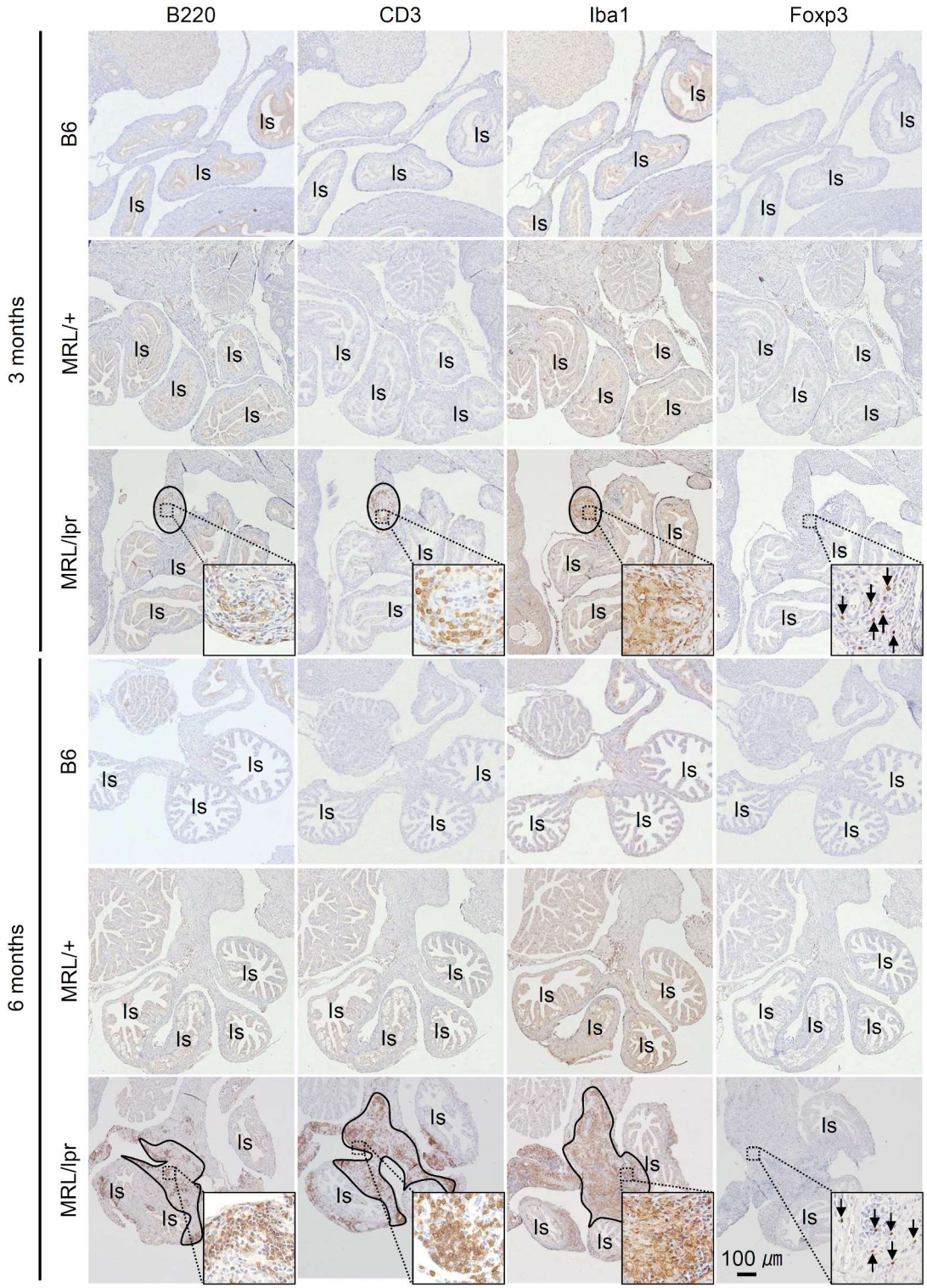

Figure 2-7. The immunohistochemistry of immune cells in the mesosalpinx suspending the oviductal isthmus in mice.

Black circles surround the area of severe infiltration of immune cells. The squares surrounded by the black dashed lines are magnified in the insets, showing the area of significant infiltration of the immune cells. Arrows indicate the distribution of the Foxp3 positive cells.

Is: isthmus. B6: C57BL/6N, MRL/+: MRL/MpJ, MRL/lpr: MRL/MpJ-Fas$^{lpr/lpr}$.

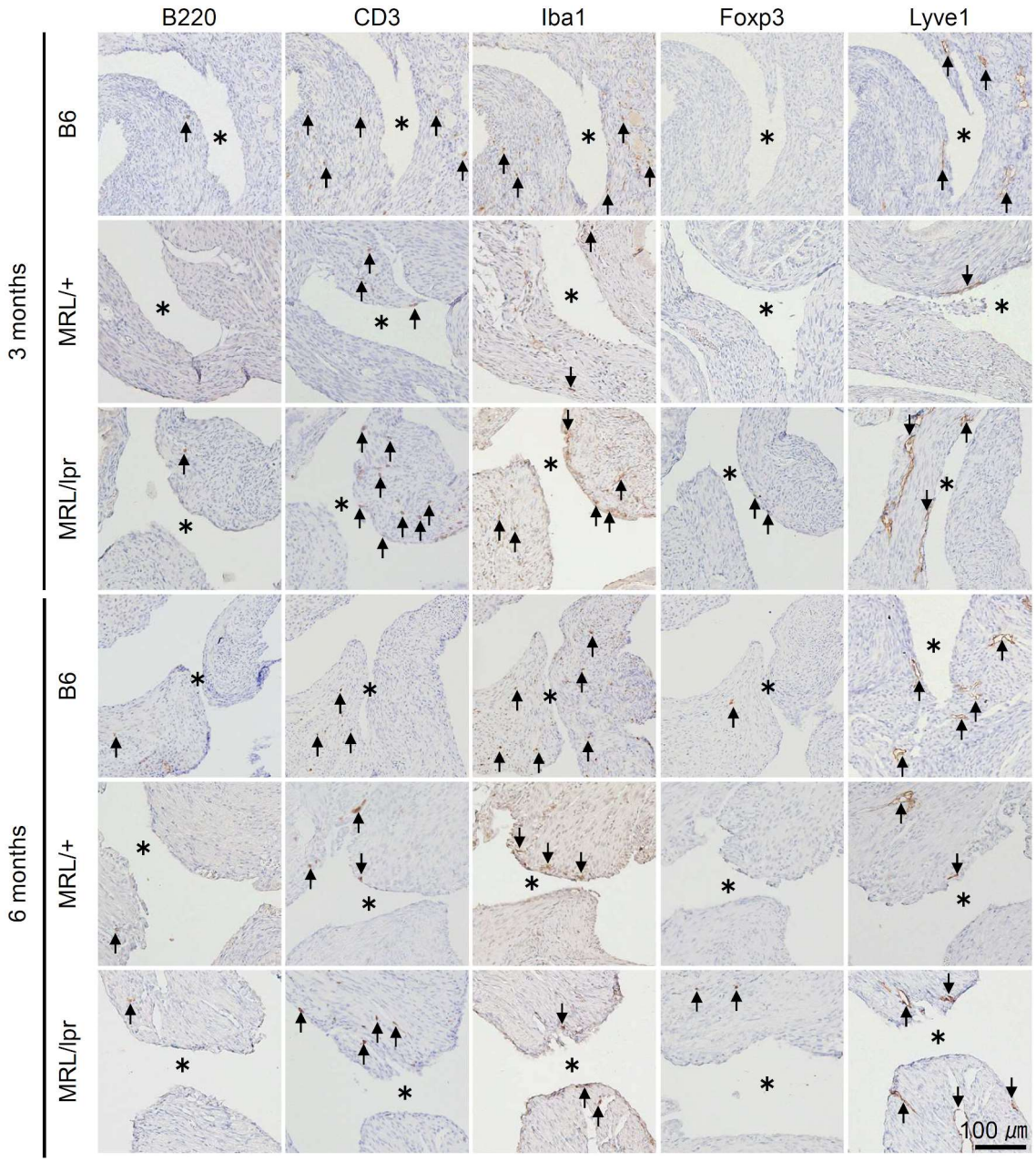

Figure 2-8. The immunohistochemistry of immune cells in the ligament of ovarian bursa in mice. Arrows indicate the distribution of immune cells in the connective tissue of the ligament of ovarian bursa.

Asterisks: the foramen of ovarian bursa. B6: C57BL/6N, MRL/+: MRL/MpJ, MRL/lpr: MRL/MpJ-Fas$^{lpr/lpr}$.

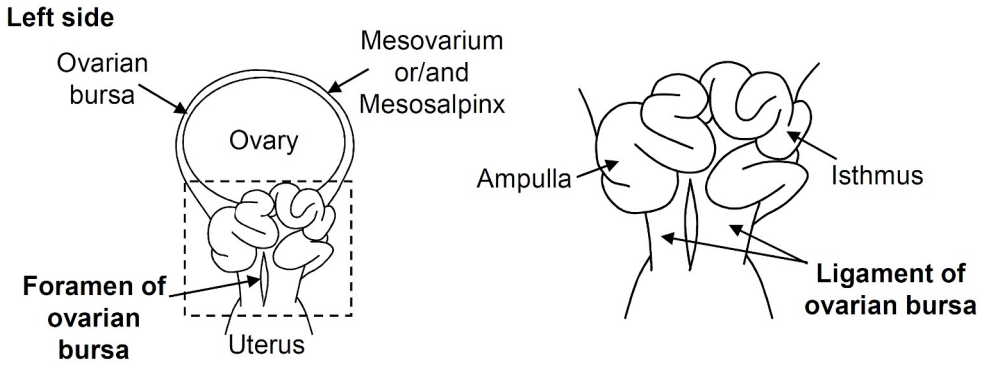

Figure 2-9. The anatomical schema of the foramen and ligament of ovarian bursa.
The mesovarium and mesosalpinx enclose the peritoneal cavity, which is called the ovarian bursa, and the large part of ovary. The mesosalpinx connecting the oviductal ampulla or isthmus and the cranial part of uterus has the silt-like opening of the ovarian bursa to the peritoneal cavity, which is called the foramen of ovarian bursa. The ligament of ovarian bursa, which is the part of the mesosalpinx connecting the oviduct and uterus, surrounds the foramen of ovarian bursa. The ligament consists of a thick smooth muscle layer. The squares surrounded by dashed lines are magnified in the schema on the right side.

Movie 2-1. Leakage of India ink from the ovarian bursa to extrabursa through the foramen of the ovarian bursa in C57BL/6N mouse at 3 months of age.

Chapter 3

The unique ovulation and luteinization phenotypes in MRL/+ mice after superovulation treatment

Introduction

In Chapter 1, MRL/+ mice subjected to hormonal superovulation were found to produce a markedly larger number of COCs than did B6 mice at 3 months of age. Furthermore, the number of COCs in the ampulla of oviducts exceeded the number of OOs in the ovaries of MRL/+ mice, as determined histologically by counting the total number of ruptured follicles, hemorrhagic bodies and the follicular antrum containing no oocytes. These results suggest that the PUR in MRL/+ mice was over 100%. Therefore, it is hypothesized that MRL/+ mice may have unique ovarian phenotypes including a high sensitivity to superovulation treatment and/or faster luteinization. Indeed, in support of the latter hypothesis, the sum of the histological number of ovulated oocytes and CL was comparable to the number of COCs in the ampulla of oviducts from MRL/+ mice.

Superovulation treatment is required not only for the experimental technology for the laboratory animals in the research field but also for assisted reproductive technology for the livestock animals possessing low ovulation rates, such as cows, horses, and sheep [112].The response to superovulation treatment varies among animal species and strains. The genetic parameters for sensitivity to superovulation treatment have been investigated for genetic improvement for bovine assisted reproductive technology [154]. In superovulated mice, the ovulation rates ranges from about 5 to 40 oocytes depending on the strains, which relates to genetics role in response to the hormonal treatment [12]. The mechanism underlying on the difference of sensitivity to superovulation treatment among mice strains could contribute to the improvement of the veterinary reproductive technology.

The MRL/+ mouse strain was established by selective interbreeding of the B6 (0.3%), C3H (12.1%), AKR (12.6%) and LG (75%) strains [45]. MRL/+ is well known as a strain that exhibits a unique tissue repair response to various injuries [45]. For example, in MRL/+ mice, ear punches approximately 2 mm in diameter [18] or heart injuries induced with a cryoprobe [70] repair without scarring or fibrosis. In addition, after Caesarean delivery, uterine wound healing in MRL/+ mice showed histological, mitotic and functional differences compared with the C57BL/6 strain [11]. In the kidney, an organ that does not regenerate, fibrotic activity was lower and calcification was increased after acute injury in MRL/+ than B6 mice [110].

Although MRL/+ mice have been used as healthy controls for MRL/lpr mice in pathological studies, they also show a propensity for autoimmune diseases [45]. The crucial contribution of the

telomeric region of chromosome 1 has been clarified in the pathogenesis of autoantibody production, splenomegaly and glomerulonephritis in MRL/+ mice [48]. It has been also identified several genetic loci associated with reproductive system phenotypes in this strain, such as the emergence of ovarian cysts [65], numerous ovarian mast cells [85], testicular oocytes [93] and spermatocyte apoptosis [64]. Thus, MRL/+ mice show unique phenotypes not only with regard to tissue repair and autoimmune disease capacity, but also in the reproductive system. Hence, in this Chapter, the author evaluated the ovulation, luteinization and fertilization rates of ovulated oocytes in MRL/+ mice not only to investigate the hypotheses raised in Chapter 1 but also to discuss the functional implications of the phenotypes found in the MRL/+ mice.

Materials and Methods

Animals

Animal experimentation was approved by the Institutional Animal Care and Use Committee of the Graduate School of Veterinary Medicine, Hokkaido University (Approval no. 13-0031). Experimental animals were handled in accordance with the Guide for the Care and Use of Laboratory Animals, Graduate School of Veterinary Medicine, Hokkaido University (approved by the Association for Assessment and Accreditation of Laboratory Animal Care International). Male B6, female B6 and female MRL/+ mice (3 months old) were obtained from Japan SLC, Inc.. The housing and euthanization of mice were performed as done in Chapters 1 and 2.

In vitro fertilization (IVF) for the fertilization rate assay

IVF was conducted according to the manuals supplied by the Center for Animal Resources and Development, Kumamoto University [118,119].

Collection of spermatozoa

Spermatozoa were obtained from the cauda epididymides of a male B6 mouse, resuspended in a dish containing 100 μL FERTIUP Mouse Sperm Preincubation Medium (KYUDO Co., Ltd., Saga, Japan), covered with paraffin oil and incubated for 1 h at 37°C with 5% CO_2 in air.

Collection of oocytes

For superovulation treatment, PMSG (ASKA Animal Health Co., Ltd.) was injected intraperitoneally into B6 (n = 5) and MRL/+ (n = 5) mice (200 μL of 37.5 IU/mL gonadotropin per mouse). Forty-eight hours after PMSG injection, mice were injected intraperitoneally with the same dose of hCG (ASKA Animal Health Co., Ltd.). Mice were killed 24 h after hCG injection. Intact COCs were released from the excised oviduct into 200 μL CARD MEDIUM (KYUDO Co., Ltd.), covered with paraffin oil and incubated for 30–60 min at 37°C with 5% CO_2 in air before insemination.

Insemination

After preincubation as described above, the sperm suspensions were added to a drop of

CARD MEDIUM containing COCs and incubated for 24 h at 37°C with 5% CO_2 in air. The final concentration of motile spermatozoa in the fertilization medium was 400–800 spermatozoa/μL.

The embryos obtained were counted and classified into four categories according to morphological features: fertilized embryos, unfertilized embryos, abnormal cleavage embryos and dead embryos. The number of embryos in each category was determined under a stereoscopic microscope. The fertilization rate was calculated as follows: Fertilization rate (%) = 100 × no. fertilized oocytes/(total no. fertilized and unfertilized oocytes)

Oocyte counts under a natural estrous cycle and after PMSG or hCG injection

The first group of female mice was mated with male mice in the evening. The next day, female mice (n = 5) with a vaginal plug were killed. The second group (n = 4) were injected intraperitoneally with PMSG (200 μL of 37.5 IU/mL gonadotropin per mouse) and killed 24 h after injection. The third group (n = 4) were injected with hCG (200 μL of 37.5 IU/mL gonadotropin per mouse) at estrus, which was determined by vaginal smear, and were killed 24 h after injection. COCs in the oviducts were extracted by oviductal perfusion with 0.01 M PBS and the number determined under a stereoscopic microscope.

Next-generation exome sequencing

Genomic DNA was isolated from the kidneys of B6 and MRL/+ mice with a DNeasy kit (Qiagen, Hulsterweg, The Netherlands). Exome capture was performed using Sureselect XT Mouse All Exon kit (Agilent Technologies Japan Ltd., Tokyo, Japan). Whole-exome sequencing was performed on a HiSeq2000 machine (Illumina, San Diego, CA, USA). The mouse mm10 assembly downloaded from the University of California Santa Cruz (UCSC; http://genome.ucsc.edu/, accessed 13 Aug 2018) was used as the reference genome for sequence alignment. Reads were mapped using Burrows–Wheeler Aligner version 0.5.9 (http://bio-bwa.sourceforge.net/, accessed 13 Aug 2018). Single nucleotide variants (SNVs) and small insertions/deletions were identified using SAMtools version 0.1.18 (http://samtools.sourceforge.net/, accessed 13 Aug 2018). The author hypothesized that mutations in genes associated with female hormones or their receptors may contribute to the high sensitivity of MRL/+ mice to hCG. Therefore, the author compared the exome sequences of the following

genes between the two strains: inhibin alpha (*Inha*), inhibin beta-B (*Inhbb*), follicle stimulating hormone beta (*Fshb*), activin A receptor, type 1 (*Acvr1*), activin receptor IIA (*Acvr2a*), activin receptor IIB (*Acvr2b*), luteinizing hormone beta (*Lhb*), inhibin beta-A (*Inhba*), gonadotropin releasing hormone 1 (*Gnrh1*), luteinizing hormone/choriogonadotropin receptor (*Lhcgr*), follicle stimulating hormone receptor (*Fshr*), estrogen receptor 1 (*Esr1*), estrogen receptor 2 (*Esr2*) and progesterone receptor (*Pgr*).

Histological analysis of luteinization in superovulated mice

Mice were either injected intraperitoneally with PMSG (200 μL of 37.5 IU/mL gonadotropin per mouse) followed 48 h later by hCG (200 μL of 37.5 IU/mL gonadotropin per mouse) or had their ovaries removed. The hCG injection time point 48 h after the administration of PMSG was considered as 12 h before ovulation (–12 h postovulation (h.p.o.); n = 4), with ovaries collected 72 h (12 h.p.o.; n = 6), 78 h (18 h.p.o.; n = 4) and 96 h (36 h.p.o.; n = 4) later (Figure 3-1). The ovaries were fixed with 4% PFA at 4°C overnight, embedded in paraffin and cut into 10-μm serial sections. Using serial HE-stained sections, the number of antral follicles, ruptured follicles, hemorrhagic bodies and CL was counted manually by histological observation, as described in Chapter 1.

The ratio of the maximum to minimum diameter of oocytes contained in antral follicles was defined as the 'oocyte aspect ratio' and calculated on serial sections of superovulated ovaries at –12 h.p.o. Serial sections clearly showing the nucleolus were selected for this analysis. Four serial sections of ovaries were used and 13–15 oocytes from B6 mice and 40–61 oocytes from MRL/+ mice were analyzed in each ovary to determine the oocyte aspect ratio.

Reverse transcription and quantitative real-time polymerase chain reaction

Total RNA from ovaries of B6 and MRL/+ mice at 12 h.p.o. (n = 4) and 27 h.p.o. (n = 4) was purified using TRIzol reagent (Thermo Fisher Scientific Inc., Waltham, MA, USA) according to the manufacturer's instructions. The purified total RNA (83.3 ng/μL) was used as a template to synthesise cDNA using ReverTra Ace qPCR RT Master Mix (TOYOBO Co., Ltd., Osaka, Japan). Quantitative polymerase chain reaction (qPCR) analysis was performed on the cDNA (20 ng/μL) using THUNDERBIRD SYBR qPCR Mix (TOYOBO Co., Ltd) and the following gene-specific primers (5′–3′): matrix metallopeptidase 2 (*Mmp2*), ACGATGATGACCGGAAGTG (forward)

and AATCGGAAGTTCTTGGTGTAGG (reverse; product size 157 bp); matrix metallopeptidase 9 (*Mmp9*), CATTCGCGTGGATAAGGAG (forward) and GAAACTCACACGCCAGAAGA (reverse; product size 112 bp); tissue inhibitor of metalloproteinase 1 (*Timp1*), TCTGGCATCCTCTTGTTGCT (forward) and ACTCTTCACTGCGGTTCTGG (reverse; product size 292 bp); and actin, beta (*Actb*; used as a housekeeping gene), TGTTACCAACTGGGACGACA (forward) and GGGGTGTTGAAGGTCTCAAA (reverse). The qPCR cycling conditions were 95°C for 1 min, followed by 40 cycles of 95°C for 15 s and 60°C for 45 s. Primers were obtained from Sigma-Aldrich Co. Llc. (St. Louis, MO, USA). The concentration of the template RNA used in the reverse transcription reaction was 83.3 ng/μL, whereas the concentration of cDNA used in the PCR reaction was 20.0 ng/μL. Data were normalized against the expression level of *Actb* and analyzed using the $\Delta\Delta C_t$ method.

Statistical analysis

Results are expressed as the mean ± SE. Statistical analysis was performed as done in Chapters 1 and 2.

Results

Morphological features of embryos obtained after IVF

After IVF of oocytes obtained from B6 and MRL/+ mice, different categories of embryos (i.e. fertilized, unfertilized, abnormal and dead) were observed, as shown in Figure 3-2A-G. There were many dead embryos, characterized by oocyte deformation and cytolysis, were numerous in the MRL/+ group (Figure 3-2G), but these were not observed in the B6 group.

Histological ovary sections were obtained from mice at –12 h.p.o., a time point when antral follicles are considered to be maturing for ovulation. In the antral follicles of MRL/+ mice, elongated or compacted oocytes were frequently observed, whereas regular round-shaped oocytes were found in the antral follicles of the B6 mice (Figure 3-2H and I). As shown in Figure 3-2J the oocyte aspect ratio was significantly higher in MRL/+ than B6 mice (1.40 ± 0.04 vs 1.20 ± 0.02 respectively), indicating an altered oocyte morphology in the antral follicles of MRL/+ mice.

Number of embryos obtained after IVF and the fertilization rate in MRL/+ than B6 mice

After superovulation treatment, MRL/+ mice produced 71.0 ± 13.4 COCs, whereas B6 mice produced 26.8 ± 2.8 COCs (Figure 3-3A). In B6 mice, the number of fertilized, unfertilized, abnormal and dead embryos was 12.8 ± 1.6 (47.7 ± 2.5% of the total collected embryos), 1.2 ± 0.4 (4.9 ± 1.5%), 12.8 ± 1.6 (47.4 ± 2.0%) and 0 (0%) respectively. In MRL/+ mice, these number of fertilized, unfertilized, abnormal and dead embryos was 11.6 ± 4.6 (16.6 ± 4.4%), 9.2 ± 2.2 (14.7 ± 5.1%), 17.2 ± 3.2 (24.7 ± 2.3%) and 33.0 ± 9.2 (43.9 ± 7.1%), respectively. The number of unfertilized and dead embryos was significantly larger in MRL/+ than B6 mice. Furthermore, the fertilization rate was significantly lower in MRL/+ than B6 mice (52.3 ± 11.9% vs 90.7 ± 2.8% respectively; Figure 3-3B).

Number of COCs obtained under a natural oestrus cycle or after PMSG treatment

Under a natural estrous cycle without superovulation treatment, B6 and MRL/+ mice ovulated 10.3 ± 0.5 and 12.0 ± 0.9 COCs respectively, with no significant difference between the two strains (Figure 3-4A). Because in non-equine species PMSG stimulates not only follicular development, but also ovulation [19], the author also counted the number of ovulated COCs following injection of PMSG. After a single PMSG injection, B6 and MRL/+ mice ovulated 9.5 ± 2.7 and 9.5 ± 2.5 COCs respectively, which did not differ significantly (Figure 3-4B). In contrast,

the number of ovulated COCs after hCG treatment was significantly higher in MRL/+ than B6 mice (16.8 ± 4.2 vs 2.5 ± 2.5 respectively; Figure 3-4C).

Comparative sequence analysis of ovulation-related genes in B6 and MRL/+ mice

The author hypothesized that mutations in genes associated with female hormones or their receptors may contribute to the high sensitivity of MRL/+ mice to hCG. Therefore, the author compared the exome sequences of *Inha*, *Inhbb*, *Fshb*, *Acvr1*, *Acvr2a*, *Acvr2b*, *Lhb*, *Inhba*, *Gnrh1*, *Lhcgr*, *Fshr*, *Esr1*, *Esr2* and *Pgr* genes between the two strains (Table 3-1) Genetic variants were detected in the following genes in MRL/+ mice: *Acvr1* (one synonymous exon variant and six intron variants), *Acvr2b* (seven synonymous exon and 15 intron variants), *Gnrh1* (one intron variant and one variant in the 3′ untranslated region (UTR)), *Lhcgr* (one synonymous exon, 12 intron and two upstream region variants) and *Esr1* (two synonymous exon variants and 12 intron variants). In addition to nine intron variants and five synonymous exon variants, *Pgr* in MRL/+ mice had two non-synonymous exon variants. The first one exon variant was a missense variant in position 118 in the DNA sequence (TCG) causing the serine to be replaced with a threonine, yielding ACG in the DNA sequence (variant ID: rs16808507). The second exon variant in *Pgr* was also a missense variant, in position 252 in the DNA sequence (GGA), causing the glycine to be replaced with a glutamic acid, yielding GAA (variant ID: rs16808511). Representatively, mice of the AKR/J and NZB/BINJ strains also have these two non-synonymous variants in *Pgr* (Mouse Phenome Database; https://phenome.jax.org/, data accessed 13 Apr 2018). The number of embryos produced from the AKR/J and NZB/BINJ strains after superovulation treatment has been reported to be approximately 20 and 10 respectively [116,147], indicating that it is unlikely that these variants cause the ovulation of high number of embryos in mice.

No variants were detected in the *Inha*, *Inhbb*, *Acvr2a*, *Fshb*, *Lhb*, *Inhba*, *Fshr* and *Esr2* genes. Thus, no coding region mutations affecting protein structure were identified in the genes examined.

Folliculogenesis and luteinization after superovulation treatment

The author examined ovarian histology after superovulation (Figure 3-5A-J). At –12 h.p.o., just before ovulation, numerous antral follicles were observed and CL occupied the remaining space of the ovaries in both B6 and MRL/+ mice (Figure 3-5A and F). At 12 h.p.o., ruptured

follicles and hemorrhagic bodies were detected, and several antral follicles and CL were observed in both strains (Figure 3-5B and G). At 18 and 36 h.p.o., some hemorrhagic bodies remained, and several CL were observed in the ovaries of B6 mice (Figure 3-5C and D). In contrast, in MRL/+ mice, the number of CL in the ovaries increased at 18 h.p.o. (Figure 3-5H) compared with 12 h.p.o. (Figure 3-5G). At 36 h.p.o., numerous CL occupied almost the whole ovary in MRL/+ mice (Figure 3-5I). The CL in both strains consisted of fibroblasts, vascular endothelial cells and granulosa and theca lutein cells containing vacuoles (Figure 3-5E and J).

Next, the author counted the number of antral follicles, ruptured follicles, hemorrhagic bodies and CL after superovulation in B6 and MRL/+ mice (Figure 3-6A and B). In B6 mice, the number of antral follicles was significantly greater at –12 than at 12, 18 and 36 h.p.o. (15 ± 1 vs 5.1 ± 0.9, 5.0 ± 0.9 and 1.8 ± 0.8 respectively; $P < 0.05$). The number of ruptured follicles was significantly greater at 12 h.p.o. (10.0 ± 1.7) than at other time points (0.3 ± 0.3, 0.8 ± 0.5 and 0.3 ± 0.3 at –12, 18 and 36 h.p.o. respectively; $P < 0.05$) and the number of hemorrhagic bodies were significantly greater at 18 and 36 h.p.o. (14.0 ± 2.7 and 9.0 ± 1.5 respectively) than at –12 and 12 h.p.o. (0.3 ± 0.3 and 0.7 ± 0.4 respectively). However, the number of CL did not change significantly throughout the observation period (8.5 ± 1.6, 13.4 ± 1.8, 10.8 ± 2.9 and 9.5 ± 2.3 at –12, 12, 18 and 36 h.p.o. respectively).

Similar to B6 mice, the number of antral follicles in the MRL/+ strain was significantly greater at –12 h.p.o. (66.0 ± 4.9) than at other time points, and significantly greater at 12 and 18 than at 36 h.p.o. (22.0 ± 2.3 and 26.5 ± 1.9 vs 4.5 ± 2.5 respectively; $P < 0.05$). The number of ruptured follicles was significantly greater at 12 h.p.o. (21.0 ± 0.9) than at other time points, and significantly greater at 18 than at –12 and 36 h.p.o. (9.5 ± 1.8 vs 0 ± 0 and 0 ± 0 respectively; $P < 0.05$). However, unlike B6 mice, in MRL/+ mice there number of CL was significantly greater at 36 than at 12 h.p.o. (37.3 ± 6.1 vs 16.7 ± 1.2 respectively; $P < 0.05$).

The percentage of antral follicles, ruptured follicles, hemorrhagic bodies and CL relative to the total number of observed structures is shown in Figure 3-6C and D. At –12 h.p.o., percentages were similar in the MRL/+ and B6 groups. At 12 h.p.o., the ovaries of MRL/+ mice had a significantly higher percentage of hemorrhagic bodies and a lower percentage of CL than in B6 mice. At 18 h.p.o., the percentage of antral follicles and ruptured follicles was significantly higher, whereas the percentage of hemorrhagic bodies was lower in ovaries of MRL/+ than B6 mice. Importantly, at 36 h.p.o., the percentage of hemorrhagic bodies was significantly lower and the

percentage of CL was significantly higher in MRL/+ than B6 mice ($P < 0.05$). These data indicate differences in ovarian phenotypes between B6 and MRL/+ mice; in particular, there is an accelerated luteinization in the latter strain.

Expression of MMPs and TIMPs in ovaries during luteinization

MMPs and TIMPs play a key role in the breakdown of ECM for luteinization [117,139]. Among the MMP family of proteins, Mmp2 and Mmp9 appear to be important for luteinization [117]. Our findings (Figure 3-6D) suggest that ovaries of MRL/+ mice are forming CL most actively between 18 and 36 h.p.o. Therefore, the author examined the expression of *Mmp2*, *Mmp9* and *Timp1* in ovaries of B6 and MRL/+ mice at 12 h.p.o. (before luteinization) and at 27 h.p.o. (during luteinization; Figure 3-7). The expression of *Mmp2* and *Mmp9* did not change in either strain between 12 and 27 h.p.o., whereas *Timp1* expression was significantly lower at 27 than at 12 h.p.o. in MRL/+ mice (Figure 3-7A). *Mmp9* expression at 12 h.p.o. was significantly lower in MRL/+ than B6 mice ($P < 0.05$). The ratio of *Mmp2* and *Mmp9* expression relative to that of *Timp1* increased significantly at 27 h.p.o. compared with 12 h.p.o. in MRL/+ mice (Figure 3-7B).

In addition, the author compared the exome sequences of *Mmp2*, *Mmp9* and *Timp1* (Table 3-2). No variants were detected in *Timp1*. *Mmp2* in MRL/+ mice had 18 synonymous exon variants, 47 intron variants and one variant in the 5′UTR. *Mmp9* in MRL/+ mice had one non-synonymous exon variant, which was a missense variant in position 639 in the DNA sequence (CTC) in which leucine was replaced with proline, yielding CCC in the DNA sequence (variant ID: rs13475086). AKR/J and BALB/cJ mice also harbor this non-synonymous variant in *Mmp9* (Mouse Phenome Database; https://phenome.jax.org/, data accessed 13 Apr 2018). These strains of mice exhibit slower healing than MRL/+ mice [73], indicating that it is unlikely that this variant causes the faster luteinization related to the faster healing in MRL/+ mice.

Discussion

Consistent with the results in Chapter 1 and other reports [147], MRL/+ mice ovulated significantly more COCs than did B6 mice after superovulation treatment. MRL/+ mice generated approximately 70 oocytes after the injection of PMSG and hCG, and approximately 10 oocytes in the normal estrous cycle. These results indicate that the MRL/+ strain has a higher sensitivity to these gonadotrophin treatments than does the B6 strain. In equines, PMSG is known as the equine chorionic gonadotrophin and shows only LH-like activity [19]. However, in non-equine species, PMSG shows both FSH and LH activity, and thus stimulates not only folliculogenesis, but also ovulation and luteinization [19]. A previous study discussed the possibility that produced oocytes induced by PMSG treatment remained in the oviducts until subsequent ovulation following injection of hCG [147]. However, in the present study the number of produced COCs following PMSG treatment was almost equal between the MRL/+ and B6 strains, and comparable to that of COCs under the natural estrous cycle. This is consistent with the findings of another study that compared the number of produced oocytes after PMSG injection with that ovulated in normal estrous [58]. Interestingly, MRL/+ mice produced more COCs than did B6 mice after a single injection of hCG. However, the total number of COCs produced following injection of either PMSG or hCG alone did not reach the number generated after sequential injections of PMSG and hCG. Therefore, both hCG and sequential injections of PMSG and hCG have stronger effects on ovulation in MRL/+ than B6 mice. Based on these findings, the author hypothesized that mutations in genes associated with female hormones and their receptors contributed to the high sensitivity to hCG observed in the MRL/+ strain. However, comparison of the exon sequences of several such genes (*Inha*, *Inhbb*, *Fshb*, *Acvr1*, *Acvr2a*, *Acvr2b*, *Lhb*, *Inhba*, *Gnrh*, *Lhcgr* and *Fshr*) between the B6 and MRL/+ strains found no coding region variants predicted to affect protein structure and function. Therefore, the superovulation-related phenotype in MRL/+ mice may be related to an altered expression of these genes in the ovary and/or in other organs associated with the hypothalamic–pituitary–gonadal axis, which could arise due to genetic variation in sequences outside of coding regions, such as in gene promoters.

Approximately 44% of embryos developed from oocytes produced in MRL/+ mice were dead, and the fertilization rate was significantly lower for the MRL/+ than B6 strain. These results indicate the low quality of produced oocytes in MRL/+ mice. Various factors, such as genes, hormone levels, chemical interactions and environment and physical conditions, affect oocyte

quality [14,80,101,113]. Importantly, previous studies reported that the percentage of cells undergoing apoptosis in cumulus cells increased in oocytes within follicles subjected to hydrostatic pressure [99]. The histological observations revealed a more elongated oocyte morphology in MRL/+ than B6 mice. It is not clear whether this morphological change is due to factors intrinsic to oocytes or whether it is influenced by the microenvironment, such as by pressure from the large number of developing follicles in MRL/+ mice. Because ovaries in MRL/+ mice contain a larger number of follicles than ovaries in B6 mice, it is possible that the poorer oocyte quality in MRL/+ mice results from exposure to high pressure. The morphological abnormality was not found in embryos *in vitro*. Furthermore, the IVF rate of human ovoid embryos is not affected, but delayed preimplantation development is seen [32]. There are no reports regarding how an ovoid shape of oocytes in ovarian sections can affect the fertilization rate and oocyte quality. However, the data suggest the possibility that an excessive number of follicles in an ovary can affect the oocyte quality in multifetal animals such as mice.

The folliculogenesis pattern was similar in MRL/+ and B6 mice before ovulation and the injection of hCG, with antral follicles accounting for most follicles in the ovary. After ovulation, MRL/+ mice formed CL within 36 h, whereas hemorrhagic bodies were numerous in B6 mice even after 36 h. These results indicate that the differentiation of ovulated follicles to CL occurs faster in MRL/+ than B6 mice. In addition, the higher percentage of ruptured follicles at 18 h.p.o. in MRL/+ than B6 mice indicates that ovulation from matured follicles continues for a longer period in MRL/+ than B6 mice, which may be due to the high sensitivity of the former strain to artificial ovulation.

In Chapter 1, the author considered that the accelerated luteinization in MRL/+ mice would be associated with the enhanced healing ability in this strain. Several possible explanations for the enhanced healing capacity of MRL/+ mice have been proposed, including cell cycle and proliferative features, increased stem cell quantity and/or quality and enhanced immune response [45]. In particular, changes in the ECM regulated by MMPs appeared to be crucial for the healing capacity of the MRL/+ strain [45]. ECM remodeling is cooperatively and tightly regulated by interactions between proteases and their inhibitors, such as MMPs and TIMPs respectively [139]. For example, it was proposed that neutrophils and macrophages within wounds secrete significantly higher amounts of active MMP-2 and MMP-9 and lower amounts of TIMPs in MRL/+ than B6 mice [38,45]. Importantly, in the CL, a transient endocrine gland, marked

morphological changes are found upon the differentiation of luteal cells, and this process also involves changes in the ECM that enable cell migration and neovascularization in the newly formed CL [25,117]. Within the MMP family of proteins, MMP-2 and MMP-9 appear to be important for luteinization [117]. The ratio of active MMPs to TIMPs may be important in maintaining an ECM microenvironment conducive to the differentiation of follicle-derived cells into luteal cells [114]. The present results showed that the ratio of *Mmp2* and *Mmp9* to *Timp1* was elevated earlier in MRL/+ than B6 mice, resulting in the MMP–TIMP balance shifting towards MMP shortly after ovulation in MRL/+ mice. This suggests that accelerated ECM remodelling, as observed in wound healing, also occurs in the ovulated and ruptured follicles in MRL/+ mice, leading to quick luteinization. In addition, oocyte development during nest breakdown and folliculogenesis is accelerated in neonatal MRL/+ mice [143], and this strain has a high frequency of ovarian cysts at older ages [65,69]. Together, these results indicate that the MRL/+ mice have unique phenotypes associated with the female reproductive system throughout life.

In conclusion, the matured MRL/+ strain has unique phenotypes in female reproductive function, such as high sensitivity to gonadotrophin treatment and a faster process of luteinization; these characteristics can contribute to the study of the mechanism of follicle remodeling and female reproductive function. In addition, it is suggested that the reproductive research on murine female reproductive morphofunction should consider the strain-depending differences on the phenotypes of ovulation and luteinization. Further studies on genetic mechanism underlying the unique reproductive phenotype of MRL/+ strains would contribute to improvement of the assisted reproductive technology in livestock animals.

Summary

In this Chapter, the author reports two unique phenotypes in the female reproductive system of MRL/+ mice that affect ovulation and luteinization as suggested in Chapter 1. The author found that superovulation treatment resulted in the production of significantly more oocytes in MRL/+ than B6 mice (71.0 ± 13.4 vs 26.8 ± 2.8 respectively). However, no exon mutations were detected in genes coding for female reproductive hormones or their receptors in MRL/+ mice. In addition, the fertilization rate was lower for ovulated oocytes from MRL/+ than B6 mice, with most of the fertilized oocytes showing abnormal morphology, characterized by deformation and cytolysis. Histological tracing of luteinization showed that MRL/+ mice formed corpora lutea within 36 h after ovulation, whereas B6 mice were still at the hemorrhagic bodies formation stage after 36 h. The balance between the expression of matrix metalloproteinases and their tissue inhibitors shifted towards the former earlier after ovulation in MRL/+ than B6 mice. This result indicates a possible link between accelerated extracellular matrix remodeling in the ovulated or ruptured follicles and luteinization in MRL/+ mice. Together, MRL/+ mice exhibit distinct phenotypes in several biological processes including reproduction. These findings reveal novel reproductive phenotypes in MRL/+ mice that provide novel insights into reproductive biology.

Tables and Figures

Table 3-1. Polymorphisms in ovulation-related genes detected between C57BL/6N (B6) and MRL/MpJ (MRL/+) strains using next-generation sequencing

Gene	Chr	Location (bp)		Strains		Region	Change	Variant ID
	no.	Start	End	B6	MRL/+			
Acvr1	chr02	58448495	58448495	A	G	Intron	–	rs214065797
		58458835	58458835	G	T	Intron	–	rs230650639
		58458868	58458868	T	C	Intron	–	rs246215171
		58463020	58463020	T	C	Exon	Synonymous SNV	rs33549343
		58463229	58463229	G	A	Intron	–	rs228629097
		58477571	58477571	A	G	Intron	–	rs27909412
		58500669	58500669	C	A	Intron	–	rs261538744
Acvr2b	chr09	119427385	119427385	A	G	Intron	–	rs45872254
		119427427	119427431	TGCTC	–	Intron	–	-
		119427489	119427489	C	T	Exon	Synonymous SNV	rs254093865
		119427495	119427495	C	T	Exon	Synonymous SNV	rs245957907
		119427867	119427867	A	C	Intron	–	rs50502574
		119427874	119427874	A	G	Intron	–	rs214816821
		119427922	119427922	T	G	Intron	–	rs238044625
		119427962	119427962	C	T	Intron	–	rs48995394
		119428382	119428382	A	G	Exon	Synonymous SNV	rs220947222
		119428430	119428430	G	C	Exon	Synonymous SNV	rs236256586
		119428520	119428520	A	G	Exon	Synonymous SNV	rs30372811
		119428612	119428612	C	G	Intron	–	rs30134774

Gene	Chr no.	Location (bp) Start	End	Strains B6	MRL/+	Region	Change	Variant ID
		119428620	119428620	G	–	Intron	–	-
		119429791	119429791	–	A	Intron	–	-
		119429811	119429811	G	A	Intron	–	rs249216178
		119429889	119429889	C	A	Exon	Synonymous SNV	rs50269096
		119429928	119429928	T	C	Exon	Synonymous SNV	rs231454902
		119430037	119430037	G	A	Intron	–	rs215251161
		119430059	119430059	A	G	Intron	–	rs50218863
		119430115	119430115	–	ATAGTCAGAAT CGCCACGCC	Intron	–	-
		119430387	119430387	T	C	Intron	–	rs247262863
		119432888	119432888	A	–	Intron	–	-
Gnrh1	chr14	67746552	67746552	A	T	Intron	–	rs3023411
		67749359	67749359	A	–	3′UTR	–	-
Lhcgr	chr17	88765044	88765044	G	A	Exon	Synonymous SNV	rs45832892
		88765274	88765274	G	A	Intron	–	rs49175256
		88765283	88765283	T	C	Intron	–	rs49233045
		88765284	88765284	G	C	Intron	–	rs50445833
		88765297	88765297	A	G	Intron	–	rs50723996
		88765328	88765328	A	G	Intron	–	rs51548994
		88767223	88767223	–	C	Intron	–	-
		88767357	88767357	G	C	Intron	–	rs33145242

Gene	Chr no.	Location (bp) Start	End	Strains B6	MRL/+	Region	Change	Variant ID
		88767384	88767384	A	C	Intron	–	rs33347120
		88769697	88769697	T	G	Intron	–	rs3717394
		88769748	88769748	T	A	Intron	–	rs3717517
		88769935	88769937	AAC	–	Intron	–	rs235138678
		88772141	88772141	G	A	Intron	–	rs52183165
		88792035	88792035	C	T	Upstream	–	rs52233715
		88792040	88792040	G	A	Upstream	–	rs52545123
Pgr	chr09	8900819	8900819	T	A	Exon	Non-synonymous SNV	rs16808507
		8900914	8900914	A	T	Exon	Synonymous SNV	rs222662569
		8900959	8900959	G	A	Exon	Synonymous SNV	rs246932498
		8901222	8901222	G	A	Exon	Non-synonymous SNV	rs16808511
		8901259	8901259	C	A	Exon	Synonymous SNV	rs16808515
		8901730	8901730	C	G	Exon	Synonymous SNV	rs16808520
		8922762	8922762	C	T	Intron	–	rs16808540
		8956132	8956132	–	TGT	Intron	–	–
		8956215	8956215	T	A	Intron	–	rs16808632
		8956228	8956228	T	–	Intron	–	rs16808634
		8956263	8956263	T	C	Exon	Synonymous SNV	rs16808635
		8956426	8956426	A	G	Intron	–	rs38678743
		8956474	8956474	G	A	Intron	–	rs253462664
		8956484	8956484	T	C	Intron	–	rs262156449

Gene	Chr	Location (bp)		Strains		Region	Change	Variant ID
	no.	Start	End	B6	MRL/+			
		8956517	8956517	A	C	Intron	–	rs216472569
		8956530	8956530	C	A	Intron	–	rs234992683
Esr1	chr10	4964668	4964668	G	A	Intron	–	rs29383782
		4964798	4964798	C	T	Intron	–	rs50779278
		4964883	4964883	T	G	Intron	–	rs49862291
		4964886	4964886	C	T	Intron	–	rs46991755
		4966154	4966154	G	T	Intron	–	rs29315913
		4966407	4966407	T	C	Intron	–	rs29330062
		4969082	4969082	A	G	Intron	–	rs16821149
		4969093	4969093	G	A	Intron	–	rs16821150
		4969094	4969094	T	A	Intron	–	rs16821151
		4969106	4969116	TGTCTTCGAGA	–	Intron	–	rs214903150
		4969210	4969210	G	T	Exon	Synonymous SNV	rs16821161
		4969249	4969249	A	T	Exon	Synonymous SNV	rs47715549
		4969307	4969307	C	T	Intron	–	rs46716572
		4969389	4969389	C	T	Intron	–	rs47973744

chr, chromosome; SNV, single nucleotide variant; *Acvr1*, activin A receptor, type 1; *Acvr2b*, activin receptor IIB; *Gnrh1*, gonadotropin releasing hormone 1; *Lhcgr*, luteinizing hormone/choriogonadotropin receptor; *Pgr*, progesterone receptor; *Esr1*, estrogen receptor 1; UTR, untranslated region.

Table 3-2. Polymorphisms in luteinization-related genes detected between the C57BL/6N (B6) and MRL/MpJ (MRL/+) strains using next-generation sequencing

Gene	Chr	Location (bp)		Strains		Region	Change	Variant ID
	no.	Start	End	B6	MRL/+			
Mmp2	chr08	92827509	92827509	C	G	5′UTR	–	rs50154992
		92827789	92827789	T	C	Intron	–	rs47915014
		92830595	92830595	A	G	Intron	–	rs50707366
		92830606	92830606	T	A	Intron	–	rs47202868
		92830632	92830632	C	T	Exon	Synonymous SNV	rs48669156
		92831599	92831602	GCAC	–	Intron	–	–
		92831611	92831611	G	A	Intron	–	rs52544499
		92831862	92831862	T	C	Intron	–	rs47205486
		92832757	92832757	A	G	Intron	–	rs45755812
		92832783	92832783	A	G	Exon	Synonymous SNV	rs47346055
		92832906	92832906	C	T	Intron	–	rs47940001
		92832935	92832935	T	C	Intron	–	rs46642227
		92832937	92832937	T	C	Intron	–	rs50670061
		92832983	92832983	T	C	Intron	–	rs51535272
		92833019	92833019	C	T	Intron	–	rs46335818
		92833037	92833037	G	T	Intron	–	rs50714352
		92833193	92833193	C	T	Exon	Synonymous SNV	rs46421166
		92833273	92833273	C	T	Intron	–	rs51678138
		92833286	92833286	T	C	Intron	–	rs45705750

Gene	Chr no.	Location (bp) Start	End	Strains B6	MRL/+	Region	Change	Variant ID
		92833302	92833302	T	C	Intron	–	rs50894680
		92835871	92835871	A	G	Intron	–	rs45886546
		92835887	92835887	A	G	Intron	–	rs46632834
		92835925	92835925	T	A	Intron	–	rs47396275
		92835947	92835947	T	C	Intron	–	rs48288639
		92835950	92835950	C	A	Intron	–	rs45708441
		92835961	92835961	C	–	Intron	–	–
		92835994	92835994	A	T	Exon	Synonymous SNV	rs47334964
		92836015	92836015	C	T	Exon	Synonymous SNV	rs50617380
		92836072	92836072	T	C	Exon	Synonymous SNV	rs46039319
		92836120	92836120	G	A	Exon	Synonymous SNV	rs50745645
		92836132	92836132	T	C	Exon	Synonymous SNV	rs49465794
		92836172	92836172	A	G	Intron	–	–
		92836208	92836208	T	C	Intron	–	rs50106637
		92836248	92836248	A	C	Intron	–	rs50508247
		92837027	92837027	G	A	Exon	Synonymous SNV	rs33504743
		92837149	92837149	T	C	Intron	–	rs46426201
		92839119	92839119	T	C	Intron	–	rs50615049
		92839341	92839341	G	T	Exon	Synonymous SNV	rs46885156
		92839428	92839428	A	C	Intron	–	rs47250679
		92840287	92840287	–	T	Intron	–	–

Gene	Chr no.	Location (bp) Start	End	Strains B6	MRL/+	Region	Change	Variant ID
		92840355	92840355	T	G	Intron	–	rs47524903
		92840387	92840387	T	C	Intron	–	rs48300311
		92840400	92840400	C	T	Exon	synonymous SNV	rs46870953
		92840436	92840436	A	G	Exon	Synonymous SNV	rs51331853
		92840440	92840440	C	T	Exon	Synonymous SNV	rs51553188
		92840567	92840567	A	T	Intron	–	–
		92840621	92840621	A	G	Intron	–	rs49727866
		92843814	92843814	T	C	Intron	–	rs32814582
		92844028	92844028	T	C	Intron	–	rs45701744
		92846032	92846032	G	T	Intron	–	rs48669406
		92846077	92846077	T	C	Intron	–	rs51010704
		92846106	92846106	T	C	Exon	Synonymous SNV	rs46518220
		92846109	92846109	T	C	Exon	Synonymous SNV	rs46528268
		92846265	92846265	C	T	Intron	–	rs33044164
		92846284	92846284	C	A	Intron	–	rs49358673
		92846296	92846304	ATGTGGCTT	–	Intron	–	–
		92846309	92846309	T	G	Intron	–	rs240469150
		92846340	92846340	T	A	Intron	–	rs50419882
		92846341	92846341	T	C	Intron	–	rs50984607
		92850078	92850078	G	A	Intron	–	rs46081866
		92850156	92850156	C	G	Exon	Synonymous SNV	rs49302213

Gene	Chr	Location (bp)		Strains		Region	Change	Variant ID
	no.	Start	End	B6	MRL/+			
		92850213	92850213	C	T	Exon	Synonymous SNV	rs48609021
		92850231	92850231	T	C	Exon	Synonymous SNV	rs51146338
		92852461	92852461	C	T	Intron	–	rs49769472
		92852477	92852477	A	G	Intron	–	rs46075410
		92852508	92852508	C	A	Intron	–	rs51124308
Mmp9	chr02	164953375	164953375	T	C	Exon	Non-synonymous SNV	rs13475086

chr, chromosome; SNV, single nucleotide variant; *Mmp2*, matrix metallopeptidase 2; *Mmp9*: matrix metallopeptidase 9; UTR, untranslated region.

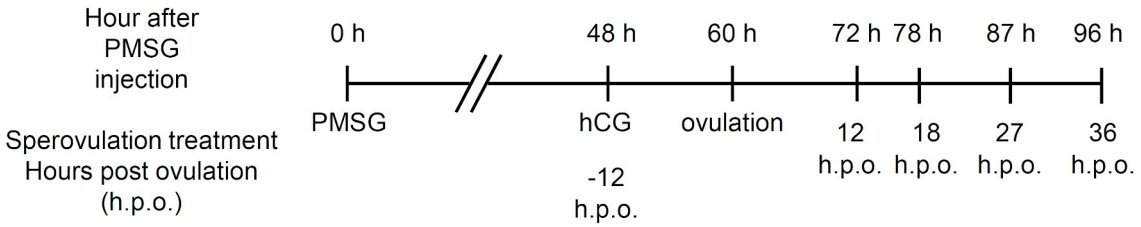

Figure 3-1. The superovulation treatment protocol used in the present study. Mice were injected with pregnant mare serum gonadotrophin (PMSG) intraperitoneally; 48 h after PMSG injection, defined as –12 h postovulation (h.p.o.), mice were injected intraperitoneally with human chorionic gonadotrophin (hCG) or had their ovaries removed. Ovaries were collected 24 h (12 h.p.o.), 30 h (18 h.p.o.), 39 h (27 h.p.o.) and 48 h (36 h.p.o.) after hCG injection.

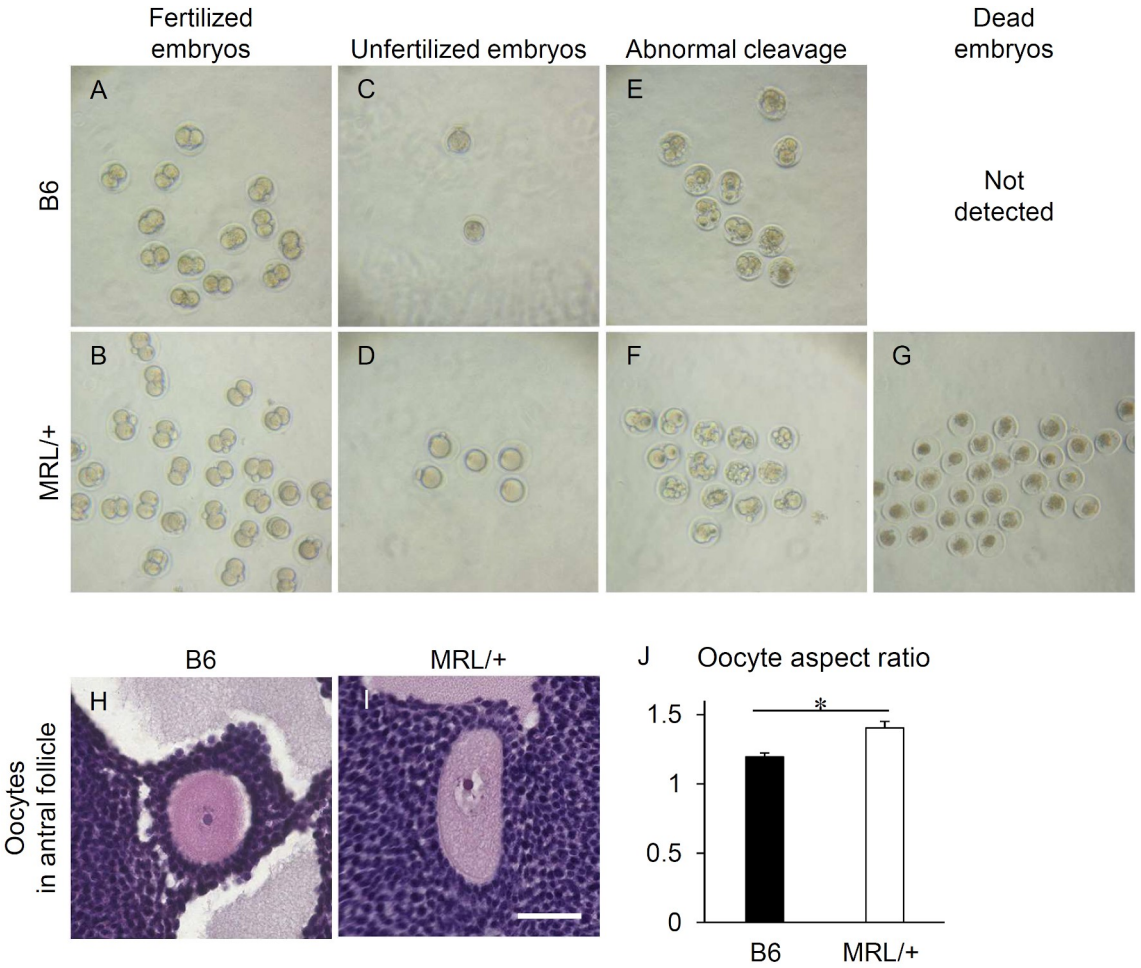

Figure 3-2. Morphological observations of embryos after IVF of oocytes obtained from superovulated mice.

(A and B) Fertilized embryos that have two cells of the same size.

(C and D) Unfertilized embryos.

(E and F) Abnormal cleavage in embryos, which have either three or more cells or two cells of different sizes.

(G) Dead embryos derived from MRL/+ mice that have a large cytoplasm and condensed cells.

(H and I) Morphological differences between oocytes contained in antral follicles at –12 h.p.o. in B6 and MRL/+ mice. Bar = 50 μm.

(J) The oocyte aspect ratio (maximum diameter/minimum diameter) in B6 mice (n = 4; 13–15 oocytes analyzed in each ovary) and MRL/+ mice (n = 4; 40–61 oocytes analyzed in each ovary). Data are the mean ± SE. *: $P < 0.05$ (Mann–Whitney *U*-test).

h.p.o.: hour postovulation, B6: C57BL/6N, MRL/+: MRL/MpJ.

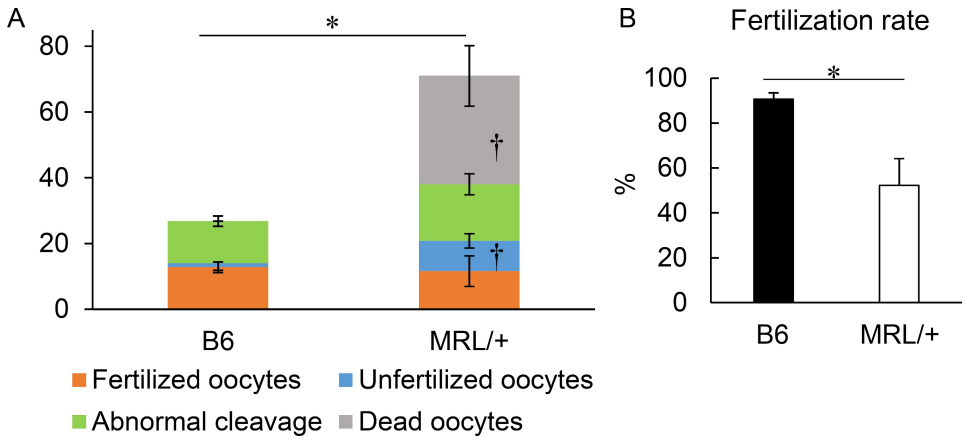

Figure 3-3. Results of the fertilization assay in embryos obtained from superovulated mice.
(A) Number of different types of embryos generated per mouse through IVF. Data are the mean ± SE (n = 5 in each strain). *$P < 0.05$ (Mann–Whitney *U*-test). $^{\dagger}P < 0.05$ compared with the same embryo type in B6 mice (Mann–Whitney *U*-test).
(B) Fertilization rate calculated from the number of fertilized and unfertilized embryos shown in **(A)**. Data are the mean ± SE ($n = 5$ in each strain). *$P < 0.05$ (Mann–Whitney *U*-test).
B6: C57BL/6N, MRL/+: MRL/MpJ.

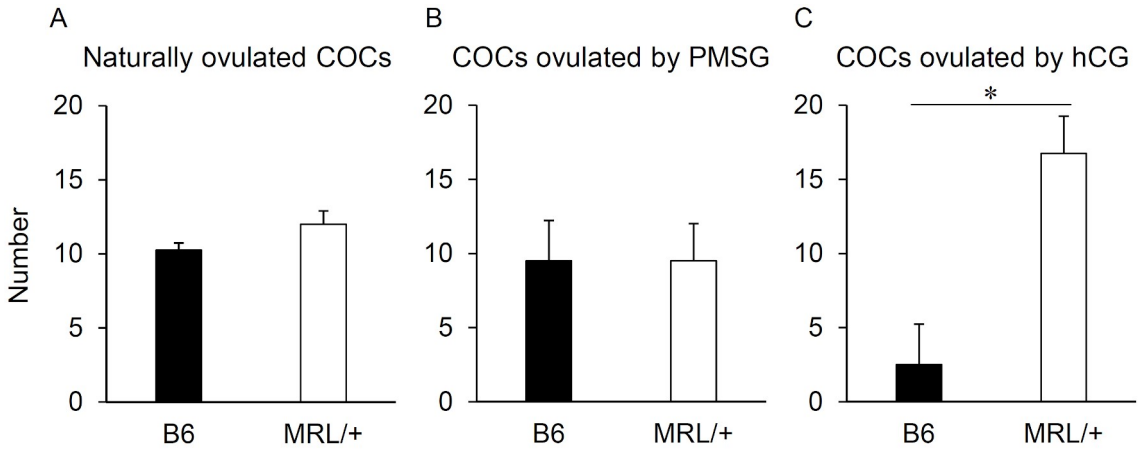

Figure 3-4. Number of cumulus oocyte complexes (COCs) produced **(A)** under a natural oestrous cycle and after injection of **(B)** pregnant mare's serum gonadotrophin (PMSG) or **(C)** human chorionic gonadotrophin (hCG). Data are the mean ± SE (n = 5 in each strain for **(A)**; n = 4 in each strain for **(B)** and **(C)**). There were no significant differences in the number of COCs ovulated between B6 and MRL/+ mice under a natural estrous cycle or after injection of PMSG. **P* < 0.05 (Mann–Whitney *U*-test).
B6: C57BL/6N, MRL/+: MRL/MpJ.

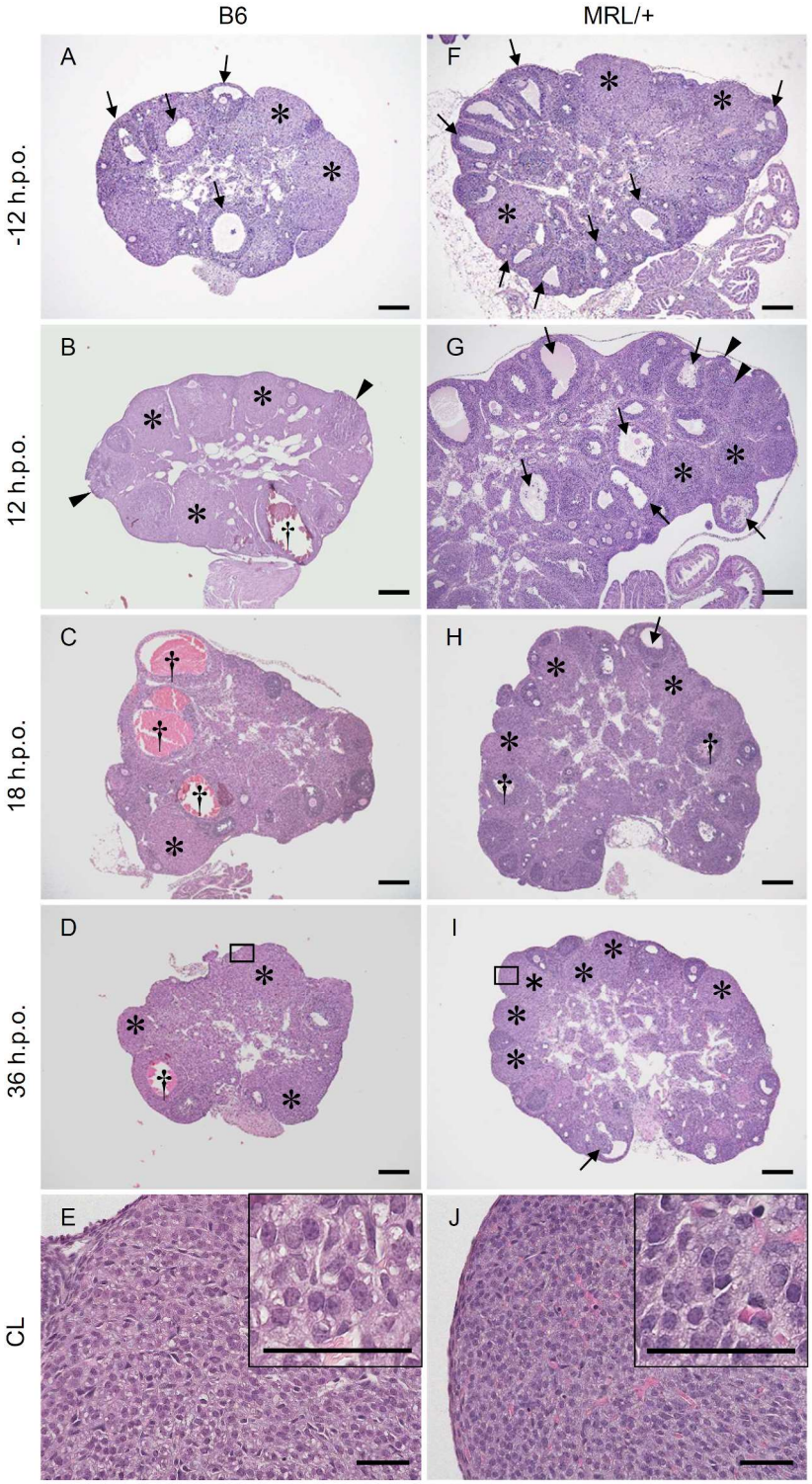

Figure 3-5. Ovarian histology before and after superovulation in B6 **(A-E)** and MRL/+ **(F-J)** mice. The squares indicated in **(D)** and **(I)** are magnified in **(E)** and **(J)** respectively, with insets showing lutein cells containing vacuoles. Arrows indicate antral follicles, arrowheads indicate ruptured follicles, daggers indicate hemorrhagic bodies and asterisks indicate corpora lutea. Bars = 300 μm **(A-D and F-I)**; 50 μm **(E and J)**.
CL: corpus luteum, h.p.o.: hour postovulation, B6: C57BL/6N, MRL/+: MRL/MpJ.

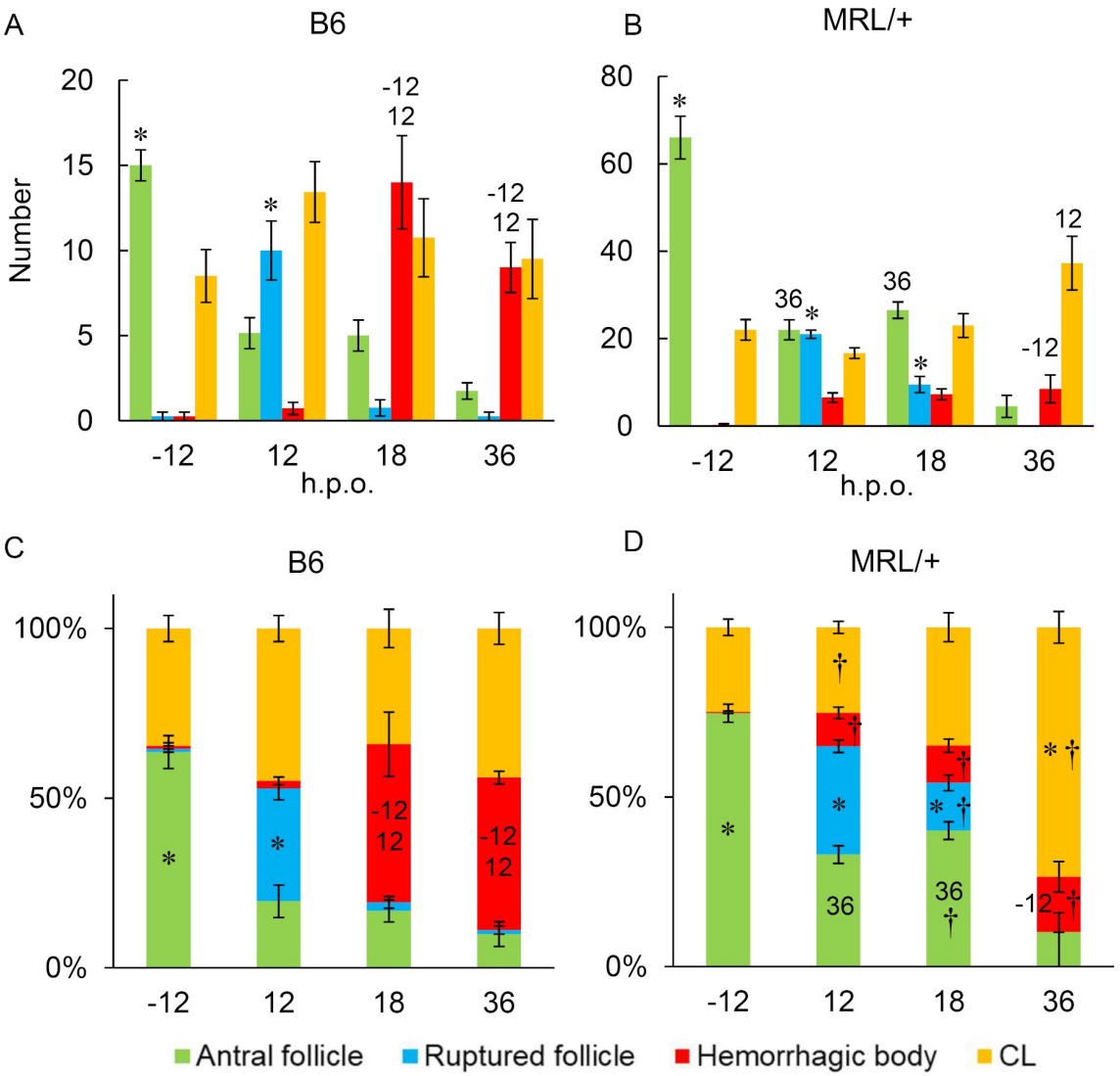

Figure 3-6. Number **(A and B)** and percentage **(C and D)** of ovarian follicle-related structures in superovulated B6 **(A and C)** and MRL/+ **(B and D)** mice. Data are the mean ± SE of ovaries from four mice in each group at –12, 18 and 36 h.p.o. and six mice in each group at 18 h.p.o. Asterisks indicate significant differences compared with the other three time points within the same strain are shown. Significant differences –12, 12 and 36 h.p.o. within the same strain are indicated as '–12', '12' and '36' respectively ($P < 0.05$, Kruskal–Wallis test followed by Scheffé's test). In **(D)**, the daggers indicate significant differences in the same structure compared with the B6 strain ($P < 0.05$, Mann–Whitney *U*-test).
h.p.o.: hour postovulation, CL: corpus luteum, B6: C57BL/6N, MRL/+: MRL/MpJ.

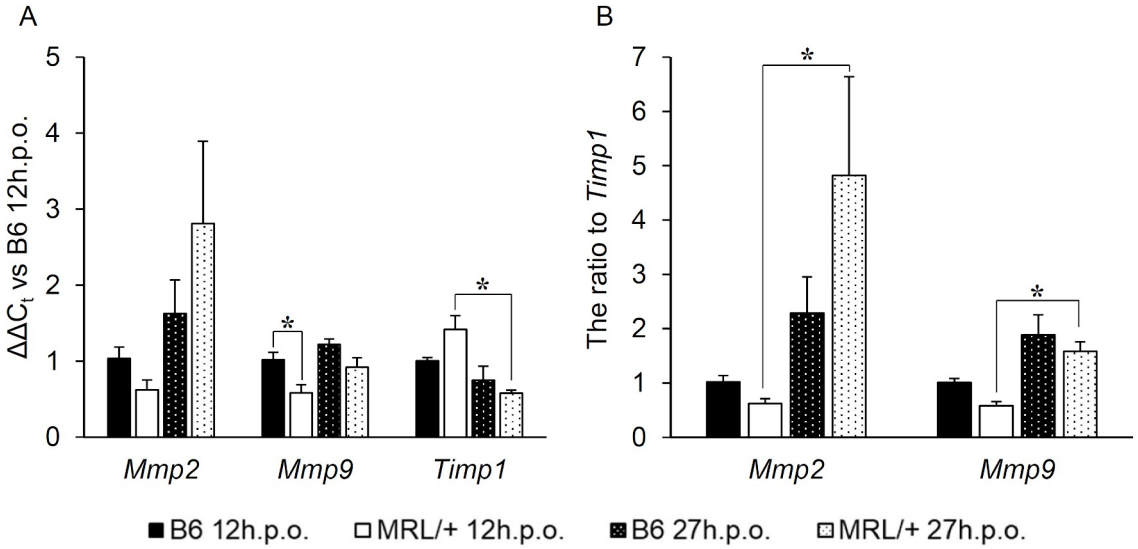

Figure 3-7. Expression of MMPs and TIMPs in ovaries during luteinization.

(A) Expression of *Mmp2*, *Mmp9*, and *Timp1* mRNA during luteinization in ovaries of superovulated mice.

(B) The ratio of MMP mRNA to *Timp1* expression, as determined by quantitative real-time PCR at 12 and 27 h.p.o.. Data are the mean ± SE. (n = 4 for each strain at each time point). **P* < 0.05 (Mann–Whitney *U*-test).

h.p.o.: hour postovulation, *Mmp2, 9*: matrix metallopeptidase 2, 9, *Timp 1*: tissue inhibitor of metalloproteinase 1, B6: C57BL/6N, MRL/+: MRL/MpJ.

Chapter 4

Altered ciliary morphofunction in the oviductal infundibulum in autoimmune disease-prone mice

Introduction

In Chapter 1, the correlation between the progression of autoimmune disease and the dysfunction of ovulation and oocyte pick-up was revealed. Next, the author examined the histopathology and morphofunction of ciliated epithelium on the oviductal infundibulum in MRL/lpr mice. Oocyte pick-up is one of the primary functions of the oviduct in reproduction, in which it takes oocytes produced in the ovary into the oviductal lumen [46], while infundibulum dysfunction prevents oocyte fertilization. One theory regarding the underlying mechanism of oocyte pick-up is that well-controlled ciliary beating on the infundibulum ciliated epithelium transports oocytes into the lumen [108], although the actual physical mechanism of oocyte pick-up is not fully understood.

Oviduct morphofunction can be affected by the condition of surrounding tissues. For example, the spread of inflammation in peritoneal cavity and/or uterus to the oviductal lumen induces oviductal swelling and/or adhesion, leading to luminal interruption in both human and animals [76,138]. Peritubal adhesions or damage to oviduct lining resulted from inflammatory conditions can impair tubal mobility, sperm and embryo transport, and oocyte pick-up [76]. In addition, in Holstein repeat breeder cows, oviductal luminal blockage severely impairs fertility [106]. However, it is still unknown whether the infundibulum ciliary functions driving the healthy oocyte pick-up are impaired by these immunological disorders or other endogenous factors.

In this Chapter, the effects of the autoimmune abnormalities on the infundibulum cilia regulating oocyte pick-up in MRL/lpr mice were determined. In addition to the oviduct, the author also examined the ciliary morphofunction of tracheal ciliated epithelial cells as a representative organ for motile cilia possession and compared their morphology with that of the oviduct. The author proposes the novel pathological theory that altered ciliary function triggered by an autoimmune abnormality contributes to oocyte pick-up dysfunction and note interesting similarities of ciliary morphofunction in the oviduct and trachea.

Materials and Methods

Animals

Animal experimentation was approved by the Institutional Animal Care and Use Committee of the Graduate School of Veterinary Medicine, Hokkaido University (Approval No. 15-0079). Experimental animals were handled in accordance with the Guide for the Care and Use of Laboratory Animals, Graduate School of Veterinary Medicine, Hokkaido University (approved by the Association for Assessment and Accreditation of Laboratory Animal Care International). Female MRL/+ and MRL/lpr mice at 3 and 6 months of age were obtained from Japan SLC, Inc.. The housing of mice was performed as done in Chapters 1, 2, and 3. For histoplanimetry of measurement of percentage of ciliated epithelial cells and number of CD3-positive T-cells in infundibulum, the mice under natural estrous cycle were used. The estrous cycle of each mouse was confirmed by monitoring vaginal smears. For evaluation of ovulation and oocyte pick-up by the oviduct, ultrastructural analysis, and CBF measurement, superovulation treatment was conducted as done in Chapter 1. Briefly, PMSG (ASKA Animal Health Co., Ltd.) was injected intraperitoneally in mice (200 μL of 37.5 IU/mL gonadotropin per mouse). After 48 h of PMSG injection, mice were injected intraperitoneally with the same dose of hCG (ASKA Animal Health Co., Ltd.). Twenty-four hours after hCG injection, all mice were euthanized by methods performed in Chapters 1, 2, and 3.

Evaluation of autoimmune disease condition

As the indices of an autoimmune disease, the S/B and anti-dsDNA antibody levels in mice serum were measured as done in Chapter 1. Anti-dsDNA antibody levels in mice serum were measured using the LBIS anti dsDNA-Mouse ELISA kit (FUJIFILM Wako Pure Chemical Co., Ltd., Osaka, Japan) according to the manufacturer's instructions.

Evaluation of ovulation and oocyte pick-up by the oviduct

PUR was calculated as done in Chapter 1. Briefly, the ovaries and oviductal ampulla were collected from mice and immediately placed in 0.01 M PBS. The COCs present in the ampulla were pushed out into a glass dish with 0.01 M PBS and counted. Ovaries were fixed with 4% PFA at 4°C overnight, embedded in paraffin, and cut into 10 μm-thick whole serial sections, which were used for the histological counting of OOs from the ovaries. PUR was then calculated as

follows: PUR (%) = 100 × number of COCs / number of OOs.

Histoplanimetry

Mice oviducts and tracheas were collected and fixed with 4% PFA at 4°C overnight, embedded in paraffin, and cut into 3-μm-thick sections, which were then used for HE staining and immunohistochemistry. To investigate the percentage of ciliated cells composing the epithelium in the infundibulum, the number of total epithelial cells (a) and secretory cells (b) in three different regions per one section were manually counted. Three semi-serial sections stained with HE with 20-μm intervals were used, and the percentage of ciliated epithelial cells was calculated as follows: percentage of ciliated epithelial cells (%) = [100 × number of total epithelial cells (a) – number of total secretory cells (b)] / number of total epithelial cells (a)

Some sections were immunostained with rabbit anti-CD3 primary antibody as performed in Chapters 1 and 2. To quantify the degree of T-cell infiltration in the infundibulum, the number of CD3-positive T-cells per 1 μm^2 was counted by using BZ-X Analyzer of Fluorescence Microscope BZ-X710 (Keyence, Osaka, Japan).

Ultrastructural analysis

For transmission electron microscope (TEM) analysis, perfusion fixation was performed on 3- and 6-month-old superovulated MRL/+ and MRL/lpr mice. The caudal vena cava was cut and released under deep anesthesia and 20 mL of PBS and half-strength Karnovsky's fixing solution (2.5% glutaraldehyde, 2% PFA, 0.1 M PB, pH 7.4) perfused from the left ventricle to the whole body. The detached infundibulum from the oviducts and the trachea beneath the isthmus of the thyroid grand were post-fixed with 1% osmium tetroxide in 0.1 M PB for 2 hours at 4°C. Specimens were dehydrated using a graded alcohol series and embedded in epoxy resin (Quetol 812 Mixture; Nisshin EM CO., Ltd., Shinjuku, Tokyo, Japan). The epoxy blocks were cut into 60 nm-thick sections, stained with uranyl acetate and lead citrate, and examined via a JEM-1210 microscope (JEOL Ltd., Akishima, Tokyo, Japan).

The orientation of the ciliary central microtubules was measured as previously described [40]. The ciliary orientation is defined by the plane formed by the central tubules and is used to estimate ciliary beat direction by measuring the angle between the central tubule plane and a reference line [100]. Reference lines were drawn through the central pairs of microtubules using Image J software

(National Institutes of Health). The mean vector length (r_{cell}) represents the circular variance of these angles within the cell. In one specimen, more than 10 cells which have more than 10 cilia clearly expressing pairs of central microtubules were chosen and analyzed for calculating of the average r_{cell} in each specimen. The ciliary height on the ciliated epithelial cells was defined as the distance between "the upper end of the cilia" and "luminal surface of the cell." The height was measured using Image J on more than 10 ciliated cells within one specimen.

Ciliary beat frequency (CBF) measurement

Ciliary beating was analyzed by a program developed by Dr. Jason J. Chen [16]. The collected oviductal and tracheal specimens of the superovulated mice were kept in D-MEM (high glucose) with L-glutamine and phenol red (D-MEM) (FUJIFILM Wako Pure Chemical Co., Ltd.) at 37°C. Using a stereoscope, the infundibulum was detached from the oviduct. The excess soft tissue was removed via microdissection and the trachea was sectioned into 1 mm^2 to 4 mm^2 pieces, which were then incubated for 30 min in D-MEM at 37°C and placed onto slides for observation (Figure 4-1A). As shown in Figure 4-1A, the oviductal infundibulum was put into a chamber with D-MEM (Matsunami Glass Industry Co., LTD., Kishiwada, Osaka, Japan), following a published method previously used to study CBF in oviducts [108]. Trachea tissue pieces were also put under cover slips in D-MEM (Figure 4-1B). Ciliary movements were observed using a phase contrast microscope (BX50, Olympus Co., Ltd., Shinjuku, Tokyo, Japan) and recorded through the ocular lens using an iPhone 6S (Apple Inc., Cupertino, California, U.S.A.) at 240 frames per second.

The program used for CBF data analysis was written in MATLAB (MathWorks Inc., Natick, MA, USA) was used for CBF data analysis as described previously [16]. A 3-second video was isolated from each recording and regions of interest (ROIs) selected according to histologic findings. Power spectrum graphs were then generated to determine the CBF of the samples. The mean CBF values for each individual specimen were obtained by analyzing more than 100 ROIs and averaging CBF values of those ROIs.

Statistical analysis

Results are expressed as the mean ± SE. Statistical analysis was performed as done in Chapters 1. 2, and 3.

Results

Histology and inflammation of infundibulum in the oviducts of MRL/lpr mice

The histopathology of the infundibulum during aging and the estrous cycles were examined (Figure 4-2A). The oviductal epithelium mainly consists of ciliated epithelial cells and secretory cells in mice [24,96]; however, these cell populations appeared to change with the estrous cycle (Figure 4-2A). Briefly, in both MRL/+ and MRL/lpr mice, ciliated epithelial cells were more abundant in the estrus than in the anestrus phase, as confirmed by histoplanimetry (Figure 4-2B). The percentage of ciliated epithelial cells in MRL/lpr mice at 6 months was significantly lower than in MRL/+ mice at the same age throughout the estrous cycle (Figure 4-2A and B). The percentage of ciliated epithelial cells significantly decreased at 6 months than at 3 months in MRL/lpr mice, while the percentage did not change with aging in MRL/+ mice (Figure 4-2A and B). In addition, few CD3-positive T-cells were observed in the lamina propria and in the muscle layer of the infundibulum in MRL/+ mice throughout the estrous cycle at both ages (Figure 4-2C and D). However, there were numerous CD3-positive T-cells in 6-month-old MRL/lpr mice that were more notable at the anestrus compared with the estrus phase (Figure 4-2C and D). MRL/lpr mice at 6 months showed a significant increase in CD3-positive T-cells compared to MRL/+ at both stages (Figure 4-2D).

Ultrastructure and altered beating direction of oviductal cilia in MRL/lpr mice

The ultrastructure of ciliated epithelial cells in the oviduct of MRL/+ and MRL/lpr at 3 and 6 months old is shown in Figure 4-3A-H. No remarkable difference in cilia density was noted between mouse strains and ages, but the oviductal ciliary height from the luminal top of the ciliated epithelial cell seemed to be shortest in MRL/+ mice at 3 months old compared with other test groups (Figure 4-3A, C, E, and G, white arrows), which is also confirmed in the oviductal ciliated epithelial cells in the HE-stained sections (Figure 4-3A, C, E, and G, insets). Furthermore, the orientation of the central microtubules in a cilium, which indicates the direction of cilial motion, was more randomized in 6 month MRL/lpr mice compared with the others (Figure 4-3B, D, F, and H, white lines). However, there are no age-related differences in cilia composing structures in MRL/lpr mice (Figure 4-3F and H, insets).

These morphological findings were summarized in Figure 4-3I-J. At 3 months of age, the oviductal ciliary height from the luminal top of the ciliated epithelial cell was significantly higher

in MRL/lpr than MRL/+ mice (Figure 4-3I). While there was no change in the oviductal ciliary height of MRL/lpr mice with age, oviductal ciliary height of MRL/+ mice increased with aging. The variance values of the angles within a pair of central microtubules (Figure B, D, F, and H, white lines) represents the cooperativity of the ciliary beating direction in a given cell. At 6 months of age, MRL/lpr mice showed significantly lower cilia alignment in the oviductal infundibulum than that in MRL/+ mice, while there were no differences among two strains at 3 months old (Figure 4-3J).

Altered oviductal ciliary beating in MRL/lpr

The CBF were recorded using stereomicroscopy, and representative still images from these movies are shown in Figure 4-4A (with movies in Movie 4-1 to 4). From these movies, MRL/lpr mice had significantly higher oviductal CBF in the infundibulum at both 3 and 6 months (11.41 ± 0.09 Hz and 10.67 ± 0.21 Hz, respectively) compared to MRL/+ mice at each corresponding age (10.25 ± 0.27 Hz and 9.18 ± 0.37 Hz, respectively) (Figure 4-4B). Importantly, the oviductal CBF showed significant age-related decreases in MRL/lpr mice at 6 months.

Histology and inflammation of tracheal mucosa in MRL/lpr mice

In all examined mice, the tracheal mucosa was lined with ciliated pseudo-stratified columnar epithelium, and the epithelia heights were higher at 6 months old compared to 3 months old (Figure 4-5A). Furthermore, in 6-month-old MRL/lpr mice, the non-ciliated cells and mononuclear cells beneath epithelium were frequently exposed, and a part of their epithelium was covered with mucin layer (Figure 4-5A, arrows). As shown in Figure 4-5B, the mononuclear cells were CD3-positive and tended to increase in number with aged mice, being particularly abundant in the lamina propria as well as mucosal epithelium in 6-month-old MRL/lpr mice.

Ultrastructure of tracheal ciliated epithelial cells in MRL/lpr mice

The ciliary ultrastructure of the trachea of MRL/+ and MRL/lpr mice at 3 months and 6 months of age showed no remarkable morphological differences among strains is shown in Figure 4-6A-H. Furthermore, there were no significant differences in both the tracheal ciliary height and tracheal cilia alignment among strains and ages (Figure 4-6I and J).

Altered systemic ciliary beating in MRL/lpr mice

The author also recorded the tracheal CBF as a representative tissue to indicate systemic cilia function using stereomicroscopy and show representative still images from movie files in Figure 4-7A (with movies in Movie 4-5 to 8). While the tracheal CBF in 3-month-old MRL/lpr mice (8.16 ± 0.31 Hz) was significantly higher than that in MRL/+ of the same age (7.37 ± 0.17 Hz), the tracheal CBF in MRL/lpr at 6 months (6.29 ± 0.41 Hz) was significantly lower than in MRL/+ of the same age (7.39 ± 0.26 Hz). Similar to oviductal CBF, MRL/lpr mice showed reduced tracheal CBF with aging (Figure 4-7B).

Autoimmune disease affects systemic ciliary function

The S/B, serum levels of anti-dsDNA antibody, the numbers of COCs and OOs and PUR in the individual mice used in this Chapter were also measured as done in Chapter 1 to examine the relationship between ciliary beating in both the oviduct and trachea and autoimmune abnormality, ovulation, and oocyte pick-up. Briefly, as described in Chapter 1, MRL/lpr mice showed both significantly greater splenomegaly and significantly higher serum levels of anti-dsDNA antibody at 3 and 6 months of age compared with MRL/+ mice (data not shown). In addition, the COC, OO, and PUR values in 6-month-old MRL/lpr mice (5.36 ± 0.95, 7.18 ± 1.46, and 76.93 ± 6.33 %, respectively) were significantly lower as compared with those of 3-month-old MRL/lpr mice (41.63 ± 5.47, 43.57 ± 6.35, and 100.69 ± 3.31 %, respectively) and with those of 6-month-old MRL/+ mice (20.75 ± 1.82, 20.63 ± 1.60, and 101.10 ± 5.11 %, respectively). Furthermore, in MRL/+ mice, significant age-associated reductions were observed for COCs and OOs, but not in PUR (41.63 ± 2.98, 39.29 ± 2.02, and 101.73 ± 3.83 % in 3-month-old MRL/+ mice, respectively). Based on these values as well as the values of CBF, r_{cell} and ciliary height, correlation analysis was performed for these parameters (Table 4-1 to 3).

First, correlation analysis between the PUR and the number of COCs and OOs was performed to examine the relationship between oocyte pick-up and ovulation (Table 4-1). In all of the mice included in the analysis and MRL/lpr mice, PUR showed significant positive correlations with both the COCs ($P < 0.01$) and the OOs value ($P < 0.05$).

Second, correlation analyses between ultrastructural morphological changes in both the oviduct and trachea and autoimmune abnormalities was performed (Table 4-2). The oviductal and tracheal r_{cell} values showed significant strong positive correlations in MRL/lpr mice ($P < 0.001$)

while in MRL/+, the oviductal ciliary height correlated negatively with the S/B ratio ($P < 0.05$).

Finally, to examine the relationship between ciliary beating in both the oviduct and trachea and autoimmune abnormality, ovulation, and oocyte pick-up, correlation analysis was performed for these parameters (Table 4-3). In all of the mice included in the correlation analysis, the oviductal CBF showed significant positive correlations with S/B ($P < 0.05$) and the serum anti-dsDNA antibody levels ($P < 0.01$), which are indices of autoimmune disease. On the other hand, in MRL/lpr mice, the oviductal and tracheal CBF showed significant negative correlations with S/B ($P < 0.05$). Furthermore, in MRL/+ mice, oviductal CBF correlated positively with the number of COCs ($P < 0.05$). Additionally, all mice showed strong positive correlations between the tracheal CBF and the number of COCs and OOs ($P < 0.001$), with MRL/lpr mice also showing a strong positive correlation both the oviductal and tracheal CBF and the number of COCs and OOs ($P < 0.001$). In addition tracheal CBF showed a significant positive correlation with PUR in all mice examined ($P < 0.01$) and MRL/lpr mice ($P < 0.01$), with MRL/lpr mice also showing a significant positive correlation between the oviductal and tracheal CBF ($P < 0.01$).

Discussion

As reported in previous studies [92] and the present study, female MRL/lpr mice develop systemic autoimmune disease at the age of 3 months, which becomes more severely exacerbated at 6 months of age. In MRL/lpr mice that developed severe autoimmune diseases, a large number of immune cells infiltrated the oviductal and the tracheal mucosa as reported for other systemic organs such as the ovaries, kidneys, lungs, skin, and liver [33,34,49,92,144]. Both the healthy oviduct and trachea contain a heterogeneous population of innate and adaptive immune cells, including T-cells [3,54]. In the mucosa, these T-cells play an important role in maintaining mucosal homeostasis and are involved in inflammatory regulation, tissue repair, and protection against infectious agents [3]. Therefore, it is suggested that the excess auto-reactive lymphoproliferation due to the failure of negative selection of thymocytes by Fas protein disrupts the normal immune balance and induces the infiltration of numerous T-cells in both oviduct and trachea of older MRL/lpr mice.

At 3 months, there was no difference in ovulation and oocyte pick-up indices between both strains, but the oviductal epithelium of MRL/lpr mice had longer cilia and faster CBF compared with MRL/+ mice. For each cell type there is a specific range of normal lengths for cilia, and even slight deviations outside of this range are often sufficient to generate pathological phenotypes [5]. Mice lacking ciliary length control show female infertility because the elongated cilia in the oviduct cannot maintain proper fluid flow leading to the tubal obstruction [88]. While cilium elongated in MRL/+ mice with aging, ciliary elongation occurred at an earlier age in MRL/lpr mice than MRL/+ mice. In addition, the inflammatory cytokine stimulation produced during chronic inflammation induces the sustained elongation of primary cilia, another type of cilia than examined in this study, and the subsequent loss of length regulation function [31]. Although the direct effect and mechanism of ciliary elongation in 3-month-old MRL/lpr mice remains unclear, the author propose that the faster oviductal CBF in MRL/lpr mice might compensate for altered cilia function due to morphological changes and maintain normal oocyte pick-up.

As reported in Chapter 1, MRL/+ and MRL/lpr mice show decreased ovulation with aging, with the latter showing a more remarkable decrease in ovulation as well as oocyte pick-up. Furthermore, the oviducts of 6-month-old MRL/lpr mice showed decreased percentage of ciliated epithelial cells, decreased CBF, and lost ciliary cooperativity than 3-month-old MRL/lpr mice. The infundibulum mucosa and the ovarian surface are closely associated with slow COCs release

[37]. In addition, the process of the oocyte pick-up representatively comprises of both accurate oviductal ciliary beating and the transient adhesion of COCs to the tips of cilia [63,89,120,121]. In fact, considering the strong correlation between “the number of OOs and COCs” and “the oviductal CBF and the PUR” in MRL/lpr mice, the interaction and adhesion of cumulus cells and cilia in the infundibulum epithelium likely play a key role in the pathological state of ovulation and oocyte pick-up dysfunction in MRL/lpr mice. Further, these results imply that oocytes or the cumulus cells themselves regulate oviductal ciliary function to promote healthy oocyte pick-up. The author therefore considered that the severe morphofunctional changes of oviductal epithelium, in particular those of cilia, found in 6-month-old MRL/lpr mice would ultimately impair not only ovulation but also oocyte pick-up.

The oviductal CBF showed significant correlation with the extent of splenomegaly in all mice examined and MRL/lpr, indicating a relationship between autoimmune abnormality and ciliary function. MRL/+ mice exhibit autoimmune disease-associated abnormalities but have milder symptoms that manifest much later in life compared to MRL/lpr mice [56]. Several inflammatory factors are reported to potentially alter the CBF in both human oviduct and respiratory tracts in *ex vivo* experiments, including IL-6 [94], IL-4, IL-5, IL-9, IL-13, IFN-ɤ [39], and platelet-activating factor [62]. Previous reports indicate that the high serum levels of IL-6, IL-9 and IFN-ɤ, which are produced by T-cells, are involved in lupus development in MRL/lpr mice [6,122,145]. Thus, it is proposed that variations in levels of these cytokines in serum and/or tissues alters the oviductal CBF of MRL/lpr mice. The inflammatory factors affecting CBF may be involved in the complicated regulation of ciliary function in mice, as no significant correlations between the oviductal CBF and oocyte pick-up were found. It is proposed that altered ciliary function triggered by an aberrant immune condition affects the pivotal physiological function of the reproductive tract.

In addition to oviductal cilia, the author examined tracheal cilia to evaluate systemic ciliary morphofunction. The tracheal CBF in MRL/lpr decreased with age and correlated negatively with S/B. These results indicate that the progression of the systemic autoimmune abnormality in MRL/lpr mice alters systemic ciliary function, similar to oviductal cilia. However, in contrast to oviductal morphology, the ultrastructure of tracheal ciliated cells did not exhibit any significant changes. The molecular pathogenesis of altered ciliary beating speed can thus be explained by a systemic inflammatory response, while the abnormality of the oviduct cilia ultrastructure seems

to involve an additional local pathological response. Female patients with primary ciliary dyskinesia (PCD), the congenital autosomal recessive genetic disorder characterized by total or partial dysfunction of the ciliary cells due to ciliary ultrastructural abnormalities, largely show such respiratory alterations and sometimes are infertile [4,71]. However, some female PCD patients with severely dysfunctional respiratory cilia successfully conceive and deliver babies [129]. In feline PCD, the ultrastructural defects in the oviductal cilia were observed along with early lesions of bronchiectasis suggested by computed tomography, although the cat did not show no clinical signs of respiratory tract [103]. The features of ciliary ultrastructural abnormalities in PCD vary in the oviduct and respiratory tract, so it is proposed that the effects of mutated proteins and protein expression would vary in these different tissues [75]. Taken together, due to the tissue-related differences in the function and/or expression of disease-associated molecules, the ciliary morphofunction of the oviduct is more susceptible to aging and/or immune abnormalities than the trachea and severely impacts reproductive function in MRL/lpr mice.

The author also found histological and functional relationship between the oviductal tract and respiratory tract in mammals. The strong positive correlation between the oviductal and tracheal CBF and ciliary cooperativity gives rise to two theories. The first theory is that the one or more molecules circulating systemically have identical effects on the systemic ciliary function. The second theory is that the inflammatory substances produced by immune cells, such as T-cells, infiltrate into the tissue and alter the ciliary beating patterns, resulting in the systemic decrease of CBF. The clinical reports in women with tubal ectopic pregnancies, which is suspected to be caused by the oviductal ciliary abnormalities, support comparisons between this study and human pathology. Both oviductal and nasal CBF in those patients correlated positively and was decreased compared with healthy women [74,90]. The peptide hormone adrenomedullin was reported to be involved in the molecular pathogenesis of tubal ectopic pregnancies and decreased oviductal and nasal CBF. The significant positive correlation between the tracheal CBF and the oocyte pick-up rate in MRL/lpr mice interestingly suggests that changes in the tracheal ciliary beating reflects that of the oviductal reproductive function in mice. Therefore, the further study on the functional correlation between tracheal cilia and reproductive tract in female livestock animals would indicate the possibility that fertility can be estimated by the pathology of respiratory tract.

In human patients, ciliary morphofunctional abnormalities are observed after infection and inflammation in both the lower and upper respiratory tract and is referred to as secondary ciliary

dyskinesia [4,111]. Additionally, in human patients with granulomatosis with polyangiitis, a potentially lethal systemic autoimmune disease characterized by necrotizing vasculitis of small arteries and veins [67], the nasal CBF is severely impaired [127]. In the patients with asthma, an inflammatory respiratory disease, both the secondary ciliary dysfunction and the secondary ultrastructural abnormalities of bronchial epithelium are closely related to asthma severity [123]. The ciliary ultrastructural abnormalities in patient airways were also reported to be associated with long-lasting airways infections [20]. In the female PCD patients, the immobility of cilia on oviductal epithelial cells leads the oocyte transportation failure [78]. It is estimated that the ovulation disorders and oocyte pick-up by oviducts is also involved in the infertility of the patients with dysfunction of motile cilia.

In conclusion, oocyte pick-up on the oviductal infundibulum is regulated by ciliary function, requires appropriate beating speed and coordinated beating directions and becomes abnormal upon impairment of the local environmental immune balance in ciliated epithelium during systemic autoimmune disease conditions in MRL/lpr mice. A close correlation between the change of ciliary morphofunction in the respiratory tract and that of morphofunction in the reproductive tract is also found, which implies possibility that non-invasive methods to evaluate the oocyte transporting function of oviducts by means of the respiratory evaluation in live animals.

Summary

In Chapter 4, the author investigated the relationship between autoimmune disease or oocyte pick-up and infundibulum morphofunction by focusing on the ciliated epithelium using MRL/+ and MRL/lpr mice at 3 and 6 months of age. As the indices of ciliary morphofunction, the author examined the percentage of ciliated epithelial cells, ciliary height, the index of cilia beating direction, and CBF in the infundibulum. In MRL/lpr mice, the percentage of ciliated epithelial cells was decreased with autoimmune disease progression. Although ciliary height and CBF were higher and faster in MRL/lpr mice than in MRL/+ mice at 3 months, the absolute CBF values in MRL/lpr mice were lower with autoimmune disease progression. At 6 months, ciliary height did not differ between mouse lines, but the index of cilia beating direction indicated randomized patterns in MRL/lpr mice. Taken together with the significant T-cells infiltration in the infundibulum of MRL/lpr mice at 6 months of age and the strong correlation between the oviductal CBF and the PUR in MRL/lpr mice, it is suggested that oocyte pick-up is affected by altered ciliary morphofunction including fewer cilia, inappropriate beating speed and uncoordinated beating directions under the local inflammation in ciliated epithelium during systemic autoimmune disease conditions in MRL/lpr mice. In addition, the author found a close correlation between the change of ciliary morphofunction in the respiratory tract and that of morphofunction in the reproductive tract, which suggests that changes in the tracheal ciliary morphofunction can reflect that of the oviductal reproductive function in mice.

Tables and Figures

Table 4-1. Spearman's correlation coefficient (ρ) between oocyte pick-up and ovulation.

		Parameters	
	Strains	*COCs*	*OOs*
PUR	All mice	0.547**	0.416*
	MRL/+	0.212	-0.156
	MRL/lpr	0.641**	0.563*

*$P < 0.05$; **$P < 0.01$; MRL/+: MRL/MpJ; MRL/lpr: MRL/MpJ-Fas$^{lpr/lpr}$; PUR: oocyte pick-up rate; COCs: cumulus oocyte complexes; OOs: ovulated oocytes.

Table 4-2. Spearman's correlation coefficient (ρ) between the oviductal or tracheal ciliary beat frequency and the indices of the autoimmune disease, ovulation or oocyte pick-up function.

		Parameters					
	Strains	*S/B*	*Anti-dsDNA antibody*	*COCs*	*OOs*	*PUR*	*Oviductal CBF*
Oviductal	All mice	0.391*	0.507**	0.241	0.231	0.019	-
CBF	MRL/+	-0.255	-0.165	0.530*	0.349	0.463	-
	MRL/lpr	-0.489*	0.008	0.720***	0.727***	0.425	-
Tracheal	All mice	-0.447	-0.195	0.686***	0.749***	0.382**	0.249
CBF	MRL/+	-0.083	-0.333	-0.356	-0.171	-0.189	-0.058
	MRL/lpr	-0.649*	0.115	0.844***	0.825***	0.637**	0.636**

*$P < 0.05$; **$P < 0.01$; ***$P < 0.001$; MRL/+ = MRL/MpJ; MRL/lpr = MRL/MpJ-*Fas*$^{lpr/lpr}$; CBF: ciliary beat frequency; S/B: ratio of spleen weight to body weight; Anti-dsDNA: anti-double-stranded DNA; COCs: cumulus oocyte complexes; OOs: ovulated oocyte; PUR: oocyte pick-up rate.

Table 4-3. Spearman's correlation coefficients (ρ) between the oviductal and tracheal ultrastructure and the ratio of spleen weight to body weight.

		Parameters		
	Strains	*S/B*	*Oviductal r_{cell}*	*Oviductal ciliary height*
Oviductal r_{cell}	All mice	-0.482	-	-
	MRL/+	0.036	-	-
	MRL/lpr	-0.590	-	-
Tracheal r_{cell}	All mice	-0.351	0.3879	-
	MRL/+	0.381	-0.108	-
	MRL/lpr	-0.483	0.952^{***}	-
Oviductal ciliary height	All mice	0.077	-	-
	MRL/+	-0.771^{*}	-	-
	MRL/lpr	0.570	-	-
Tracheal ciliary height	All mice	0.024	-	-0.318
	MRL/+	0.500	-	-0.313
	MRL/lpr	-0.524	-	-0.147

*$P < 0.05$; **$P < 0.01$; MRL/+ = MRL/MpJ; MRL/lpr = MRL/MpJ-*Fas*$^{lpr/lpr}$; S/B: ratio of spleen to body weight.

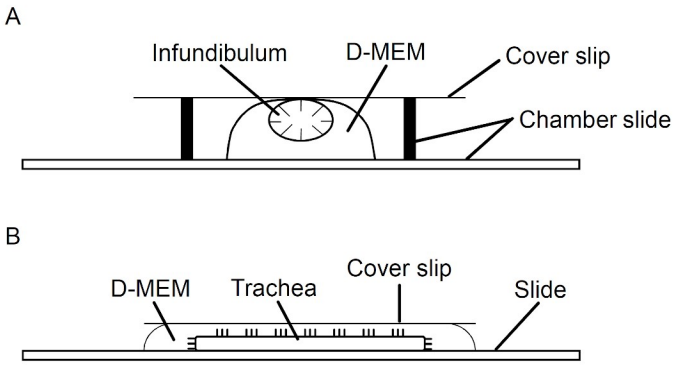

Figure 4-1. Scheme of the preparation for the ciliary beat frequency measurement.
(A) Oviductal infundibulum preparation schematic. The infundibulum is placed into the drop of D-MEM (high glucose) with L-Glutamine and phenol red (D-MEM) and covered with a cover slip so that the ciliated epithelium faces the cover slip.
(B) Trachea preparation schematic. The pieces of trachea are placed into D-MEM on a slide and sealed with a cover slip.

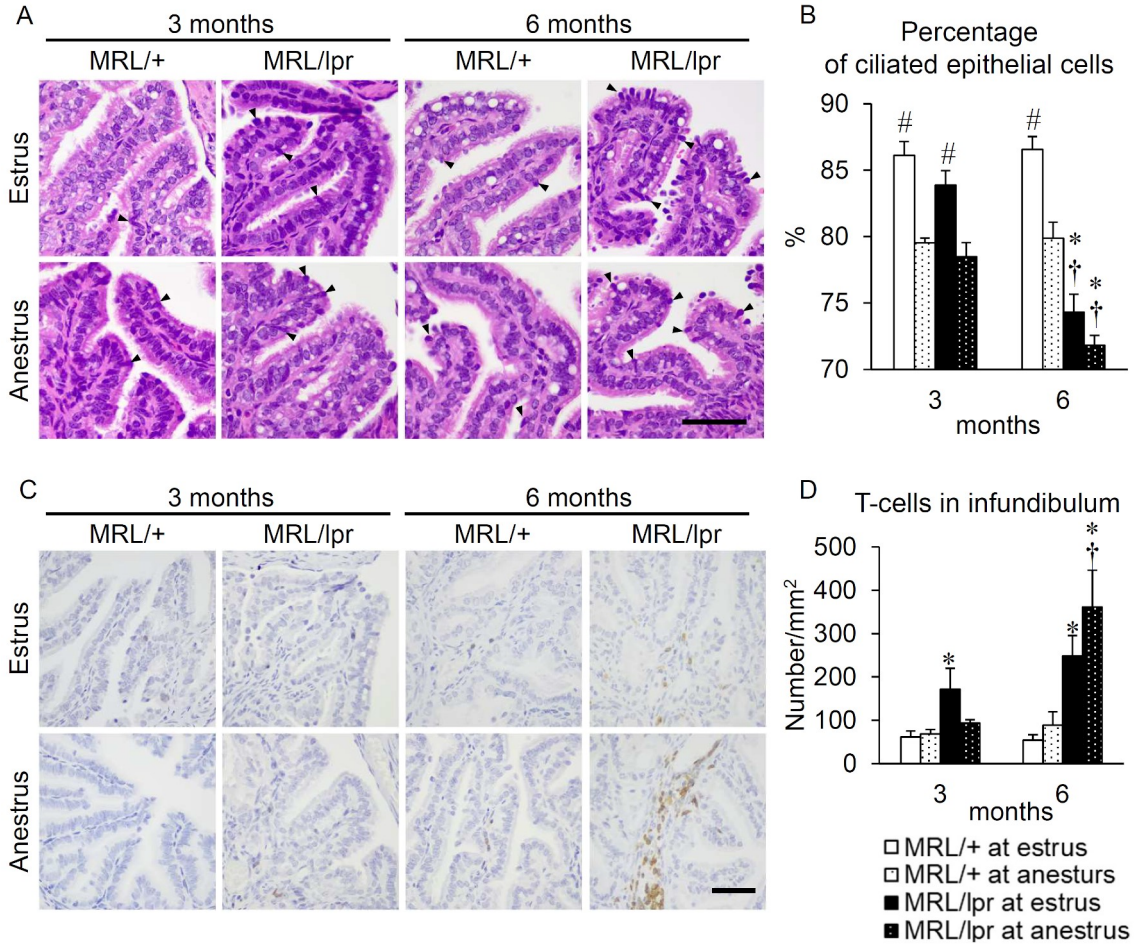

Figure 4-2. Estrous cycle-related morphological changes and inflammation in the oviductal infundibulum

(A) Histological sections of the oviductal infundibulum at estrus and anestrus stages stained with hematoxylin-eosin. Arrowheads indicate secretory cells. Bar = 50 μm.

(B) Percentage of ciliated epithelial cells composing the infundibulum epithelium. Each bar represents mean ± SE (n ≥4). #: comparison between stages at same age within same strain (Mann-Whitney *U*-test, $P < 0.05$). †: significant age-related difference at the same stage in the same strain (Mann-Whitney *U*-test, $P < 0.05$). *: significant differences between MRL/+ and MRL/lpr mice at the same age and stage (Mann-Whitney *U*-test, $P < 0.05$).

(C) Localization of CD-3 positive T-cells in the oviductal infundibulum at estrus and anestrus stages as revealed by immunohistochemistry. Bar = 50 μm.

(D) Number of CD3-positive T-cells in the infundibulum at anestrus and estrus stages. Each bar represents mean ± SE (n ≥4). †: significant difference between ages at the same stage in the same strain (by Mann-Whitney *U*-test, $P < 0.05$). *: significant differences between MRL/+ and MRL/lpr mice at the same age and stage (Mann-Whitney *U*-test, $P < 0.05$). No significant stage-related difference was detected by Mann-Whitney *U*-test.

MRL/+: MRL/MpJ, MRL/lpr: MRL/MpJ-Fas$^{lpr/lpr}$.

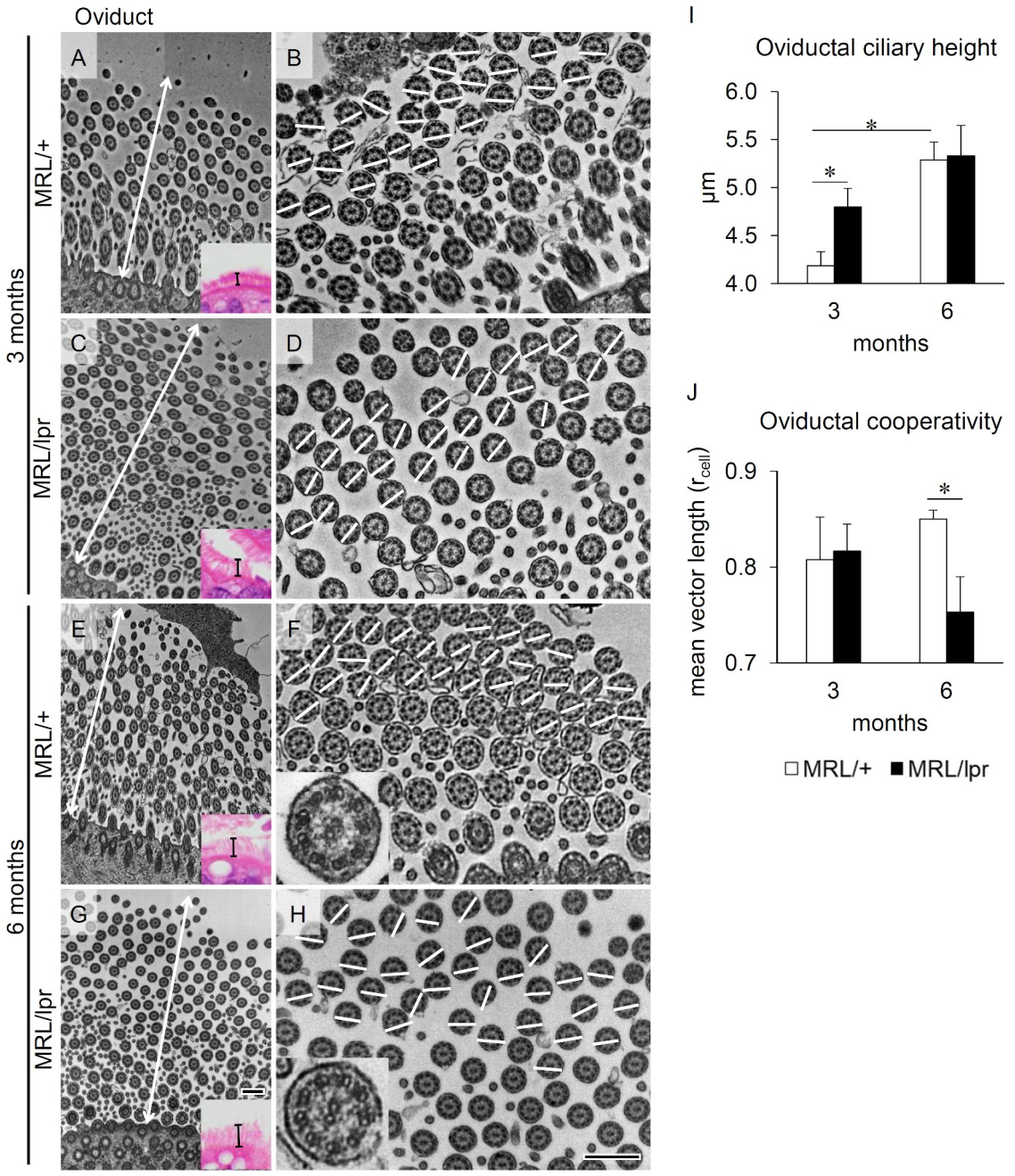

Figure 4-3. The ultrastructural changes in the cilia of the oviductal infundibulum.
(A-H) The oviductal ciliary ultrastructure as observed by transmission electron microscopy. The white bidirectional arrows indicate the ciliary height. The ciliary height on the oviductal ciliated epithelial cells in the HE-stained sections is shown as black lines in the insets of **(A)**, **(C)**, **(E)** and **(G)**. The white lines are drawn through central pairs of microtubules located at the center of cilia. Bar = 500 nm.
(I) The oviductal ciliary height. n = 4 per group. Data are the mean ± SE. **P* < 0.05 (Mann-Whitney *U*-test).
(J) Oviductal ciliary cooperativity of the beating direction is shown as mean vector length (r_{cell}). n = 4 per group. Data are the mean ± SE. **P* < 0.05 (Mann-Whitney *U*-test).
MRL/+: MRL/MpJ, MRL/lpr: MRL/MpJ-Fas$^{lpr/lpr}$.

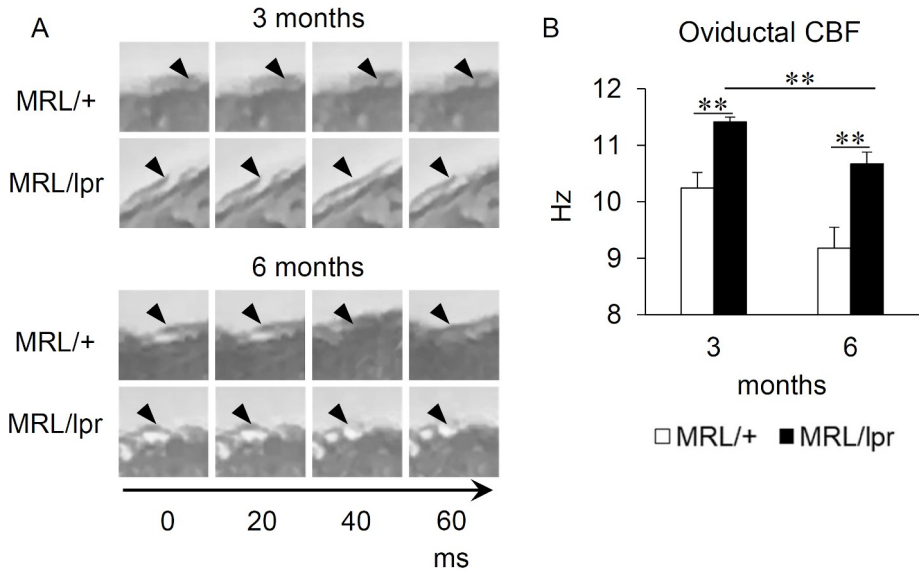

Figure 4-4. The ciliary beating in the ciliated epithelial cells in the oviductal infundibulum
(A) The sequential ciliary beating patterns observed by stereo microscopy. Arrowheads indicate the same cilia in multiple frames.
(B) Oviductal ciliary beating frequency (CBF). n = 7, 7, 8, 11. Data are mean ± SE. $^{**}P < 0.01$ (Mann-Whitney *U*-test). n values are listed in the following order: 3-month-old MRL/+ mice, 3-month-old MRL/lpr mice, 6-month-old MRL/+ mice, and 6-month-old MRL/lpr mice.
MRL/+: MRL/MpJ, MRL/lpr: MRL/MpJ-Fas$^{lpr/lpr}$.

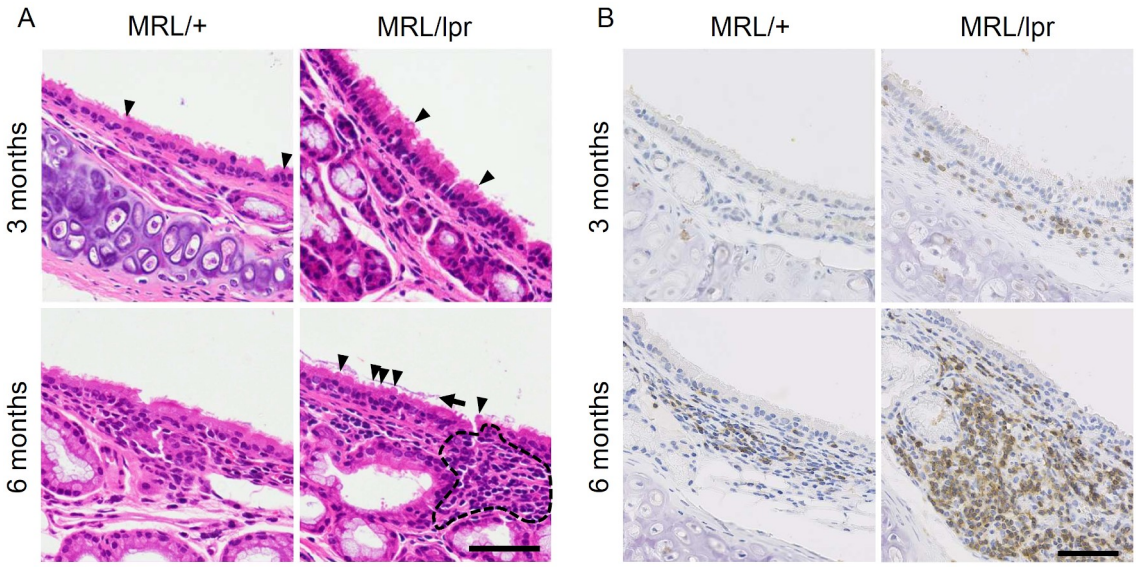

Figure 4-5. The histology and inflammation in the ciliated epithelial cells in the trachea.
(A) The histology of the trachea. Arrowheads indicate non-ciliated cells. Arrows indicate mucin layer. Dashed line indicates the region of infiltrated mononuclear cells. Hematoxylin-eosin stained. Bar = 50 μm.
(B) The localization of CD-3 positive T-cells in the trachea revealed by immunohistochemistry. Bar = 50 μm.

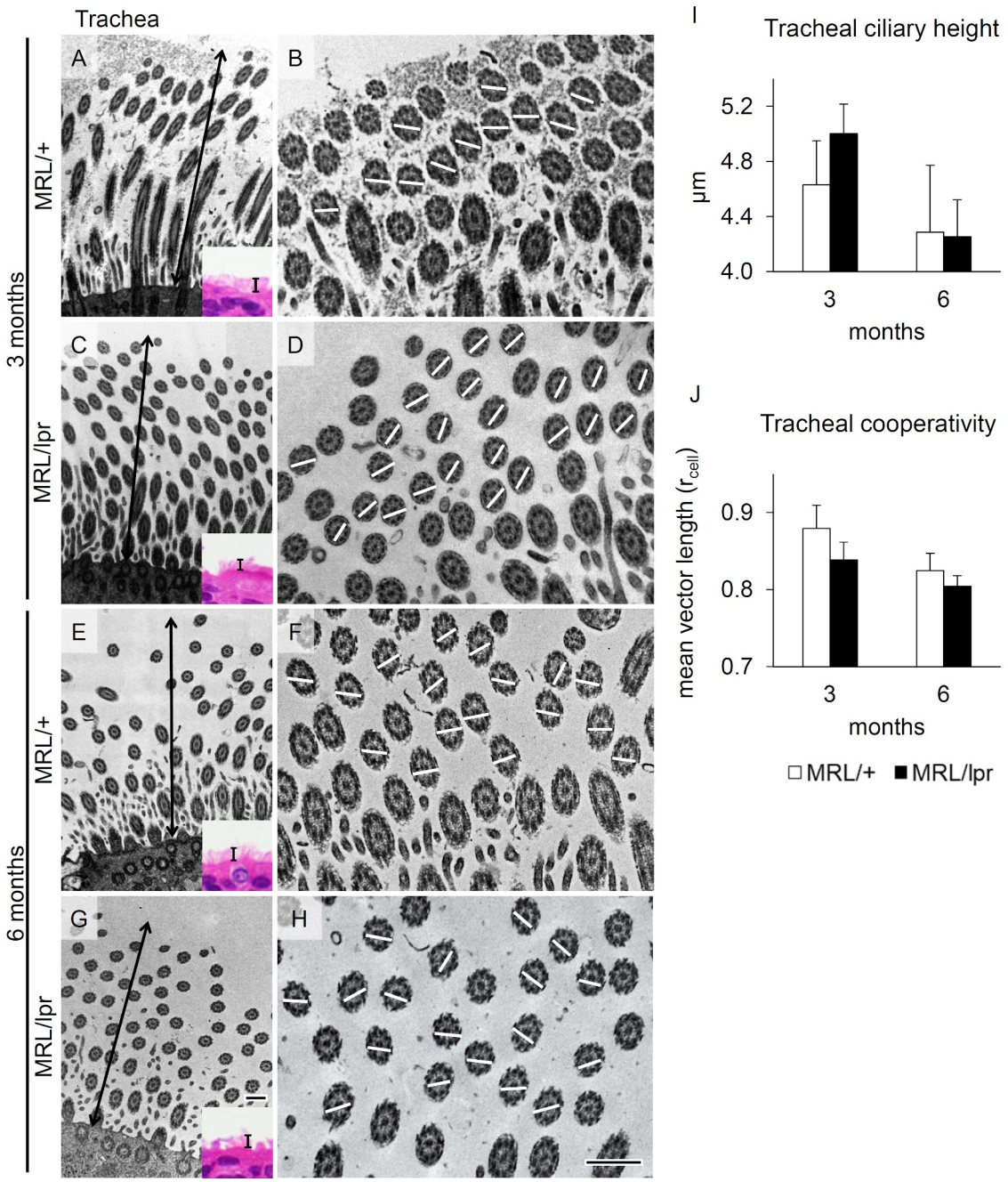

Figure 4-6. The ultrastructural changes in cilia of the ciliated epithelial cells in the trachea.
(A-H) The tracheal ciliary ultrastructure as observed by transmission electron microscopy. The black bidirectional arrows indicate the ciliary height. The ciliary height on the tracheal ciliated epithelial cells in the HE-stained sections is shown as black lines in the insets of **(A)**, **(C)**, **(E)** and **(G)**. The white lines are drawn through central pairs of microtubules located at the center of cilia. Bar = 500 nm.
(I) Tracheal ciliary height. n = 4 per group. Data are the mean ± SE. **P* < 0.05 (Mann-Whitney *U*-test).
(J) The tracheal ciliary cooperativity of the beating direction is shown as mean vector length (r_{cell}). n = 4 per group. Data are the mean ± SE.
MRL/+: MRL/MpJ, MRL/lpr: MRL/MpJ-Fas$^{lpr/lpr}$.

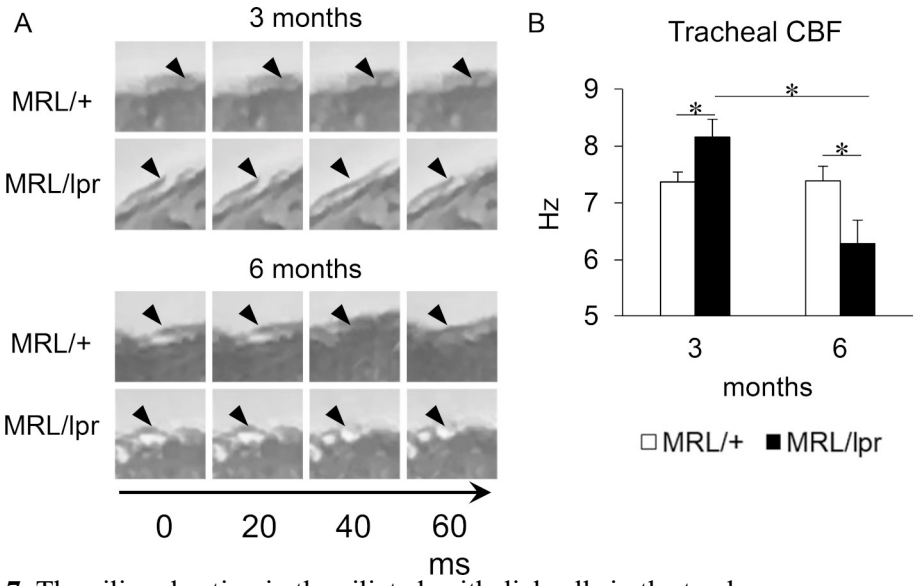

Figure 4-7. The ciliary beating in the ciliated epithelial cells in the trachea.
(A) The sequential ciliary beating patterns observed by stereo microscopy. Arrowheads indicate the same cilia in multiple frames.
(B) The trachea ciliary beating frequency (CBF). n = 4, 4, 6, 7. Data are the mean ± SE. **P* < 0.05 (Mann-Whitney U-test). n values are listed in the following order: 3-month-old MRL/+ mice, 3-month-old MRL/lpr mice, 6-month-old MRL/+ mice, and 6-month-old MRL/lpr mice.
MRL/+: MRL/MpJ, MRL/lpr: MRL/MpJ-Fas$^{lpr/lpr}$.

Movie 4-1. The ciliary beating in the oviductal infundibulum of MRL/MpJ mice at 3 months.
Movie 4-2. The ciliary beating in the oviductal infundibulum of MRL/MpJ mice at 6 months.
Movie 4-3. The ciliary beating in the oviductal infundibulum of MRL/MpJ-*Fas*$^{lpr/lpr}$ mice at 3 months.
Movie 4-4. The ciliary beating in the oviductal infundibulum of MRL/MpJ-*Fas*$^{lpr/lpr}$ mice at 6 months.
Movie 4-5. The ciliary beating in the trachea of MRL/MpJ mice at 3 months.
Movie 4-6. The ciliary beating in the trachea of MRL/MpJ mice at 6 months.
Movie 4-7. The ciliary beating in the trachea of MRL/MpJ-*Fas*$^{lpr/lpr}$ mice at 3 months.
Movie 4-8. The ciliary beating in the trachea of MRL/MpJ-*Fas*$^{lpr/lpr}$ mice at 6 months.

Conclusion

The female infertility and reproductive disorder are the serious problem underlying social background of declining birth rate in human and affecting stable supply of livestock product. Female infertility is caused by the interaction of various pathological factors of the reproductive tracts and disturbances in the physiological mechanism regulating healthy reproductive function, which makes it difficult to reveal all the details of the pathology of female infertility. Herein, this study focused on the pathology of oocyte pick-up by oviducts and aimed to reveal some of the mechanism of the pathogenesis of female infertility. Oocyte pick-up is one of the most important function of the oviductal infundibulum, where the oocytes produced from ovaries are transported into the lumen; the dysfunction of oocyte pick-up causes female infertility. However, not only physiological mechanism regulating oocyte pick-up but also the detailed pathogenesis mechanism of oocyte pick-up has not been fully understood.

Importantly, immune abnormality affects the healthy morphofunction of female reproductive tracts. In livestock animals, infections and inflammation in female reproductive tracts relate to declined fertility. It has been reported that women patients with autoimmune disease increase their risk of infertility and that the model mice of systemic autoimmune disease develop the failure of ovarian function. Therefore, the author hypothesized that autoimmune disease could affect oocyte pick-up and histologically examined the oviduct of the systemic autoimmune disease model, MRL/lpr mice.

In Chapter 1, the author firstly developed the histological method to evaluate the murine oocyte pick-up and confirmed whether autoimmune disease affects oocyte pick-up in MRL/lpr mice. The ovaries and oviducts of superovulated mice were removed, and the number of COCs in the oviductal lumen was counted under a stereomicroscope as the actual number of oocytes picked-up by infundibulum. The number of ruptured follicles and hemorrhagic bodies was counted in the histological serial sections of ovaries as the actual number of OOs by ovaries. The PUR, which is calculated by the numbers of COCs and OOs, was approximately 100% in healthy B6 mice, indicating that the PUR is the effective method to quantify the murine oocyte pick-up. On the other hand, the PUR of MRL/lpr mice at 6 months of age was significantly decreased compared to that of 3-month-old mice, and showed negative correlations with indices of autoimmune disease progression. In addition, the ultrastructural observations revealed that the infundibulum of MRL/lpr mice at 6 months of age swelled up and decreased the number of cilia

covering the epithelium. Taken together, the deterioration of autoimmune disease in MRL/lpr mice induces the oocyte pick-up dysfunction along with the morphological changes in the oviductal infundibulum.

In Chapter 2, the anatomical structure of the mesovarium and mesosalpinx enclosing the ovarian bursa that supports oocyte pick-up by the infundibulum was examined. The ovaries and oviducts of all examined mice were surrounded by the ovarian bursa with the small peritoneal opening, that is the FOB with the size of 0.04 to 0.12 cm^2. The FOB is surrounded by the LOB composed of a thick smooth muscle layer, suggesting that the contraction of the smooth muscle can change the size of the FOB and that ovulated oocytes can escape into the peritoneal cavity through the FOB in mice. The size of the FOB tended to be larger in 6-month-old MRL/lpr mice than that of other strains. Furthermore, the mesosalpinx surrounding the FOB, that is the LOB, showed deposition of collagen fibers. These results suggest that the morphological changes of the FOB and the functional changes of the LOB relate to the oocyte pick-up dysfunction in MRL/lpr mice.

In Chapter 3, the unique phenotypes relating to the ovarian function in supreovulated MRL strain mice suggested in Chapter 1 were analyzed in details. In Chapter 1, MRL/lpr mice and its wild type, MRL/+ mice, were found to produce significantly numerous numbers of oocyte after superovulation treatment. Herein, the gene sequences encoding sex hormones and their receptors in MRL/+ mice were compared with those in B6 mice by using next-generation exome sequencing. However, there were no mutations expected to affect the structure or/and function of these proteins. At 3 months, the fertilization rate of oocytes produced after superovulation treatment was significantly lower in MRL/+ mice than B6 mice. In addition, the theory raised in Chapter 1 why the PUR of MRL/+ mice exceeded 100% was confirmed. As the results of histological tracing of luteinization after superovulation treatment, it was revealed that luteinization progressed faster in MRL/+ mice than in B6 mice, which is suggested to be due to enhanced extracellular matrix remodeling in the postovulatory follicles in MRL/+ mice.

In Chapter 4, the morphofunctional changes of the infundibulum ciliated epithelium was examined in MRL/lpr mice. In the infundibulum of MRL/lpr mice at 6 months of age, the decreased number of ciliated epithelial cells, slower ciliary beating, and more randomized ciliary beating direction were observed compared to those of MRL/lpr mice at 3 months of age. Taken together with the report that the regular and coordinated ciliary beating is important for healthy

oocyte pick-up, these results indicate that the systemic autoimmune disease in MRL/lpr mice altered the healthy morphofunction of the infundibulum ciliated epithelium, which affects oocyte pick-up. In addition, there was significant infiltration of immune cells in the lamina propria of the infundibulum in MRL/lpr mice at 6 months of age, suggesting that the immune factors derived from these cells may be involved in the abnormal morphofunction of the ciliated epithelium.

In conclusion, this study showed that systemic autoimmune disease related to the onsets of oocyte pick-up dysfunction in mice along with the pathological alternations of the ciliated epithelium, the FOB, and the LOB. Further investigations on the morphofunction of oviducts among animal species and strains based on this study would emphasize its importance on the female reproductive process. These oviductal pathological theories on oocyte pick-up dysfunction due to immune abnormality contribute to further understanding and treatment of unexplained female infertility/reproductive disorders in the field of human and veterinary medicine.

Conclusion in Japanese

動物の繁殖障害及びヒトの雌性不妊症は、安定した畜産物の供給及び我が国の少子化克服を阻む重大な課題である。本課題を解決するため、排卵から着床までの生殖プロセスを妨げる雌性生殖器病態の解析が急務である。本研究では特に、卵管のピックアップ機能の病態に着目した。卵管の卵巣側末端・卵管ロートは、排卵卵子を卵管内へ誘導するピックアップ機能を担い、その機能異常・ピックアップ障害は繁殖障害及び不妊症の一因となる。しかし、ピックアップ機能の生理的制御機序のみならず、ピックアップ障害の詳細な発症機序は不明で、現在医学・獣医学領域の臨床現場における診断・治療法はない。

注目すべきことに、免疫異常は雌性不妊発症と深く関連する。家畜動物では、感染症や生殖器の炎症が繁殖率の低下を招く。さらに、女性の自己免疫疾患患者では不妊発症リスクが高いこと、及び自己免疫疾患モデルマウスでは卵巣内閉鎖卵胞の増加がみられることから、自己免疫異常は雌性生殖器の形態機能に重大な影響を及ぼすと考えられる。そこで本研究では、アポトーシス誘導受容体 Fas の *lpr* 変異に起因する全身性自己免疫疾患を発症するモデルマウス MRL/MpJ-*Fas*$^{lpr/lpr}$ (MRL/lpr)の卵管の形態機能解析を通し、自己免疫異常とピックアップ機能の関連性を考察した。

まず第 1 章では、マウスにおけるピックアップ機能の定量法を検討するとともに、自己免疫異常がピックアップ機能に影響を与えるか調査した。過剰排卵処置を施した雌マウスの卵巣・卵管を摘出し、卵管内の卵子卵丘細胞複合体の数を実体顕微鏡下で計測しピックアップ卵子数とした。卵巣の連続切片を作製し、破裂卵胞と出血体の数を計測し排卵卵子数とした。排卵卵子数に対するピックアップ卵子数の割合をピックアップ効率とした。健常な C57BL/6N (B6) においてピックアップ効率 (PUR) は約 100%であり、本法はピックアップ機能の定量法として有用だった。一方、重篤な自己免疫疾患を発症する 6 ヶ月齢の MRL/lpr において PUR は約 63%であり、疾患症状の軽い 3 ヶ月齢時の約 94%と比較して顕著に低下した。さらに、卵管ロートの超微形態観察の結果、6 ヶ月齢の MRL/lpr では、同齢 B6 や 3 ヶ月齢の MRL/lpr と比較し卵管ロートが腫脹し、上皮を覆う線毛が減少していた。以上より、MRL/lpr において、自己免疫疾患の進行が卵管ロートの形態的変化を伴ってピックアップ障害を招くことが示された。

続いて第 2 章では、卵巣嚢の形態を解剖学的に精査した。マウスの卵巣及び卵管ロートは、卵巣間膜及び卵管間膜によって包まれた袋状の構造“卵巣嚢”に位置するが、卵管峡部と子宮端を結ぶ卵管間膜上に 0.04～0.12cm^2 の卵巣嚢孔 (FOB) が存在したため、腹腔との連続性を保っていた。FOB は平滑筋に富む卵巣嚢孔間膜 (LOB) に囲まれ、その筋収縮によ

って FOB の大きさが変動する可能性が示された。つまり、マウスの排卵卵子は FOB を通して腹腔内に脱落すると考えられた。一方、6 ヶ月齢 MRL/lpr では、LOB が線維化し、3 ヶ月齢時と比較して FOB の面積が大きくなる傾向があったことから、FOB の形態変化が MRL/lpr のピックアップ障害に関与することが示唆された。

第 3 章では、第 1 章において示唆された MRL 系統の卵巣機能における特異的形質の詳細を解析した。第 1 章において、3 ヶ月齢の MRL/lpr およびその野生型である MRL/MpJ(MRL/+)は、B6 よりも過剰排卵処置後の排卵数が多かった。そこで、エクソーム解析によって、MRL/+における性ホルモン及びその受容体をコードする遺伝子配列を B6 と比較した結果、これら蛋白質の構造や機能に影響を及ぼすと予測される変異はみられなかった。一方で、過剰排卵処置で得られた卵子の受精率は B6 と比較して MRL/+で有意に低かった。また、第 1 章では MRL/+の PUR が 100%を超えていた。そこで、過剰排卵処置後の黄体形成過程を組織学的に追跡した結果、MRL/+では B6 に比べて黄体形成が早期に進行し、これには排卵後卵胞における細胞外マトリックスのリモデリングの亢進が関与することが示唆された。

最後に第 4 章では、卵管ロートの線毛上皮の形態機能を精査した。規則的な線毛運動は健常なピックアップ機能における必須要素であるが、6 ヶ月齢 MRL/lpr の卵管ロートでは、3 ヶ月齢時と比較して線毛上皮細胞数の減少、線毛運動速度の低下、及び線毛運動方向のばらつきの増大がみられた。このことから、全身性の自己免疫異常が卵管ロート線毛上皮の形態機能に影響を与えることが示された。また、6 ヶ月齢 MRL/lpr の卵管ロートの粘膜固有層には顕著な炎症細胞浸潤がみられ、これら細胞由来の液性免疫因子が線毛上皮の病態に関与すると考えられた。

結論として本研究は、マウスにおいて全身性自己免疫疾患が卵管の線毛上皮及び FOB・LOB を含む雌性生殖器の形態機能変化を通してピックアップ障害の発症に関与することを示した。今後、本知見を基に各種動物及びヒトの卵管病態を精査することで、原因不明の繁殖障害及び雌性不妊症の病態発生を説明できる可能性が示唆された。以上、本研究は免疫異常と卵管の機能障害の関連性を明らかにし、動物の繁殖障害及びヒトの雌性不妊症の病態発生機序の全貌を解明する上で必要不可欠な知見を提供した。

Acknowledgement

I would like to express my sincere gratitude to Professor Yasuhiro Kon of Laboratory of Anatomy, Department of Basic Veterinary Science, Faculty of Veterinary Medicine, Hokkaido University for the continuous supports and valuable advices in my research activities and career choice. I deeply appreciate Associate Professor Osamu Ichii of Laboratory of Anatomy, Department of Basic Veterinary Science, Faculty of Veterinary Medicine, Hokkaido University for the patient guidance and technical supports from my undergraduate days to now. I sincerely appreciate Professor Seiji Katagiri, Laboratory of Theriogenology, Department of Clinical Sciences, Faculty of Veterinary Medicine, Hokkaido University and Professor Mitsuyoshi Takiguchi, Laboratory of Veterinary Internal Medicine, Department of Veterinary Clinical Sciences, Faculty of Veterinary Medicine, Hokkaido University for their critical review and suggestions of this thesis. I would like to thank all members in Laboratory of Anatomy, Department of Basic Veterinary Science, Faculty of Veterinary Medicine, Hokkaido University and Laboratory of Veterinary Anatomy, School of Veterinary Medicine, Rakuno Gakuen University for their company and encouragement. I am grateful to my family for understanding and supporting my precious research life. Finally, I deeply express my sincere condolences and gratitude to all animals supporting this research.

References

1) Andrews BS, Eisenberg RA, Theofilopoulos AN, Izui S, Wilson CB, Meconahey PJ, Murphy ED, Roths JB, Dixon FJ. Spontaneous murine lupus-like syndromes. Clinical and immunopathological manifestations in several strains. J Exp Med 148, 1198-1215, 1978.

2) Andriantsirombaka RA, Aimée M, Rija R, Sinha S, Formigli L, Krishnamoorthy R, Nsa Mve Rose EE, Badulli G. Unexplained infertility. The perilous voyage of the human oocyte. Clin Obstet Gynecol Reprod Med 6, 1-3, 2020.

3) Ardighieri L, Lonardi S, Moratto D, Facchetti F, Shih IM, Vermi W, Kurman RJ. Characterization of the immune cell repertoire in the normal fallopian tube. Int J Gynecol Pathol 33, 581-591, 2014.

4) Armengot M, Milara J, Mata M, Gimeno JC, Carda C, Cortijo J. Cilia motility and structure in primary and secondary ciliary dyskinesia. Artic Am J Rhinol Allergy 24, 175-180, 2010.

5) Avasthi P, Marshall WF. Stages of ciliogenesis and regulation of ciliary length. Differentiation 83, S30-S42, 2012.

6) Balomenos D, Rumold R, Theofilopoulos AN. Interferon-ɤ is required for lupus-like disease and lymphoaccumulation in MRL-lpr mice. J Clin Invest 101, 364-371, 1998.

7) Beck-Peccoz P, Persani L. Premature ovarian failure. Orphanet J Rare Dis 1, 9, 2006.

8) Beck LR. Comparative observations on the morphology of the mammalian periovarial sac. J Morphol 136, 247-254, 1972.

9) Borpujari Scholar D, Ali Ahmed Professor F, Talukdar D, Borpujari D, Ali Ahmed F, Lalrintluanga K. Ultrasound as a diagnostic aid for anatomical defects of female reproductive tract: An overview. J Entomol Zool Stud 7, 533-536, 2019.

10) Budras KD, Habel RE, Wunshe A, Buda S. Bovine Anatomy: An Illustrated Text. First Edit. Schlütersche, Hannover. pp. 138, 2003.

11) Buhimschi CS, Zhao G, Sora N, Madri JA, Buhimschi IA, Allsworth J, Stevens E, Macones G, Buhimschi C, Weiner C. Myometrial wound healing post-Cesarean delivery in the MRL/MpJ mouse model of uterine scarring. Am J Pathol 177, 197-207, 2010.

12) Byers SL, Payson SJ, Taft RA. Performance of ten inbred mouse strains following

assisted reproductive technologies (ARTs). Theriogenology 65, 1716-1726, 2006.

13) Carp HJA, Selmi C. The autoimmune bases of infertility and pregnancy loss. J Autoimmun 38, J266-J274, 2012.

14) Carpintero NL, Suárez OA, Mangas CC, Varea CG, Rioja RG. Follicular steroid hormones as markers of oocyte quality and oocyte development potential. J Hum Reprod Sci 7, 187-193, 2014.

15) Chastant S, Saint-Dizier M. Inflammation: Friend or foe of bovine reproduction? Anim Reprod 16, 539-547, 2019.

16) Chen JJ, Lemieux BT, Wong BJF. A low-cost method of ciliary beat frequency measurement using iPhone and MATLAB. Otolaryngol Head Neck Surg 155, 252-256, 2016.

17) Clark-Knowles K V., Garson K, Jonkers J, Vanderhyden BC. Conditional inactivation of *Brca1* in the mouse ovarian surface epithelium results in an increase in preneoplastic changes. Exp Cell Res 313, 133-145, 2007.

18) Clark LD, Clark RK, Heber-Katz E. A new murine model for mammalian wound repair and regeneration. Clin Immunol Immunopathol 88, 35-45, 1998.

19) Committee of the American Society for Reproductive Medicine, Birmingham, Alabama TP. Gonadotropin preparations: Past, present, and future perspectives. Fertil Steril 90, S13-S20, 2008.

20) Corbeel L, Cornillie F, Lauweryns J, Boel M, van den Berghe G. Ultrastructural abnormalities of bronchial cilia in children with recurrent airway infections and bronchiectasis. Arch Dis Child 56, 929-933, 1981.

21) Cotchin E, Marchant J. Animal models for tumors of the ovary and uterus. In: Animal Tumors of the Female Reproductive Tract. Springer, New York. pp. 1-25, 1977.

22) Cotchin E, Marchant J. Spontaneous Tumors of the Uterus and Ovaries in Animals. Springer, New York. pp. 26-59, 1977.

23) Craig ME, Billow M. Anatomy, Abdomen and Pelvis, Broad Ligaments. In: StatPearls [Internet]. Treasure Island (FL): StatPearls Publishing. 2018.

24) Crow J, Amso NN, Lewin J, Shaw RW. Morphology and ultrastructure of fallopian tube epithelium at different stages of the menstrual cycle and menopause. Hum Reprod 9, 2224-2233, 1994.

25) Davis JS, Rueda BR. The corpus luteum: An ovarian structure with maternal instincts and suicidal tendencies. Front Biosci 7, 1949-1978, 2002.

26) Di Carlantonio G, Shaoulian R, Knoll M, Magers T, Talbot P. Analysis of ciliary beat frequencies in hamster oviducal explants. J Exp Zool 272, 142-152, 1995.

27) Dieker JWC, van der Vlag J, Berden JHM. Deranged removal of apoptotic cells: Its role in the genesis of lupus. Nephrol Dial Transplant 19, 282-285, 2004.

28) Dijkhuizen AA, Stelwagen J, Renkema JA. Economic aspects of reproductive failure in dairy cattle. I. Financial loss at farm level. Prev Vet Med 3, 251-263, 1985.

29) Dirksen ER, Satir P. Ciliary activity in the mouse oviduct as studied by transmission and scanning electron microscopy. Tissue Cell 4, 389-403, 1972.

30) Dixon D, Alison R, Bach U, Colman K, Foley GL, Harleman JH, Haworth R, Herbert R, Heuser A, Long G, Mirsky M, Regan K, van Esch E, Westwood FR, Vidal J, Yoshida M. Nonproliferative and proliferative lesions of the rat and mouse female reproductive system. J Toxicol Pathol 27, 1S-107S, 2014.

31) Dummer A, Rol N, Szulcek R, Kurakula K, Pan X, Visser BI, Jan Bogaard H, DeRuiter MC, Goumans MJ, Hierck BP. Endothelial dysfunction in pulmonary arterial hypertension: Loss of cilia length regulation upon cytokine stimulation. Pulm Circ 8, 1-9, 2018.

32) Ebner T, Shebl O, Moser M, Sommergruber M, Tews G. Developmental fate of ovoid oocytes. Hum Reprod 23, 62-66, 2008.

33) Elewa YHA, Ichii O, Kon Y. Sex-related differences in autoimmune-induced lung lesions in MRL/MpJ-*fas* ^{lpr} mice are mediated by the development of mediastinal fat-associated lymphoid clusters. Autoimmunity 50, 306-316, 2017.

34) Fang X, Zaman MH, Guo X, Ding H, Xie C, Zhang X, Deng GM. Role of hepatic deposited immunoglobulin G in the pathogenesis of liver samage in systemic lupus erythematosus. Front Immunol 9, 1457, 2018.

35) Garrido MR, Peña AI, Herradon PG, Becerra JJ, Sande J, Quintela LA. Evaluation of tubal patency in repeat breeder Holstein cows. Spanish J Agric Res 17, e04SC02, 2019.

36) Ginther OJ, Beg MA, Bergfelt DR, Donadeu FX, Kot K. Follicle selection in monovular species. Biol Reprod 65, 638-647, 2001.

37) Gordts S, Campo R, Rombauts L, Brosens I. Endoscopic visualization of the process of fimbrial ovum retrieval in the human. Hum Reprod 13, 1425-1428, 1998.

38) Gourevitch D, Clark L, Chen P, Seitz A, Samulewicz SJ, Heber-Katz E. Matrix metalloproteinase activity correlates with blastema formation in the regenerating MRL mouse ear hole model. Dev Dyn 226, 377-387, 2003.

39) Grosse-Onnebrink J, Werner C, Loges NT, Hormann K, Blum A, Schmidt R, Olbrich H, Omran H. Effect of TH2 cytokines and interferon gamma on beat frequency of human respiratory cilia. Pediatr Res 79, 731-735, 2016.

40) Guirao B, Meunier A, Mortaud S, Aguilar A, Corsi JM, Strehl L, Hirota Y, Desoeuvre A, Boutin C, Han YG, Mirzadeh Z, Cremer H, Montcouquiol M, Sawamoto K, Spassky N. Coupling between hydrodynamic forces and planar cell polarity orients mammalian motile cilia. Nat Cell Biol 12, 341-350, 2010.

41) Gustafsson H, Emanuelson U. Characterisation of the repeat breeding syndrome in Swedish dairy cattle. Acta Vet Scand 43, 115, 2002.

42) Halbert SA, Tam PY, Blandau RJ. Egg transport in the rabbit oviduct: The roles of cilia and muscle. Science 191, 1052-1053, 1976.

43) Haller-Kikkatalo K, Salumets A, Uibo R. Review on autoimmune reactions in female infertility: Antibodies to follicle stimulating hormone. Clin Dev Immunol 2012, 762541, 2012.

44) Hermes R, Hildebrandt TB, Göritz F. Reproductive problems directly attributable to long-term captivity-asymmetric reproductive aging. Anim Reprod Sci 82-83, 49-60, 2004.

45) Heydemann A. The super super-healing MRL mouse strain. Front Biol (Beijing) 7, 522-538, 2012.

46) Huang S, Driessen N, Knoll M, Talbot P. In vitro analysis of oocyte cumulus complex pickup rate in the hamster *Mesocricetus auratus*. Mol Reprod Dev 47, 312-322, 1997.

47) Hünerwadel A, Fagagnini S, Rogler G, Lutz C, Jaeger SU, Mamie C, Weder B, Ruiz PA, Hausmann M. Severity of local inflammation does not impact development of fibrosis in mouse models of intestinal fibrosis. Sci Rep 8, 15182, 2018.

48) Ichii O, Konno A, Sasaki N, Endoh D, Hashimoto Y, Kon Y. Autoimmune glomerulonephritis induced in congenic mouse strain carrying telomeric region of

chromosome 1 derived from MRL/MpJ. Histol Histopathol 23, 411-422, 2008.

49) Ichii O, Otsuka S, Sasaki N, Yabuki A, Ohta H, Takiguchi M, Hashimoto Y, Endoh D, Kon Y. Local overexpression of interleukin-1 family, member 6 relates to the development of tubulointerstitial lesions. Lab Invest 90, 459-475, 2010.

50) Iijima S, Yokoyama K. Socioeconomic factors and policies regarding declining birth rates in Japan. Nihon Eiseigaku Zasshi 73, 305-312, 2018.

51) Inoue Y. Hysteroscopic hydrotubation of the equine oviduct. Equine Vet J 45, 761-765, 2013.

52) Isaksson R, Tiitinen A. Present concept of unexplained infertility. Gynecol Endocrinol 18, 278-290, 2004.

53) Isaza-Restrepo A, Martin-Saavedra JS, Velez-Leal JL, Vargas-Barato F, Riveros-Dueñas R. The peritoneum: Beyond the tissue - A review. Front Physiol 9, 738, 2018.

54) Iwasaki A, Foxman EF, Molony RD. Early local immune defences in the respiratory tract. Nat Rev Immunol 17, 7-20, 2017.

55) Johnson LA, Luke A, Sauder K, Moons DS, Horowitz JC, Higgins PDR. Intestinal fibrosis is reduced by early elimination of inflammation in a mouse model of IBD: Impact of a “Top-Down” approach to intestinal fibrosis in mice. Inflamm Bowel Dis 18, 460-471, 2012.

56) Kanno H, Nose M, Itoh J, Taniguchi Y, Kyogoku M. Spontaneous development of pancreatitis in the MRL/Mp strain of mice in autoimmune mechanism. Clin Exp Immunol 89, 68-73, 1992.

57) Kauffold J, Groeger S, Bergmann K, Wehrend A. Use of contrast sonography to test for tubal patency in dairy cattle. J Reprod Dev 55, 335-338, 2009.

58) Kaufman MH, Whittingham DG. Viability of mouse oocytes ovulated within 14 hours of an injection of pregnant mares’ serum gonadotrophin. J Reprod Fertil 28, 465-468, 1972.

59) Kaufman MH, Nikitin AY, Sundberg JP. The ovary. In: Histologic Basis of Mouse Endocrine System Development: A Comparative Analysis. First Edit. CRC Press, Boca Raton. pp. 190, 2010.

60) Kellogg MP. The development of the periovarial sac in the white rat. Anat Rec 79, 465-477, 1941.

61) Khizroeva J, Nalli C, Bitsadze V, Lojacono A, Zatti S, Andreoli L, Tincani A, Shoenfeld Y, Makatsariya A. Infertility in women with systemic autoimmune diseases. Best Pract Res Clin Endocrinol Metab 33, 101369, 2019.

62) Klettke U, Luck W, Wahn U, Niggemann B. Platelet-activating factor inhibits ciliary beat frequency of human bronchial epithelial cells. Allergy Asthma Proc 20, 115-118, 1999.

63) Knoll M, Talbot P. Cigarette smoke inhibits oocyte cumulus complex pick-up by the oviduct in vitro independent of ciliary beat frequency. Reprod Toxicol 12, 57-68, 1998.

64) Kon Y, Endoh D. Morphological study of metaphase-specific apoptosis in MRL mouse testis. Anat Histol Embryol 29, 313-319, 2000.

65) Kon Y, Konno A, Hashimoto Y, Endoh D. Ovarian cysts in MRL/MpJ mice originate from rete ovarii. Anat Histol Embryol 36, 172-178, 2007.

66) König HE, Liebich H-G, Bragulla H. Veterinary Anatomy of Domestic Mammals : Textbook and Colour Atlas. 4th Editio. Schattauer Verlag, Stuttgart. pp. 423, 429-430, 2009.

67) Kubaisi B, Samra KA, Foster CS. Granulomatosis with polyangiitis (Wegener's disease): An updated review of ocular disease manifestations. Intractable Rare Dis Res 5, 61-69, 2016.

68) Kumar N, Singh A. Trends of male factor infertility, an important cause of infertility: A review of literature. J Hum Reprod Sci 8, 191-196, 2015.

69) Lee SH, Ichii O, Otsuka S, Yaser Hosney E, Namiki Y, Hashimoto Y, Kon Y. Ovarian cysts in MRL/MpJ mice are derived from the extraovarian rete: A developmental study. J Anat 219, 743-755, 2011.

70) Leferovich JM, Bedelbaeva K, Samulewicz S, Zhang XM, Zwas D, Lankford EB, Heber-Katz E. Heart regeneration in adult MRL mice. Proc Natl Acad Sci USA 98, 9830-9835, 2001.

71) Leigh MW, Pittman JE, Carson JL, Ferkol TW, Dell SD, Davis SD, Knowles MR, Zariwala MA. Clinical and genetic aspects of primary ciliary dyskinesia / Kartagener syndrome. Genet Med 11, 473-487, 2009.

72) Li M, Zhou TH, Gao Y, Zhang N, Li JC. Ultrastructure and estrogen regulation of the

lymphatic stomata of ovarian bursa in mice. Anat Rec 290, 1195-1202, 2007.

73) Li X, Gu W, Masinde G, Hamilton-Ulland M, Xu S, Mohan S, Baylink DJ. Genetic control of the rate of wound healing in mice. Heredity 86, 668-674, 2001.

74) Liao SB, Li HWR, Ho JC, Yeung WSB, Ng EHY, Cheung ANY, Tang F, O WS. Possible role of adrenomedullin in the pathogenesis of tubal ectopic pregnancy. J Clin Endocrinol Metab 97, 2105-2112, 2012.

75) Lurie M, Tur-Kaspa I, Weill S, Katz I, Rabinovici J, Goldenberg S. Ciliary ultrastructure of respiratory and fallopian tube epithelium in a sterile woman with Kartagener's syndrome: A quantitative estimation. Chest 95, 578-581, 1989.

76) Magdy N, El-Bahrawy M. Fallopian tube: Its role in infertility and gynecological oncology. World J Obstet Gynecol 3, 35-41, 2014.

77) Martin GG, Talbot P, Pendergrass P. An intrabursal injection procedure for the in vivo study of ovulation in hamsters. J Exp Zool 216, 461-468, 1981.

78) Mccomb P, Langley L, Sd M, Verdugo P. The oviductal cilia and Kartagener's syndrome. Fertil Steril 46, 412-416, 1986.

79) McGrath Jr. H, Biundo Jr. JJ. A longitudinal study of high and low avidity antibodies to double-stranded DNA in systemic lupus erythematosus. Arthritis Rheum 28, 425-430, 1985.

80) Mermillod P, Dalbis-Tran R, Uzbekova S, Thlie A, Traverso JM, Perreau C, Papillier P, Monget P. Factors affecting oocyte quality: Who is driving the follicle? Reprod Domest Anim 43, 393-400, 2008.

81) Millward S, Mueller K, Smith R, Higgins HM. A post-mortem survey of bovine female reproductive tracts in the UK. Front Vet Sci 6, 451, 2019.

82) Miranda S, Carolino N, Vilhena H, Payan-Carreira R, Pereira RMLN. Early embryo development, number, quality, and location and the relationship with plasma progesterone in dogs. Anim Reprod Sci 198, 238-245, 2018.

83) Mohammed MO, Amin FASM. Retrospective study of uterine tubes pathological abnormalities in slaughtered non-pregnant cows in sulaimani province. Assiut Vet Med J 61, 164-170, 2015.

84) Mutsaers SE. Mesothelial cells: Their structure, function and role in serosal repair. Respirology 7, 171-191, 2002.

85) Nakamura T, Sakata Y, Otsuka-Kanazawa S, Ichii O, Chihara M, Nagasaki K, Namiki Y, Kon Y. Genomic analysis of the appearance of ovarian mast cells in neonatal MRL/MpJ mice. PLoS One 9, e100617, 2014.

86) National Collaborating Centre for Women's and Children's Health (UK). Fertility: Assessment and treatment for people with fertility problems. Royal College of Obstetricians & Gynaecologists, 2013.

87) Ng A, Barker N. Ovary and fimbrial stem cells: Biology, niche and cancer origins. Nat Rev Mol Cell Biol 16, 625-638, 2015.

88) Niwa S, Nakajima K, Miki H, Minato Y, Wang D, Hirokawa N. KIF19A is a microtubule-depolymerizing kinesin for ciliary length control. Dev Cell 23, 1167-1175, 2012.

89) Norwood JT, Hein CE, Halbertt SA, Anderson RGW. Polycationic macromolecules inhibit cilia-mediated ovum transport in the rabbit oviduct. Cell Biol 75, 4413-4416, 1978.

90) O WS, Li HWR, Liao SB, Cheung ANY, Ng EHY, Yeung WSB, Ho JCM, Tang F. Decreases in adrenomedullin expression and ciliary beat frequency in the nasal epithelium in tubal pregnancy. Fertil Steril 100, 459-463.e1, 2013.

91) Ortega HH, Marelli BE, Rey F, Amweg AN, Díaz PU, Stangaferro ML, Salvetti NR. Molecular aspects of bovine cystic ovarian disease pathogenesis. Reproduction 149, R251-R264, 2015.

92) Otani Y, Ichii O, Otsuka-Kanazawa S, Chihara M, Nakamura T, Kon Y. MRL/MpJ-*Fas*^{lpr} mice show abnormalities in ovarian function and morphology with the progression of autoimmune disease. Autoimmunity 48, 402-411, 2015.

93) Otsuka S, Konno A, Hashimoto Y, Sasaki N, Endoh D, Kon Y. Oocytes in newborn MRL mouse testes. Biol Reprod 79, 9-16, 2008.

94) Papathanasiou A, Djahanbakhch O, Saridogan E, Lyons RA. The effect of interleukin-6 on ciliary beat frequency in the human fallopian tube. Fertil Steril 90, 391-394, 2008.

95) Peters H, McNatty KP. The Ovary : A Correlation of Structure and Function in Mammals. University of California Press, Berkeley. pp. 75, 1980.

96) Peters WM. Nature of "basal" and "reserve" cells in oviductal and cervical epithelium

in man. J Clin Pathol 39, 306-312, 1986.

97) Practice Committee of the American Society for Reproductive Medicine. Diagnostic evaluation of the infertile female: A committee opinion. Fertil Steril 103, e44-e50, 2015.

98) Quaas A, Dokras A. Diagnosis and treatment of unexplained infertility. Rev Obstet Gynecol 1, 69-76, 2008.

99) Rashidi Z, Azadbakht M, Amini A, Karimi I. Hydrostatic pressure affects in vitro maturation of oocytes and follicles and increases granulosa cell death. Cell J 15, 282-293, 2014.

100) Rautiainen M, Collan Y, Nuutinen J. A method for measuring the orientation ("beat direction") of respiratory cilia. Arch Otorhinolaryngol 243, 265-268, 1986.

101) Revelli A, Delle Piane L, Casano S, Molinari E, Massobrio M, Rinaudo P. Follicular fluid content and oocyte quality: From single biochemical markers to metabolomics. Reprod Biol Endocrinol 7, 40, 2009.

102) Richards JS, Russell DL, Ochsner S, Hsieh M, Doyle KH, Falender AE, Lo YK, Sharma SC. Novel signaling pathways that control ovarian follicular development, ovulation, and luteinization. Recent Prog Horm Res 57, 195-220, 2002.

103) Roperto F, Brunetti A, Saviano L, Galati P. Morphologic alterations in the cilia of a cat. Vet Pathol 33, 460-462, 1996.

104) Sakamaki K, Yoshida H, Nishimura Y, Nishikawa SI, Manabe N, Yonehara S. Involvement of Fas antigen in ovarian follicular atresia and luteolysis. Mol Reprod Dev 47, 11-18, 1997.

105) Santiago-Raber ML, Laporte C, Reininger L, Izui S. Genetic basis of murine lupus. Autoimmun Rev 3, 33-39, 2004.

106) Sawamukai Y, Minami Y, Nakano T, De Silva LNA. Tubal patency and fertility in repeat breeder cows. J Jpn Vet Med Assoc 50, 224-227, 2014.

107) Sen A, Kushnir VA, Barad DH, Gleicher N. Endocrine autoimmune diseases and female infertility. Nat Rev Endocrinol 10, 37-50, 2014.

108) Shi D, Komatsu K, Uemura T, Fujimori T. Analysis of ciliary beat frequency and ovum transport ability in the mouse oviduct. Genes Cells 16, 282-290, 2011.

109) Shinohara H, Nakatani T, Matsuda T. Postnatal development of the ovarian bursa of

the golden hamster (*Mesocricetus auratus*): Its complete closure and morphogenesis of lymphatic stomata. Am J Anat 179, 385-402, 1987.

110) Shiozuru D, Ichii O, Kimura J, Nakamura T, Elewa YHA, Otsuka-Kanazawa S, Kon Y. MRL/MpJ mice show unique pathological features after experimental kidney injury. Histol Histopathol 31, 189-204, 2016.

111) Shorter SL, Albaghdadi AJH, Kan FWK. Alterations in oviductal cilia morphology and reduced expression of axonemal dynein in diabetic NOD mice. Tissue Cell 48, 588-595, 2016.

112) Singh P, Mondal S, Singh RL. Advances in Animal Genomics. First Edit. Academic Press, London. pp. 1-12, 2020.

113) Sirotkin A V. Effect of two types of stress (heat shock/high temperature and malnutrition/serum deprivation) on porcine ovarian cell functions and their response to hormones. J Exp Biol 213, 2125-2130, 2010.

114) Smith MF, McIntush EW, Ricke WA, Kojima FN, Smith GW. Regulation of ovarian extracellular matrix remodelling by metalloproteinases and their tissue inhibitors: Effects on follicular development, ovulation and luteal function. J Reprod Fertil Suppl 54, 367-381, 1999.

115) Smith S, Pfeifer SM, Collins JA. Diagnosis and management of female infertility. JAMA 290, 1767-1770, 2003.

116) Spearow JL. Major genes control hormone-induced ovulation rate in mice. J Reprod Fertil 82, 787-797, 1988.

117) Stocco C, Telleria C, Gibori G. The nolecular control of corpus luteum formation, function, and regression. Endocr Rev 28, 117-149, 2007.

118) Takeo T, Nakagata N. Combination medium of cryoprotective agents containing L-glutamine and methyl-β-cyclodextrin in a preincubation medium yields a high fertilization rate for cryopreserved C57BL/6J mouse sperm. Lab Anim 44, 132-137, 2010.

119) Takeo T, Hoshii T, Kondo Y, Toyodome H, Arima H, Yamamura K, Irie T, Nakagata N. Methyl-beta-cyclodextrin improves fertilizing ability of C57BL/6 mouse sperm after freezing and thawing by facilitating cholesterol efflux from the cells. Biol Reprod 78, 546-551, 2008.

120) Talbot P, Geiske C, Knoll M. Oocyte pickup by the mammalian oviduct. Mol Biol Cell 10, 5-8, 1999.

121) Talbot P, Riveles K. Smoking and reproduction: The oviduct as a target of cigarette smoke. Reprod Biol Endocrinol 3, 52, 2005.

122) Tang B, Matsuda T, Akira S, Nagata N, Ikehara S, Hirano T, Kishimoto T. Age-associated increase in interleukin 6 in MRL/lpr mice. Int Immunol 3, 273-278, 1991.

123) Thomas B, Rutman A, Hirst RA, Haldar P, Wardlaw AJ, Bankart J, Brightling CE. Ciliary dysfunction and ultrastructural abnormalities are features of severe asthma. J Allergy Clin Immunol 126, 722-729.e2, 2010.

124) Trabert B, Tworoger SS, O'Brien KM et al. The risk of ovarian cancer increases with an increase in the lifetime number of ovulatory cycles: An analysis from the Ovarian Cancer Cohort Consortium (OC3). Cancer Res 80, 1210-1218, 2020.

125) Tsevat DG, Wiesenfeld HC, Parks C, Peipert JF. Sexually transmitted diseases and infertility. Am J Obstet Gynecol 216, 1-9, 2017.

126) Tzelos T, Howes NL, Esteves CL, Howes MP, Byrne TJ, Macrae AI, Donadeu FX. Farmer and veterinary practices and opinions related to fertility testing and pregnancy diagnosis of UK dairy cows. Front Vet Sci 7, 564209, 2020.

127) Ullrich S, Gustke H, Lamprecht P, Gross WL, Schumacher U, Ambrosch P. Severe impaired respiratory ciliary function in Wegener granulomatosis. Ann Rheum Dis 69, 1067-1071, 2009.

128) van den Boogaard E, Vissenberg R, Land JA, van Wely M, van der Post JAM, Goddijn M, Bisschop PH. Significance of (sub)clinical thyroid dysfunction and thyroid autoimmunity before conception and in early pregnancy: A systematic review. Hum Reprod Update 17, 605-619, 2011.

129) Vanaken GJ, Bassinet L, Boon M, Mani R, Honoré I, Papon JF, Cuppens H, Jaspers M, Lorent N, Coste A, Escudier E, Amselem S, Maitre B, Legendre M, Christin-Maitre S. Infertility in an adult cohort with primary ciliary dyskinesia: Phenotype-gene association. Eur Respir J 50, 1700314, 2017.

130) Vander Borght M, Wyns C. Fertility and infertility: Definition and epidemiology. Clin Biochem 62, 2-10, 2018.

131) van der Hoek KH, Maddocks S, Woodhouse CM, van Rooijen N, Robertson SA,

Norman RJ. Intrabursal injection of clodronate liposomes causes macrophage depletion and inhibits ovulation in the mouse ovary. Biol Reprod 62, 1059-1066, 2000.

132) Vanderhyden BC, Rouleau A, Armstrong DT. Effect of removal of the ovarian bursa of the rat on infundibular retrieval and subsequent development of ovulated oocytes. Reproduction 77, 393-399, 1986.

133) Walker MH, Tobler KJ. Female Infertility. In: StatPearls [Internet]. Treasure Island (FL): StatPearls Publishing. 2021.

134) Wang L, Liu N, Xiong C, Xu L, Shi Y, Qiu A, Zang X, Mao H, Zhuang S. Inhibition of EGF receptor blocks the development and progression of peritoneal fibrosis. J Am Soc Nephrol 27, 2631-2644, 2016.

135) Wang ZB, Li M, Li JC. Recent advances in the research of lymphatic stomata. Anat Rec 293, 754-761, 2010.

136) Wells RG. Tissue mechanics and fibrosis. Biochim Biophys Acta 1832, 884-890, 2013.

137) Wimsatt WA, Waldo CM. The normal occurrence of a peritoneal opening in the bursa ovarii of the mouse. Anat Rec 93, 47-57, 1945.

138) Wodaje HB, Mekuria TA. Risk factors of repeat breeding in dairy cattle. Adv Biol Res 10, 213-221, 2016.

139) Woessner JF. Matrix metalloproteinases and their inhibitors in connective tissue remodeling. FASEB J 5, 2145-2154, 1991.

140) Wynn TA. Cellular and molecular mechanisms of fibrosis. J Pathol 214, 199-210, 2008.

141) Xiao S, Duncan FE, Bai L, Nguyen CT, Shea LD, Woodruff TK. Size-specific follicle selection improves mouse oocyte reproductive outcomes. Reproduction 150, 183-192, 2015.

142) Yamamoto A, Omotehara T, Miura Y, Takada T, Yoneda N, Hirano T, Mantani Y, Kitagawa H, Yokoyama T, Hoshi N. The mechanisms underlying the effects of amh on müllerian duct regression in male mice. J Vet Med Sci 80, 557-567, 2018.

143) Yamashita Y, Nakamura T, Otsuka-Kanazawa S, Ichii O, Kon Y. Morphological characteristics observed during early follicular development in perinatal MRL/MpJ

mice. Jpn J Vet Res 63, 25-36, 2015.

144) Yang JQ, Saxena V, Xu H, Van Kaer L, Wang CR, Singh RR. Repeated α-galactosylceramide administration results in expansion of NK T cells and alleviates inflammatory dermatitis in MRL-*lpr/lpr* mice. J Immunol 171, 4439-4446, 2003.

145) Yang J, Li Q, Yang X, Li M. Interleukin-9 is associated with elevated anti-double-stranded DNA antibodies in lupus-prone mice. Mol Med 21, 364-370, 2015.

146) Yániz JL, Recreo P, Carretero T, Arceiz E, Hunter RHF, López-Gatius F. The peritoneal mesothelium covering the genital tract and its ligaments in the female pig shows signs of active function. Anat Rec 290, 831-837, 2007.

147) Yokoyama M, Hioki K. The copulation rate and the embryo recovery rate following induced superovulation in various strains of mice. J Mamm Ova Res 7, 89-94, 1990.

148) Yoo HS. Infectious causes of reproductive disorders in cattle. J Reprod Dev 56, S53-S60, 2010.

149) Yuan S, Wang Z, Peng H, Ward SM, Hennig GW, Zheng H, Yan W. Oviductal motile cilia are essential for oocyte pickup but dispensable for sperm and embryo transport. Proc Natl Acad Sci 118, e2102940118, 2021.

150) Yung S, Li FK, Chan TM. Peritoneal mesothelial cell culture and biology. Perit Dial Int 26, 162-173, 2006.

151) Yusuf M, Nakao T, Ranasinghe RBK, Gautam G, Long ST, Yoshida C, Koike K, Hayashi A. Reproductive performance of repeat breeders in dairy herds. Theriogenology 73, 1220-1229, 2010.

152) Zenclussen AC, Hämmerling GJ. Cellular regulation of the uterine microenvironment that enables embryo implantation. Front Immunol 6, 321, 2015.

153) Zhang H, Zhang Y, Zhao H, Zhang Y, Chen Q, Peng H, Lei L, Qiao J, Shi J, Cao Z, Duan E, Jin Y. Hormonal regulation of ovarian bursa fluid in mice and involvement of aquaporins. PLoS One 8, e63823, 2013.

154) Zoda A, Urakawa M, Oono Y, Ogawa S, Satoh M. Estimation of genetic parameters for superovulatory response traits in Japanese Black cows. J Anim Sci 99, 1-7, 2021.